Observational Studies of Accretion Disks in Black Hole X-ray Binaries

Megumi Shidatsu
Department of Astronomy
Kyoto University

A thesis submitted for the degree of
Doctor of Philosophy

January, 2015

Abstract

Black hole X-ray binaries (BHXBs) in our galaxy provide important clues to understand the fundamental physics of black hole accretion and outflows. In order to study the inner disk structure and disk winds in the canonical two states, the "low/hard" state and the "high/soft" state, we analyze X-ray data of two Galactic BHXBs, H 1743−322 and MAXI J1305−704, obtained with *Suzaku* and *Swift*.

The *Suzaku* observations of H 1743−322 were carried out in the low/hard state during its outburst in 2012 October. Located in close proximity to the Galactic center, the source is heavily absorbed and subject to scattering by interstellar dust. To accurately analyze the X-ray spectra, we appropriately take into account these effects. The time-averaged spectra in the 1–200 keV band are dominated by a hard power-law component of a photon index of ≈1.6 with a high-energy cutoff at ≈60 keV, which is well described with Comptonization of the disk emission by hot corona. We estimate the inner disk radius from the multi-color disk component, and find that it is 1.3–2.3 times larger than the radius in the high/soft state. This suggests that the standard disk does not extend to the innermost stable circular orbit (ISCO). The stable disk component is also estimated in a way independent of the time-averaged spectral modeling, by analyzing short-term spectral variability on the ∼1-sec timescale. A weak low-frequency quasi-periodic oscillation (QPO) at 0.1–0.2 Hz is detected, whose frequency is found to correlate with the X-ray luminosity and photon index. This result can be explained by the evolution of the disk truncation radius, which would set the QPO frequency.

The black hole candidate MAXI J1305−704, discovered with *MAXI* in 2012, was observed with *Suzaku* and *Swift* in the low/hard and high/soft states, respectively. The 40-ksec *Suzaku* observation shows two types of clear absorption dips. Both of them recur on a dip interval of 9.74 ± 0.04 hours, which we identify with the orbital period. There is also partially ionized absorption in the non-dip (persistent) emission in both the high/soft state and, very unusually, the low/hard state. However, this absorption (in both states) has a substantially lower ionization level than that seen in other high inclination systems, where the material forms an extended homogeneous disk wind. We suggest that the absorption is clumpy, compact structures associated with the dipping material, which we see uniquely in this source because we view it at a very large inclination angle. A large inclination angle is also favored, together with a low black hole mass, to explain the high disk temperature seen in the fairly low luminosity high/soft state, because Doppler boosting enhances the disk temperature at high inclination. The inner disk radius inferred from these data is significantly smaller than that of the soft component seen in the low/hard state, supporting models where the standard disk does not extend to the ISCO at low luminosities.

The results from the detailed spectral analysis of both sources indicate that the standard disk is receded from the ISCO in the low/hard state, in which the disk emission is strongly Compton-scattered by electrons in the hot flow or corona. We find that there is another type of ionized absorber as observed in MAXI J1305−704, with different properties from the normal, extended homogeneous disk winds. The origin and structure of such absorbers may be fully uncovered in the near future through high-sensitivity high-resolution spectroscopy with *ASTRO-H*.

Contents

List of Figures

List of Tables

1

Introduction

1.1 Stellar-mass Black Holes

Black holes are the most extreme and bizarre objects derived from General Theory of Relativity. Their gravitational fields are so strong that nothing can escape. Since they are discovered as an analytic solution of Einstein's equation of gravity (Schwarzschild, 1916) and named by J. A. Wheeler, black holes have been one of the most popular terms of astrophysics. They have attracted many people and inspired our imagination with their mysterious nature. A black hole is formed when an object becomes unable to support its own gravity. The theory of stellar evolution predicts that (stellar-mass) black holes can be born in the end of the most massive stars (Oppenheimer & Snyder, 1939). When such a star (with a mass of $\gtrsim 20\,M_\odot$) runs out of its own nuclear fuel, it rapidly collapses on itself with a gigantic explosion called supernova, remaining the core as a black hole.

The history of the observational studies of stellar-mass black holes started in the early days of X-ray astronomy. Oda et al. (1971) first pointed out the possibility that the bright X-ray source Cygnus X-1 contains a black hole and that the strong short-term variability seen in its X-ray light curve is generated in the vicinity of the compact object. The optical counterpart of Cyg X-1 was soon identified with an O-type blue supergiant star, known as HDE 226868. The star was found to orbit around the X-ray emitter in a 5.6 day period (Bolton, 1972; Webster & Murdin, 1972). Further optical observations allowed to estimate the physical parameters of the binary system and to constrain the mass of the compact object in Cyg X-1. The mass function $f(M)$, which directly relates observables to the masses of a compact object and its companion star, is derived by using the Kepler's third law as

$$f(M) = \frac{(M \sin i)^3}{(M+m)^2} = \frac{K^3 P}{2\pi G}, \tag{1.1}$$

where M, m, i, K, P, G represent the masses of the compact object and that of the counterpart, the inclination angle, the amplitude of the radial velocity of the counterpart, the orbital period, and the gravitational constant, respectively. Spectroscopy of optical absorption lines from HDE 226868 yielded $K = 75$ km sec^{-1}. The companion star's mass and the inclination angle are estimated as $m \approx 20 M_{\odot}$ and $i \approx 30^{\circ}$, respectively. From these parameters, the mass of the compact object in Cyg X-1 is calculated as $\approx$10 $M_{\odot}$ (Ninkov et al., 1987)[1], exceeding the maximum mass of a neutron star, which is not precisely estimated yet but likely less than $\approx$3 $M_{\odot}$. Cyg X-1 was thus inferred to harbor a black hole. This is the first evidence that stellar-mass black holes are not pure theoretical products, but actually present in the Universe.

1.2 Black Hole X-ray Binaries

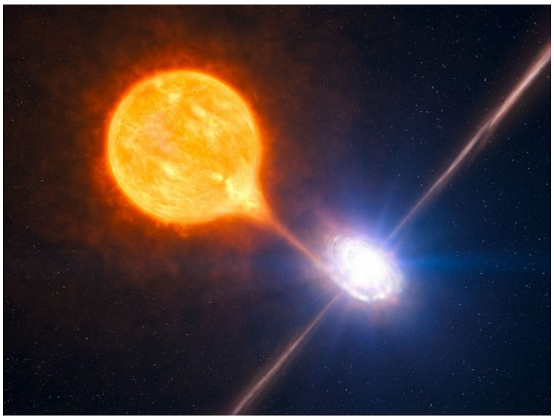

Figure 1.1: Image of a BHXB (Credit: ESO/L.Calçada).

A black hole X-ray binary (BHXB) is a close binary system consisting of a normal star and a stellar-mass black hole (Figure 1.1). The gas falling onto the black hole from the companion star forms an accretion disk and emits strong X-rays by releasing an enormous amount of the gravitational energy. BHXBs not only swallow up matter but

---

[1] The black hole mass of Cyg X-1 has recently been refined to $14.8 \pm 1 M_{\odot}$ by Orosz et al. (2011).

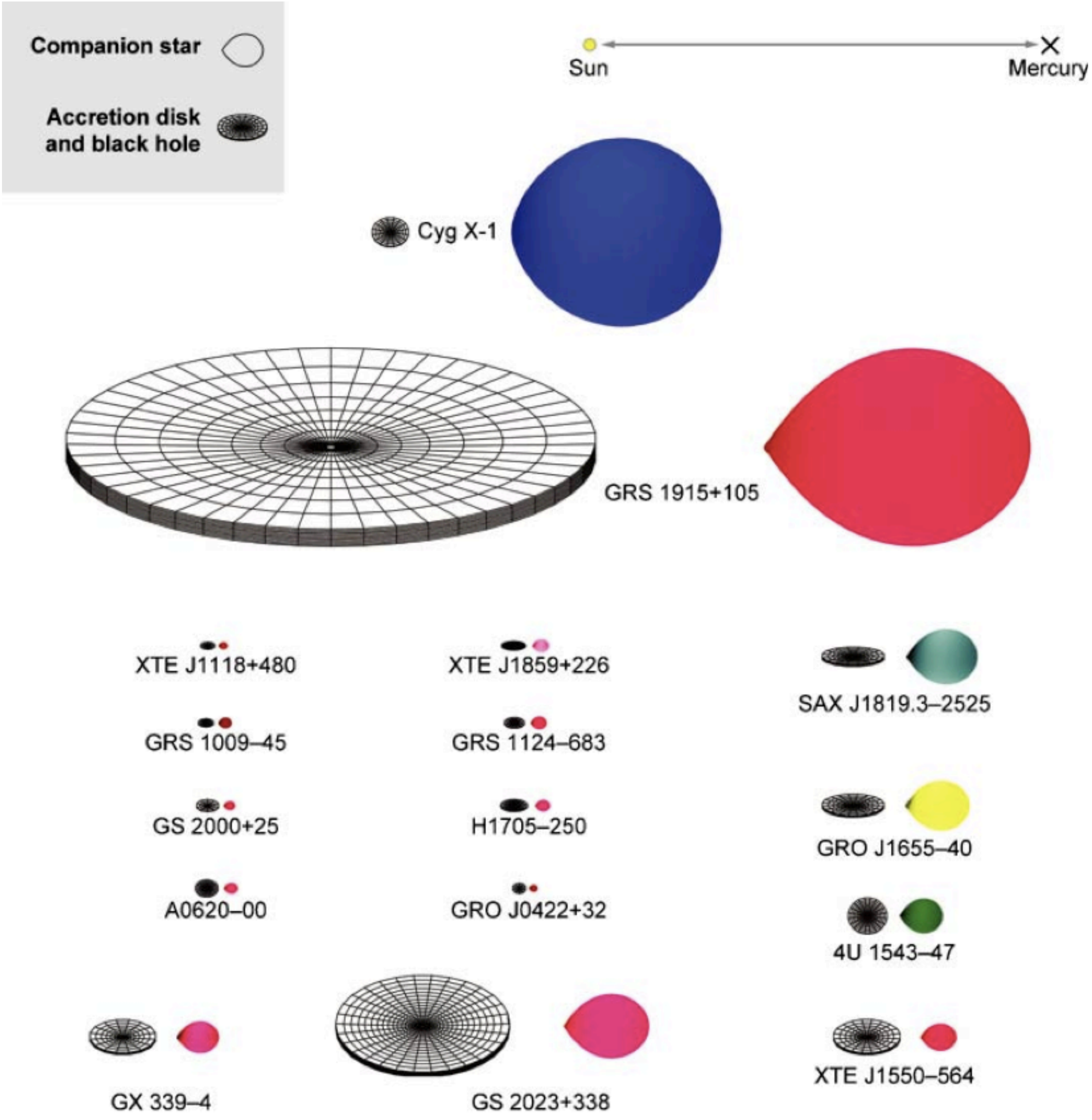

Figure 1.2: Schematic sketch of 16 BHXBs in our galaxy (Remillard & McClintock, 2006). The size of the individual systems in the figure reflects the real scale. The Sun-Mercury distance (0.4 AU) is shown at the top. The estimated binary inclination is indicated by the tilt of the accretion disk. The color of the companion star roughly indicates to its surface temperature.

also sometimes launch powerful outflows: relativistic jets and disk winds perpendicular to and along with the disk plane, respectively (see Section 1.4 for details).

After Cyg X-1, more than 20 BHXBs are discovered so far. Figure 1.2 displays a schematic sketch of 16 known BHXBs in our galaxy. Only a few systems have supergiant companions, while many of them contain small stars. X-ray binaries that have massive early type (i.e., O- or B-type) secondaries are called high mass X-ray binaries. They are persistently bright in X-rays like Cyg X-1. Some of them may feed their black holes through powerful stellar winds from the companion stars, as illustrated in the right panel in Figure 1.3. On the other hand, those containing less massive, late type stars are called low mass X-ray binaries, in which a black hole accretes gas via Roche-lobe overflow (left panel in Fig. 1.3). They are highly transient sources, increasing and decreasing their X-ray luminosities in several orders of magnitude, together with ejection and suppression of jets and disk winds (see below). A large fraction of known BHXBs are categorized as low mass X-ray binaries.

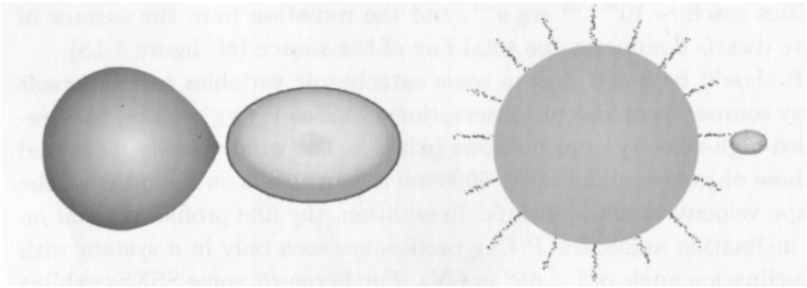

Figure 1.3: Schematic pictures of a low mass X-ray binary (left) and a high mass X-ray binary (right), taken from Kato et al. (2008).

1.3 X-ray Properties of Black Hole X-ray Binaries

1.3.1 State Transitions and Spectral Behavior in Outbursts

Transient BHXBs are normally very faint or even undetectable, but suddenly undergo dramatic outbursts, changing their X-ray luminosities (which are mainly determined by the mass accretion rates) in several orders of magnitude (e.g., Tanaka & Shibazaki, 1996) on a human timescale, typically in ≈10 days to several months for the whole

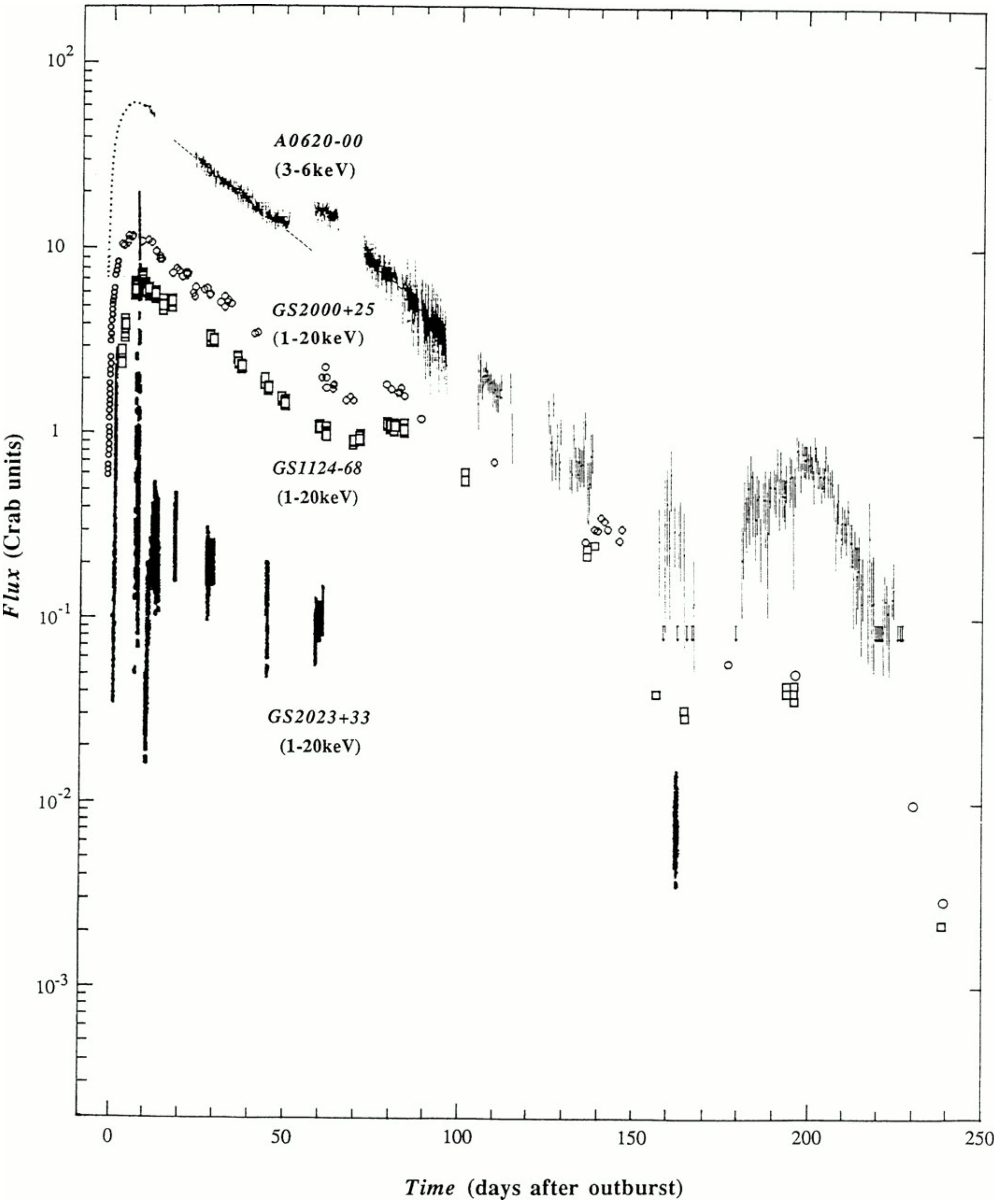

Figure 1.4: X-ray light curves of four transient BHXBs (Tanaka & Shibazaki, 1996).

period of an outburst (see Figure 1.4). At the same time, they exhibit several distinct "states" with different X-ray spectral shapes at different luminosities, as noticed in the left panel of Figure 1.5). The most canonical ones among them are so-called the "low/hard state", which is seen at relatively low luminosities during the beginning and end of outbursts, and the "high/soft state", appearing at higher soft X-ray (<10 keV) luminosities. At around the peak luminosities in outbursts, the "very high state" is sometimes observed, where the soft and hard X-ray fluxes are both strong.

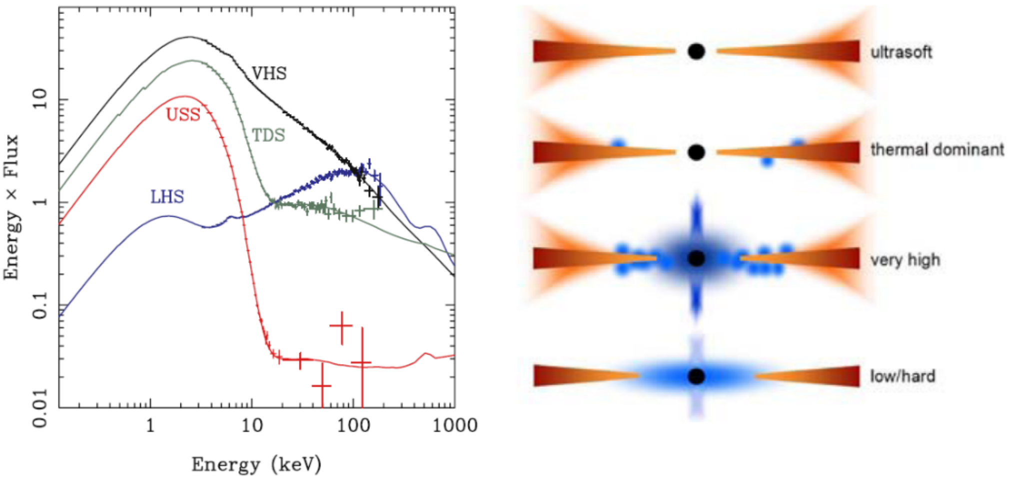

Figure 1.5: Left: X-ray spectra of the BHXB GRO J1655−40 in the very high state (black), the low/hard state (blue), the high/soft state (green), and the ultrasoft state (red; an extreme high/soft state with little contribution of the hard X-ray component). Right: Picture of the inner disk structure in each state. The standard disks and disk winds are shown in red, and the hot inner flows, coronae above the disks and jets are in blue (Done et al., 2007).

The spectral evolution of BHXBs is not solely determined by the luminosity, however. Figure 1.6 presents the hardness-intensity diagram of a typical BHXB for an outburst, in which the leftmost and rightmost sides correspond to the high/soft and low/hard states, respectively. The transition from the low/hard state to the high/soft state (called the hard-to-soft transition) normally occurs at a higher luminosity than that from the high/soft state back to the low/hard state (the soft-to-hard transition; Miyamoto et al., 1995; Nowak, 1995), and consequently a BHXB produces a counter-clockwise "q"-shaped track in the hardness-intensity diagram over an outburst (e.g.,

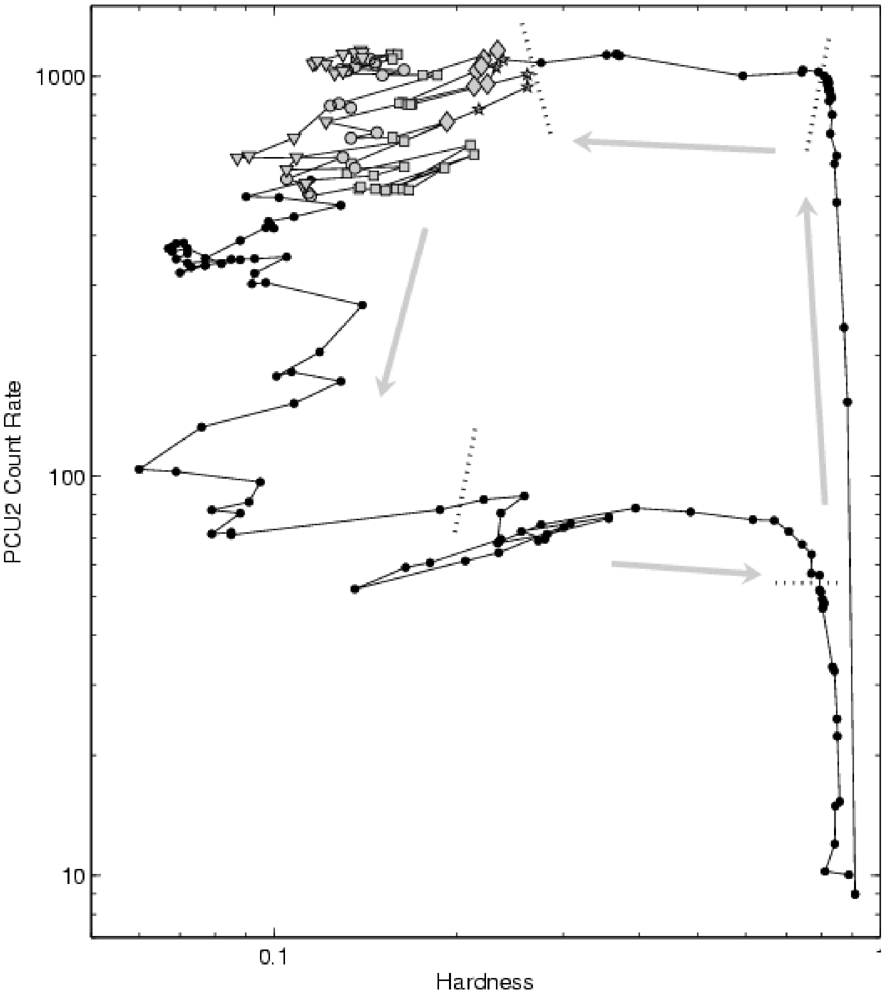

Figure 1.6: Hardness-intensity diagram of the BHXB GX339−4 in the 2002–2003 outburst (Belloni et al., 2005). The dotted lines briefly correspond to the major state transitions: hard to intermediate (top right), intermediate to soft (top left), soft to intermediate (bottom left), intermediate to hard (bottom right). The upper branch contains the very high state. The arrows indicate the general time evolution along the outburst.

Fender et al., 2004; Homan & Belloni, 2005). The luminosity at the hard-to-soft transition can vary from source to source, or even for the same BHXB during different outbursts, while the soft-to-hard transition is suggested to take place at almost the same bolometric luminosity, ≈2% $L_{\rm Edd}$[1] (Maccarone, 2003). The mechanism of this hysteresis is not fully understood, but probably described by dramatic changes in the structure of accretion flow due to the violent hydrogen ionization instability, which makes the mass accretion rate change faster than the viscous timescale in the geometrically thin disk (Gradstone et al., 2007).

The X-ray spectral shape of a BHXB is believed to reflect the geometry of the inner accretion disks, which differs significantly in each state (see, e.g., McClintock & Remillard 2006; Done et al. 2007, for recent reviews). The next three subsections describe the detail of the spectral properties and the inner disk structures in the high/soft state, the low/hard state, and the very high state.

1.3.2 High/soft State

The high/soft state is seen at ∼1–10% $L_{\rm Edd}$, in which the Xray spectrum is dominated by a soft X-ray component below 10 keV. This component is well described by the thermal emission from the optically-thick, geometrically-thin accretion disk (the standard disk; Shakura & Sunyaev, 1973). In addition, a weak power-law tail is often observed above ∼10 keV (see Fig. 1.5), extending to the gamma-ray band with a photon index of ∼2. This is likely produced by Compton scattering of the disk emission by non-thermal electrons somewhere above the disk.

The standard disk model is a steady, axisymmetric Keplerian accretion disk model, in which the viscosity is assumed to scale with the total pressure. By using the equation of the vertical hydrostatic balance, combined with the conservations of mass, momentum, energy, and angular momentum, the relation between disk flux (F) and radius (r) is derived as

$$F = \sigma T_{\rm eff}^4 = \frac{3GM\dot{M}}{8\pi r^3}\left(1 - \sqrt{\frac{r_{\rm in}}{r}}\right), \tag{1.2}$$

---

[1] $L_{\rm Edd}$ is the Eddington luminosity (or the Eddington limit): $4\pi G m_{\rm p} c M_{\rm BH}/\sigma_{\rm T}$, where $m_{\rm p}$, c, $M_{\rm BH}$, and $\sigma_{\rm T}$ represent the proton mass, the speed of light, the black hole mass, and the Thomson scattering cross-section, respectively. This is the maximum luminosity that a spherically accreting object can achieve. It is derived by balancing radiation pressure to gravity.

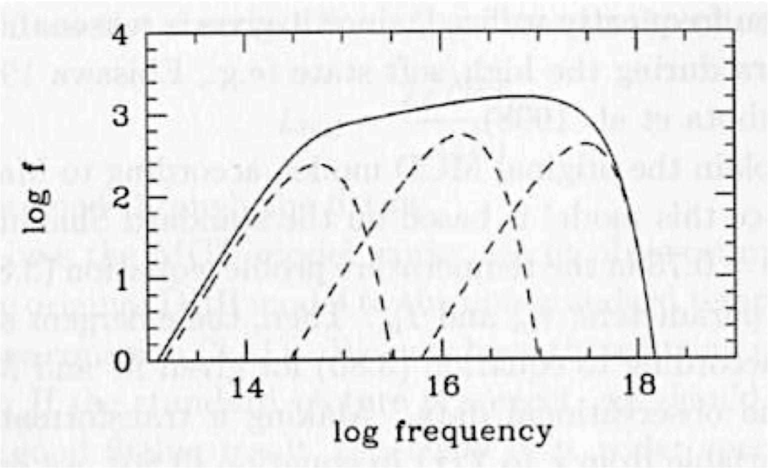

Figure 1.7: Typical spectrum of the standard disk (Kato et al., 2008). The abscissa is the frequency ν and the ordinate is the observed flux in arbitrary units. $T_{\mathrm{eff}} \propto r^{-3/4}$ is assumed. The parameters are $M = 10M_{\odot}$, $\dot{M} = 10^{18}$ g sec^{-1}, $r_{\mathrm{in}} = 6R_{\mathrm{g}} = 9 \times 10^{6}$ cm (where R_{g} is the gravitational radius, GM/c^2), and $r_{\mathrm{out}} = 10^{11}$ cm, corresponding to the disks in BHXBs. The blackbody emission from the inner disk region locates in the soft X-ray band.

where σ, T_{eff}, $\dot{M}$, and r_{in} represent the Stefan-Boltzmann constant, the effective temperature, the mass accretion rate at the radius r, and the inner radius of the disk, respectively. As illustrated in Figure 1.7, the total spectrum of the standard disk is formed by a superposition of blackbody radiation at different temperatures emitted from each radius of the disk. In X-ray astronomy, an approximated version of Equation 1.2 is often used, in which the square root term is ignored. This is called the multi-color disk (MCD) model (Mitsuda et al., 1984), where T_{eff} is exactly proportional to r$^{-3/4}$. The luminosity of the disk is thus expressed as

$$L_{\mathrm{disk}} = 2\int_{r_{\mathrm{in}}}^{\infty} 2\pi r \sigma T_{\mathrm{eff}}^{4}\, dr = 4\pi r_{\mathrm{in}} \sigma T_{\mathrm{in}}^{4}, \tag{1.3}$$

where T_{in} is the temperature at r_{in}[1]. The observed flux is given by

$$F_{\mathrm{obs}} = \frac{8\pi r_{\mathrm{in}}^{2} \cos i}{3T_{\mathrm{in}} D^{2}} \int_{T_{\mathrm{out}}}^{T_{\mathrm{in}}} \left(\frac{T}{T_{\mathrm{in}}}\right)^{-\frac{11}{3}} B(T)\, dT, \tag{1.4}$$

where $B(T)$, T_{out}, and D are the Planck function, the disk temperature at the outer edge, and the distance of the source, respectively.

---

[1] Here the disk is assumed to extend to infinity.

Because the inner temperature and the disk flux are determined from the disk spectra, the inner radius can be estimated via Equation 1.4, if the distance and inclination angle are given in advance. Many previous studies suggest that the inner disk radius stays constant during the high/soft state, regardless of the significant change in X-ray luminosity (e.g., Ebisawa et al. 1993; Kubota & Makishima 2004; Steiner et al. 2010; Shidatsu et al. 2011a). This indicates that the standard disk stably extends down to the innermost stable circular orbit (ISCO). The ISCO locates at $6R_\mathrm{g}$ (where R_g represents the gravitational radius, GM/c^2) in a Schwarzschild black hole (i.e., a non-rotating black hole). The radius of the ISCO monotonically depends on the black hole spin; it varies from $6R_\mathrm{g}$ down to $1R_\mathrm{g}$, corresponding to the case of a maximally rotating Kerr black hole.

Because the inner edge of the standard disk in the high/soft state locates at the ISCO, it can be used to estimate the black hole spin. Note that the black hole mass should be determined in advance to scale the inner radius obtained from observed disk spectra in the unit of the gravitational radius. However, it has to be taken in mind that the MCD model is only a simple approximation of the disk spectrum (see, e.g., Kubota et al. 2010; Kolehmainen et al. 2011; Shidatsu et al. 2011a). The real disk spectrum around a black hole should deviate from the MCD spectrum due to the inner boundary condition and relativistic effects including gravitational redshift, beaming, and light bending, which become particularly important for a rapidly spinning black hole. Therefore, for accurate spin measurements, it is necessary to model the disk spectra with taking into account the effects of the black hole spin self-consistently. In this way, black hole spins are estimated in several BHXBs (e.g., McClintock et al., 2006; Shafee et al., 2006).

1.3.3 Low/hard State

BHXBs in the low/hard state exhibit a hard, power-law shaped X-ray spectrum with a photon index of <2 and an exponential cutoff at ≈ 100 keV. This spectral shape is generally described as the unsaturated Compton scattering of the soft X-ray photons from the accretion disk by thermal electrons in hot inner flow or corona. As explained in Rybicki & Lightman (1979), the power-law spectral index of the unsaturated Comptonization is determined by the Compton y parameter, which is given by

$$y = \frac{4kT_\mathrm{e}}{m_\mathrm{e}c^2}\,\mathrm{Max}\left(\tau_\mathrm{es}, \tau_\mathrm{es}^2\right), \tag{1.5}$$

where k, m_e, T_e, and τ_es are the Boltzmann constant, the electron mass, the electron temperature, and the electron-scattering optical depth, respectively[1]. The cutoff energy corresponds to $\approx kT_\mathrm{e}$. Recent studies suggest that the Comptonizing cloud in the low/hard state has a more complex structure than that assumed in a single zone, spherical model. *Suzaku* high quality wide-band data enabled precise and detailed modeling of the Comptonized spectra, and Takahashi et al. (2008), Makishima et al. (2008), Shidatsu et al. (2011b), and Yamada et al. (2013a) found that two Comptonization components that have different optical depths are required to reproduce the time-averaged spectra in the bright low/hard state.

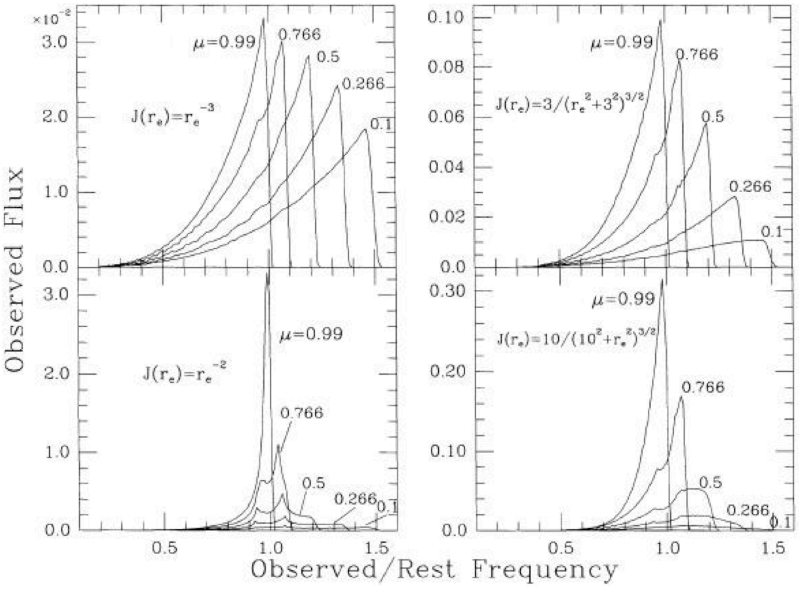

Figure 1.8: Relativistic disk emission line profile with various radial emissivity laws $J(r_\mathrm{e})$. The inclination angles ($\mu = \cos i$) are marked in each figure. The fluxes in all cases are given in the same arbitrary units (Laor, 1991).

In the low/hard state, the direct standard disk component is weak or not detected at all, and the inner temperature is lower than that in the high/soft state. Therefore, it is usually difficult to constrain the inner disk radius by analyzing disk spectra. Instead,

---

[1] This is the non-relativistic case. For the relativistic case, $y = 16(kT_\mathrm{e}/m_\mathrm{e}c^2)^2\,\mathrm{Max}(\tau_\mathrm{es}, \tau_\mathrm{es}^2)$.

another approach that uses the reflection features originated from the inner parts of optically-thick accretion disks, is often adopted to measure r_{in} in the low/hard state. Typical low/hard state spectra have a Compton hump above 10 keV created by the disk reflection (e.g., Ueda et al., 1994). As a part of the reflection component, a strong iron K-α fluorescent emission line is also detected at $\approx$6.4 keV, which can be a good tracer of the inner edge of the standard disk. As presented in Figure 1.8, emission lines from the vicinity of black holes are broadened and skewed due to the relativistic effects (Fabian et al., 1989; Laor, 1991). Using relativistic disk line models, previous studies suggested that the standard disk does not extend to the ISCO in the low/hard state and eventually extends inward according to the increase of X-ray luminosity (Tomsick et al. 2009; Shidatsu et al. 2011b; Kolehmainen et al. 2014). However, the geometry of the inner disk in the low/hard state is still controversial, particularly at relatively high luminosities. Miller et al. (2006a) and Reis et al. (2010) detected smeared iron-K lines in several BHXBs including GX 339$-$4 and GRO J1655$-$40 and argued that the standard disk extends to the ISCO, while the re-analysis of the GX 339$-$4 data by Done et al. (2010) suggested that the disk is truncated over $\gtrsim$20 R_{g}.

1.3.4 Very High State

The very high state is seen in high mass accretion rates near the Eddington limit, in which both the disk and Comptonization components strongly contribute to the X-ray spectra. The structure of the inner accretion flow in very high state is poorly understood, because this state appears only in a short time in an outburst when a source almost reaches its peak X-ray luminosity, and is difficult to observe. Moreover, the strong Compton-scattering of the standard disk emission by an energetic electron corona (e.g., Gierliński & Done, 2003; Kubota & Done, 2004) hampers direct measurements of the intrinsic disk parameters. Nevertheless, several recent studies report that the standard disk is slightly truncated (Kubota & Done 2004; Done & Kubota 2006; Tamura et al. 2012; Hori et al. 2014). This indicates that the standard disk in this state, as well as the low/hard state, is truncated, and that the inner part is replaced by a hot accretion flow at higher luminosities than the high/soft state. It is also suggested that the Comptonizing corona has both thermal and non-thermal electrons (e.g., Gierliński et al., 1999; Gierliński & Done, 2003), although it is not clear whether it is composed of two separate components or is a single cloud with a hybrid electron distribution.

1.3.5 Timing Behavior

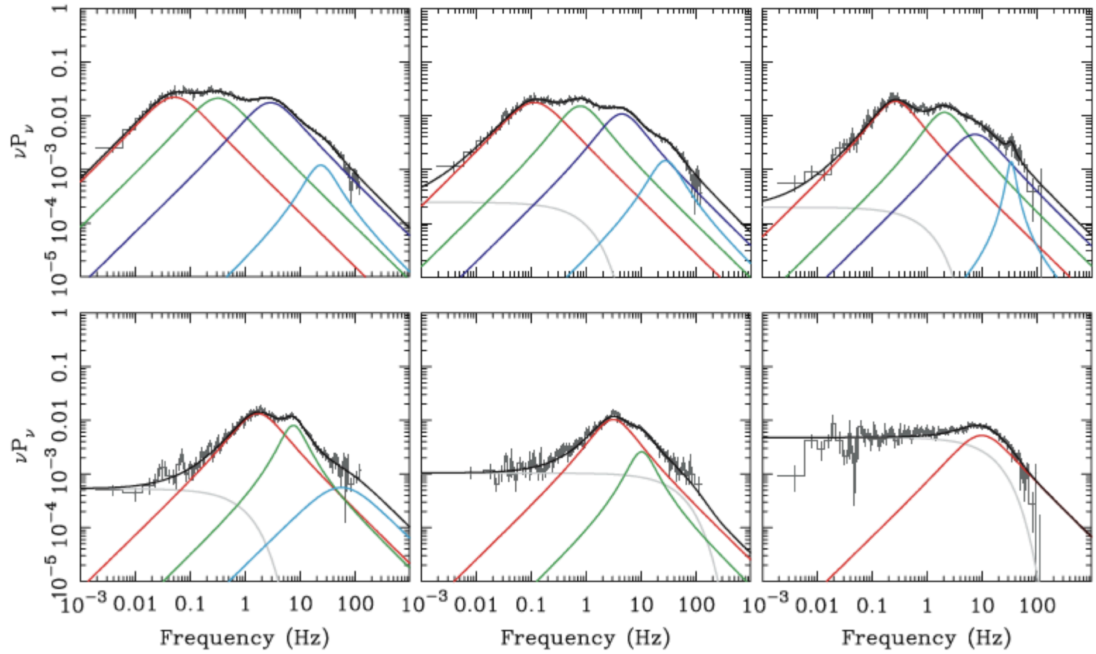

Figure 1.9: The evolution of the PDS in Cyg X-1 as it makes a transition from the low/hard to the high/soft state, together with the individual Lorentzian components. The noise component shown as the grey line is not seen in transient BHXBs (Done et al., 2007).

The properties of fast-time variability of BHXBs are also remarkably different in each state. Figure 1.9 presents the evolution of the power density spectrum (PDS) of Cyg X-1 in making a transition from the low/hard state to the high/soft state. In the low/hard state, BHXBs show noisy light curves on time scales of up to hundred seconds. Their PDSs are roughly characterized by the so-called band-limited noise with a flat profile in the νP_ν spectrum ($\nu P_\nu \propto \nu^0$) within the low and high frequency breaks, below and above which the power declines as $\nu P_\nu \propto \nu^1$ and $\nu P_\nu \propto \nu^{-1}$, respectively. In addition, quasi-periodic oscillations (QPOs) are sometimes detected on the band-limited noise. Extracting the energy spectra of the pure QPO and band-limited noise components, Axelsson et al. (2005) and Axelsson et al. (2014) found that these fast variabilities are produced by Comptonized emission from the vicinity of the black hole.

The noise profile in PDSs is better described as a superposition of multiple Lorentzians (Belloni & Hasinger, 1990; Belloni et al., 2002; Nowak, 2000). These structures can be reproduced by the superposition of “shots” (flare like events) seen in the low/hard state light curves on the ∼1-sec timescale (Negoro et al., 2001). The “shots” are thought to be related to density fluctuation of advection-dominated accretion flow inside the inner edge of the standard disk (e.g., Manmoto et al., 1996). Yamada et al. (2013b) have recently found more rapid changes in optical depth and electron temperature of the Comptonized corona at the peaks of shots on ∼0.1-sec timescale and suggested that it originates in flares powered by magnetic reconnections.

In contrast, fast variabilities are typically weak and no QPOs are seen in the high/soft state, where the constant standard disk emission dominates the X-ray flux (e.g., Homan et al., 2001). The low-frequency break of the band-limited noise seen in the low/hard state moves toward higher frequencies as the X-ray luminosity increases, and the PDS profile is smoothly connected to that in the high/soft state through the intermediate or very high state (van der Klis 2004; Axelsson et al. 2005). This implies that the low-frequency break traces the truncation radius of the standard disk. Previous studies reported that the QPO frequencies are correlated to the spectral index and the disk flux (e.g., Sobczak et al. 2000; Titarchuk & Fiorito 2004; Shaposhnikov & Titarchuk 2007), implying that the QPOs are also coupled with the inner disk structure. These characteristics support the idea that the standard disk is truncated in the low/hard state and the inner edge moves inward to reach the ISCO as the luminosity increases (Done et al., 2007; Ingram & Done, 2012).

1.4 Outflows from Black Hole X-ray Binaries

1.4.1 Ionized Absorbers and Disk Winds

Recent high-energy-resolution soft X-ray detectors, such as X-ray CCDs and grating spectrometers, discovered highly ionized blue-shifted absorption lines that originate in the “disk wind” (Figure 1.10), outflowing with a speed of $\lesssim$1000 km from the outer region of the accretion disks (e.g., Ueda et al. 1998; Kotani et al. 2000; Miller et al. 2006a; Kubota et al. 2007; Ponti et al. 2012). They seem to have a cylindrical geometry, because the absorption lines are only detected in sources with high ($\gtrsim$60°) inclination angles and do not show significant variability dependent on their orbital phases. Importantly, the mass loss rate of a disk wind is comparable with or even several to a few dozens times larger than the mass accretion rate (Ueda et al. 2004;

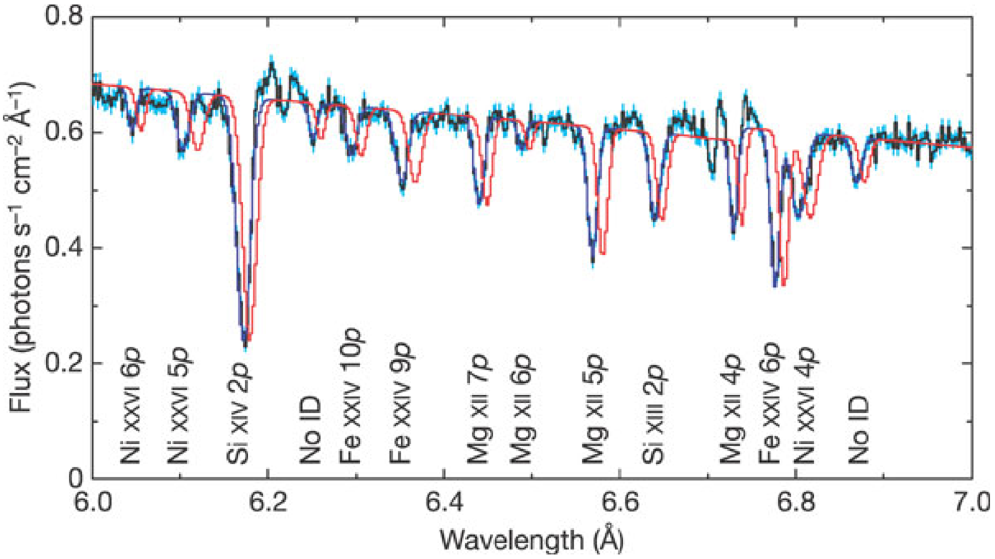

Figure 1.10: *Chandra* high resolution spectrum of GRO J1655−40 (Miller et al., 2006a). Highly ionized absorption lines originating in the disk wind are clearly seen. The best-fit phenomenological model (local continuum+Gaussian line functions) are presented in blue. The model in the rest frame is shown in red, illustrating that the observed absorption lines are blue-shifted.

Neilsen et al. 2011), suggesting that the disk wind would affect the properties of the inner region of the accretion disks and play a critical role on accretion disk physics.

There are three main mechanisms proposed for driving the disk winds in BHXBs: thermal, radiation pressure, and magnetic driving. Radiation pressure mechanism is expected to operate effectively only in high mass accretion rates (at $\gtrsim L_{\rm Edd}$). Kotani et al. (2000) detected absorption lines in the very luminous BHXB GRS 1915+105 that can be interpreted as a radiation driven wind. Thermally-driven winds are likely the most plausible scenario for normal disk winds in BHXBs. They are generated on the surface of the outer parts of the disks heated due to Compton scattering by illuminating X-ray photons (Begelman et al., 1983). Such a wind can be launched from the Compton radius,

$$R_{\rm C} \sim 10^{10}\ {\rm cm} \left(\frac{M}{M_\odot}\right) \left(\frac{T_{\rm C}}{10^8{\rm K}}\right) \sim 10^{12}\ {\rm cm}, \tag{1.6}$$

(where $T_{\rm C}$ is the Compton temperature), above which the Compton-heated gas overcomes local gravity. This would be an overestimate, however, and improved analyses predict that thermally-driven winds could be launched at a factor of 5–10 smaller radii

(Begelman et al., 1983; Woods et al., 1996). The radius of observed disk winds (R) can be estimated from the formula of the ionization parameter ξ, an indicator of the ionization stage,

$$\xi = \frac{L_{\rm X}}{n_{\rm H} R^2} = \frac{L_{\rm X}}{N_{\rm H} R} \frac{\Delta R}{R}, \tag{1.7}$$

where $n_{\rm H}$, $N_{\rm H}$, $L_{\rm X}$, and ΔR represent the hydrogen number density, the hydrogen column density, the ionizing X-ray luminosity, and the length of the absorber, respectively. The observed column density and an assumption of $\Delta R \sim 1$ (an extended wind) are usually used to derive R, while $n_{\rm H}$ can be directly measured when density-sensitive absorption lines are detected. In all cases but one, disk winds in normal BHXBs have larger distances than the Compton radii and thus consistent with thermally-driven winds. The exceptional case was *Chandra* observation of GRO J1655−40 in 2005 April (Miller et al., 2006a, 2008), in which the launching radius was estimated to $\approx 10^9$ cm, which is more than one order of magnitude smaller than the Compton radius. It was therefore interpreted as a magnetic-driven wind, although a thermally-driven scenario would not be ruled out if the wind is optically-thick (Shidatsu & Done, in prep).

High inclination systems often exhibit quasi-periodic dips accompanied by spectral hardening in their light curves. It is generally believed that the dips are caused by absorption of the X-ray emission from the central source with a dense structure in outer disks such as the "bulge", which is formed by the accretion stream from the companion star impacting the rim of the disk (see e.g., White & Swank, 1982). Previous studies showed that dipping spectra are well reproduced by a partial absorption by neutral material (e.g., Marshall et al., 1993). While this approach was successfully applied in many sources including both neutron star and black hole X-ray binaries, another explanation has recently been proposed; Boirin et al. (2005) and Díaz Trigo et al. (2006) successfully described both non-dipping and dipping spectra of neutron-star low mass X-ray binaries, using a single photo-ionized absorption model with different column densities and ionization parameters. It is suggested that absorption dips are generally produced by ionized gas of a lower ionization state and a higher column density than the disk winds.

1.4.2 Jets from Black Hole X-ray Binaries

Highly transient relativistic jets are sometimes detected in the hard-to-soft transitions. Radio interferometer resolved a core and oppositely directed knots moving with appar-

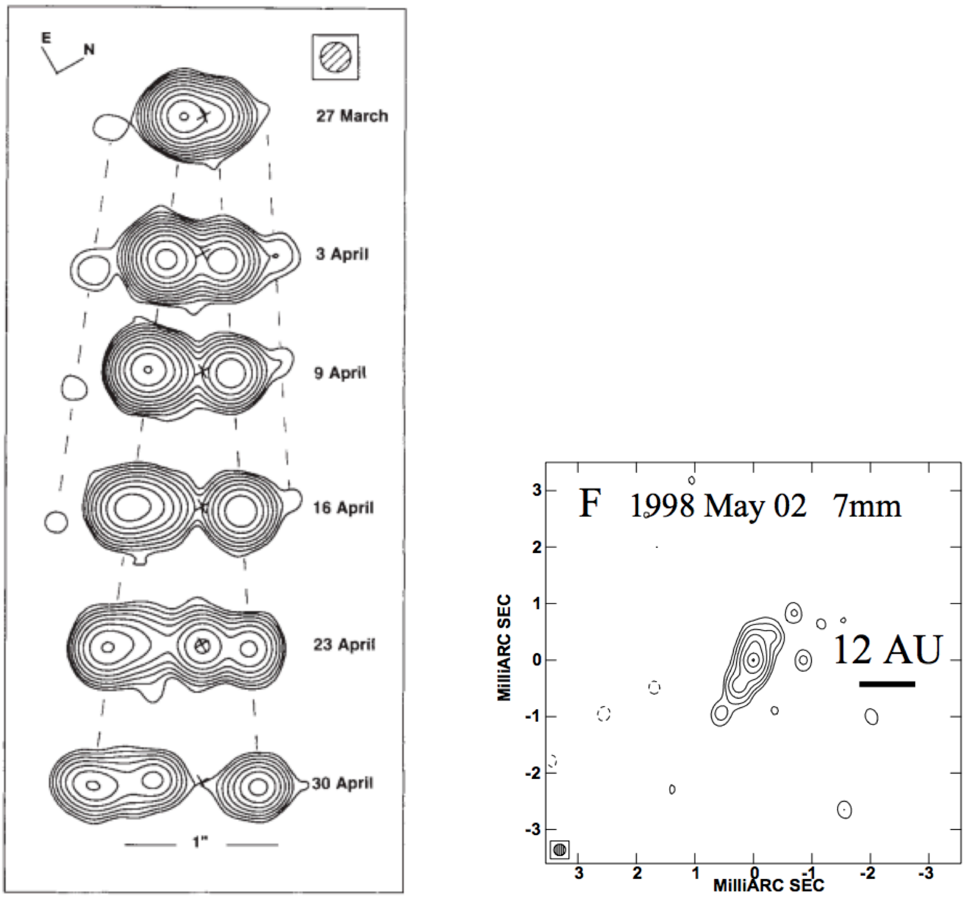

Figure 1.11: VLA images of a transient jet (left; Mirabel & Rodríguez, 1994) at the 3.5 cm wavelength and a compact jet (right; Dhawan et al., 2000) at 7 cm observed in GRS 1915+105. The radio condensations of the transient jet are moving away from the core (marked with small crosses) in the left panel. Note that the spatial resolution in the right panel is much better than that in the left panel.

ently superluminal speeds (e.g., Mirabel & Rodríguez 1994; Hjellming & Rupen 1995, and see Figure 1.11) to a projected distance of $\gtrsim$0.01 pc (Mirabel & Rodríguez, 1999). Similar knots were discovered in the X-ray band as well (Corbel et al., 2002). The jets often show large flux ratios between the two ejecta due to relativistic beaming. The true bulk velocity of the jets was found to exceed ∼90% of the speed of light, which is estimated from the apparent projected speeds of the approaching and receding sides of the jets, by assuming that they are ejected at the same time and travel with equal velocities. Relativistic jets may carry baryons. Díaz Trigo et al. (2013) have recently reported the detection of blue- and red-shifted X-ray emission lines from relativistic jets in 4U 1630−472. This is the first evidence of baryonic jets in canonical transient BHXBs, while such jets have been observed in the peculiar source SS 433, which is thought to be a persistent supercritical accretor (Watson et al. 1986; Matsuoka et al. 1986; Kawai et al. 1989; Kotani et al. 1994; Kubota et al. 2010).

There is a different type of jet in BHXBs: a steady compact jet ubiquitously seen in the low/hard state (e.g., Fender et al., 1999; Fender, 2001), extending only less than a few ten AU (Dhawan et al., 2000). The spectral energy distribution (SED) in the low/hard state has an almost flat profile in the radio band, like those observed from active galactic nuclei (AGN). This is described by the conical jet model (Blandford & Königl, 1979), where the flat spectrum is produced by the superposition of the synchrotron emission from each location in the jets. The conical jet model predicts a break of the flat component above which the jets are no longer optically-thick, even at the jet base. Observations at this break frequency, which corresponds to the peak flux density of the synchrotron emission from the innermost part of the jets, can give key information to understand the energetics of the jets and the structure of the jet base. This break was actually observed in the millimeter to infrared band (Corbel & Fender, 2002; Gandhi et al., 2011; Russell et al., 2003), and the synchrotron flux density was found to eventually decline above the break as a power law with an index >1 in SED units. Furthermore, Shidatsu et al. (2011b) and Chaty et al. (2011) successfully estimated the magnetic field and the size of the jet base as $\sim 5 \times 10^4$ G and $\sim 10^8$ cm, respectively, from the synchrotron luminosities at break frequencies in GX 339−4 and XTE J1550−564. Previous observations discovered a strong, positive linear correlation between X-ray and radio fluxes over several orders of magnitude in the low/hard state, implying a coupling between accretion flow and jets (e.g., Corbel et al. 2000; Gallo et al. 2003; Corbel et al. 2013). A similar correlation was found between X-ray and near-infrared fluxes as well (Coriat et al., 2011; Shidatsu et al., 2011b). There correlations could be extended to AGN by taking into account the black hole mass, implying a possible universal scaling law across all mass scales (Merloni et al. 2003; Falcke et al. 2004).

Jets from black holes are generally considered to be formed and powered by a highly twisted magnetic field (e.g., Benford, 1978; Blandford & Payne, 1982). Polarimetry of the synchrotron emission gives us essential information to understand the magnetic structure of the compact jets in the low/hard state. Previous radio observations at ∼1 GHz detected linearly polarized components at a level of a few % with an almost constant polarization angle (e.g., Han & Hjellming 1992; Corbel et al. 2000). These results indicate the stability of the magnetic field configuration for the emitting regions.

1.4.3 State Dependence of Outflows

Growing evidence suggests that the compact jets are always present in the low/hard state, while they are quenched and the radio fluxes decrease to undetectable levels in the high/soft state (Tananbaum et al. 1972; Fender et al. 1999; Dhawan et al. 2000; Fender 2001; Gallo et al. 2003). This indicates that the formation of compact jets is tightly related to the accretion disk structure. The ejection of transient extended jets, which occurs in the hard-to-soft transitions, is also likely linked to the evolution of accretion disks. Figure 1.12 shows a unified model of disk evolution and jet formation/suppression proposed by Fender et al. (2004). In this model, there is the "jet line" in the hardness-intensity diagram (solid vertical line in Fig. 1.12) determining the presence and absence of compact jets. As a source approaches this boundary from a harder spectral state to a softer state (i.e., from the right side to the left side in Fig. 1.12), the compact jet properties change and finally most powerful jet is launched, which corresponds to the transient extended jet. However, the actual jet physics would be more complicated; recent studies have found that the position in the diagram where compact jets are quenched varies in different outbursts of the same sources, and that transient jets are not always ejected in the hard-to-soft transitions (Miller-Jones et al. 2012; Rushton et al. 2012; Paragi et al. 2013).

Disk winds are also dependent on the X-ray states. BHXBs having winds in the high/soft and intermediate states rarely exhibit absorption lines in the low/hard state (Takahashi et al. 2008; Ueda et al. 2010; Blum et al. 2010). This has recently been confirmed through a systematic study of all the *Chandra*, *XMM-Newton*, and *Suzaku* data of BHXBs (Ponti et al., 2012, see Figure 1.13). There are two possible interpretations for the absence of the absorption lines: (1) disk winds are somehow quenched, or (2) disk winds are present in the low/hard state, but are fully ionized by strong hard X-ray illumination and thus become undetectable (Ueda et al. 2010; Díaz Trigo et al. 2014). Ponti et al. (2012) suggested that the latter is unlikely, because even at the same luminosities the absorption lines are observed in the high/soft state but not

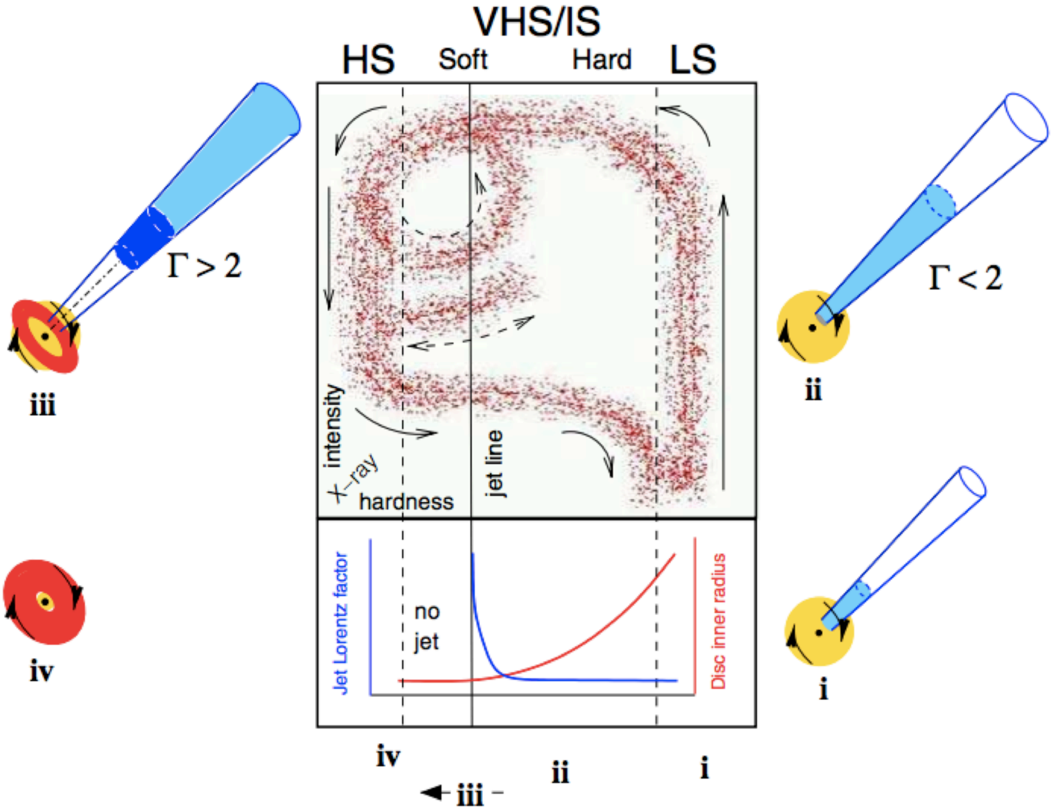

Figure 1.12: A simplified model of disk-jet coupling in BHXBs (Fender et al., 2004). The upper central box panel represents a typical X-ray hardness-intensity diagram of BHXBs, where ”HS” indicates the high/soft state, ”VHS/IS” the very high or intermediate state, and ”LS” the low/hard state. In this diagram, X-ray hardness increases to the right and intensity upwards. The lower panel indicates the variation of the bulk Lorentz factor Γ of the outflow (blue) and inner disk radius (red) with respect to hardness. The dashed loop and dotted track indicate the paths that GRS 1915+105 and some other transients take in repeated hardening and softening. The sketches around the outside illustrate a concept of the relative contributions of jet (blue), hot electron corona (yellow) and accretion disk (red) at these different stages.

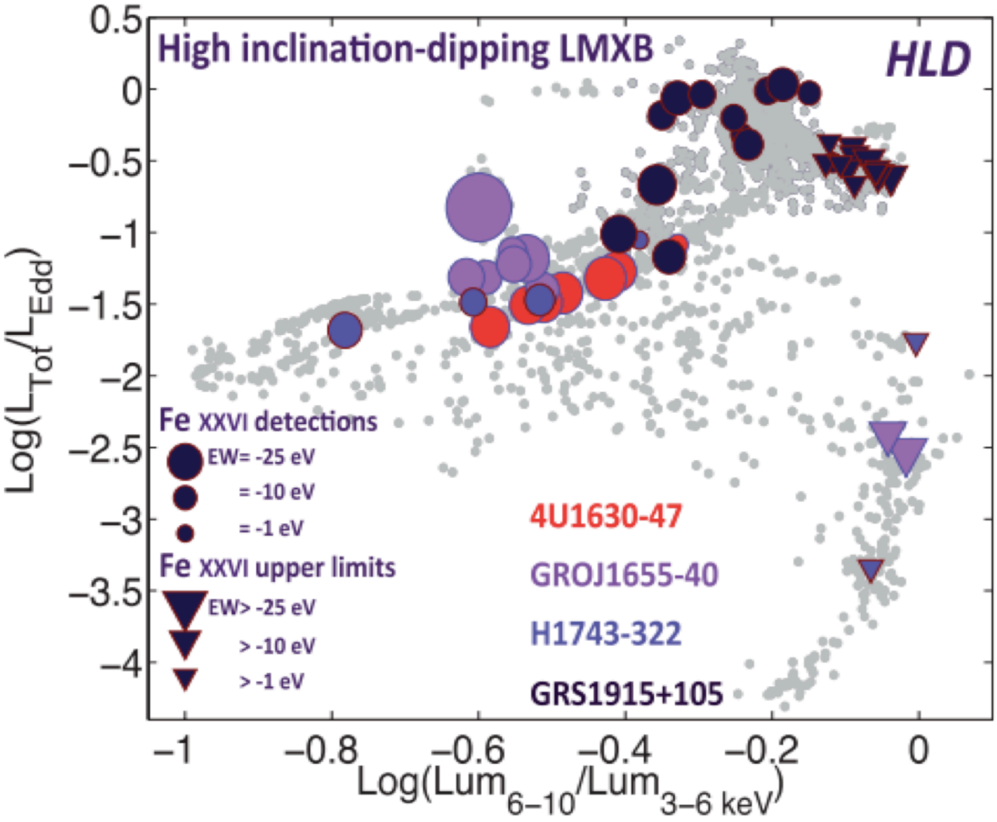

Figure 1.13: Hardness intensity diagram of high inclination BHXBs, on which the presence and absence of ionized absorption lines are superimposed (Ponti et al., 2012). The circles indicate *Chandra*, *XMM-Newton*, and *Suzaku* observations during which the Fe XXVI absorption line was detected. The size of the symbol is proportional to the equivalent width of the line. The triangles show the non-detections. Their size is proportional to the upper limit on the Fe XXVI line. The different colors indicate results from different sources.

in the low/hard state, although they did not take into account the spectral hardening. Theoretically, Chakravorty et al. (2013) have recently showed that disk winds could be thermodynamically unstable in the low/hard state, making it difficult to detect ionized absorption lines.

The observed state dependence of wind absorption lines is opposite to that of compact jets (see above). Comparing the mass loss rate of the jets with that of the disk winds, Neilsen & Lee (2009) proposed a possible explanation of the observed anti-correlation; in the high/soft state, the disk winds carry enough mass away from the disk to halt the flow of matter into jets, while jets can be launched in low/hard state, in which the powerful disk winds are quenched. Note that, however, there is one observation in which a weak wind and a weak jet are quasi-simultaneously detected in the "low/hard" state of GRS 1915+105 (Lee et al., 2002), and therefore the physical mechanisms for producing and suppressing winds may not be directly linked to those for jets. Further simultaneous radio and X-ray observations in the low/hard state are necessary to investigate whether and how the jets and winds are physically coupled.

1.5 Motivation and Strategy of This Study

Transient BHXBs are ideal objects to study the fundamental physics around black holes. As described in the previous sections, following the dramatic changes in observed properties of BHXBs during outbursts enables us to understand the evolution of black hole accretion disks and outflows over wide range of mass accretion rates. Since their discovery, BHXBs have been extensively studied over several ten years. Nevertheless, many questions are still remain, such as:

- What is the physical properties and geometry of Comptonized corona and hot inner flow? At what luminosity is the hot flow replaced by the standard disk?
- In what range of mass accretion rate does the standard disk stably extend to the ISCO?
- What is the origin of the complex rapid X-ray variability and how is it associated with the evolution of the inner disk structure?
- What is the main driving mechanism of disk winds?

- What are the physical processes to accelerate gas to the relativistic speed and to form jets?
- How much mass and energy do winds and jets carry away and how much do they affect the inner disk structure?
- What makes the state dependence of ionized absorption lines?
- How are disk winds and jets linked to the evolution of the accretion disk structure?

To answer these major questions is important not only for its own sake, but also to understand the cosmological "co-evolution" of galaxies and supermassive black holes (SMBHs). Many authors report tight correlations between the masses of SMBHs and the properties of their host galaxies (e.g., Magorrian et al., 1998), indicating that they have grown up by interacting with each other. Recent observational and theoretical studies suggest that outflows from supermassive black holes may play a key role in the co-evolution (see Fabian, 2012, for a recent review). According to their results, enormous gravitational energy released by gas accreted onto supermassive black holes powers winds and relativistic jets, and the outflows could affect the interstellar medium and regulate star formation in the host galaxies. BHXBs are the best targets to study the basic physics of the black hole accretion and outflows, because they are simplest accreting black hole systems consisting of a star and a stellar-mass black hole, and evolving on human timescales. Thanks to their proximity, they are much brighter than accreting SMBHs in the X-ray band, and thus high quality data can be obtained.

Because it is difficult to predict when the outbursts of BHXBs begin, X-ray monitoring of all the transient BHXBs in the sky is critical to perform timely observations with high-sensitivity pointing satellites. For this purpose, I have participated in the mission team of *Monitor of All-sky X-ray Image* (*MAXI*) over five years. In 2012, *MAXI* detected outbursts of the BHXB H 1743−322 and the new black hole candidate MAXI J1305−704. On the basis of the information provided by *MAXI*, we successfully conducted follow-up observations with the Japanese X-ray satellite *Suzaku*, when the systems were active. Multiple observations with the NASA (National Aeronautics and Space Administration)'s satellite *Swift* were also carried out for MAXI J1305−704. In this thesis, I analyzed these X-ray data, with a particular focus on the inner disk structure and disk winds, both of which can be sensitively studied by fully utilizing the observing capabilities of *Suzaku* and *Swift* (see Chapter 2). To constrain the structure of outer accretion disks, properties of companion stars, and emission from jets (if present), we also conducted optical and near-infrared observations almost simultaneously to the X-ray observations.

1.6 Structure of the Thesis

This thesis is comprised as follows. Chapter 2 gives an overview of the X-ray observing facilities that we utilized in this work. Chapter 3 and 4 describe the observational studies of H 1743−322 and MAXI J1305−704, respectively. These two chapters are based on the publications Shidatsu et al. (2014) and Shidatsu et al. (2013). Chapter 5 provides a summary of the results and conclusions of the thesis. Throughout the thesis, we refer to the table by Anders & Grevesse (1989) as the solar abundances. The errors of spectral parameters correspond to the 90% confidence ranges for a single parameter, unless otherwise specified.

Part of the work was done in collaboration. All the near-infrared observations with *Infrared Survey Facility* (*IRSF*) that appear in this thesis were carried out by Dr. Takahiro Nagayama and visiting observers, Mr. Tatsuhito Yoshikawa, Dr. Noriyuki Matsunaga, Dr. Kohji Tsumura, Dr. Mai Shirahata, Dr. Sudhanshu Barway, Dr. Daisuke Suzuki, and Dr. Fumio Abe. Dr. Yuki Moritani performed optical observations with the *Kanata* telescope and made the reduction of the photometric data from *Kanata*. The *Suzaku* Time-of-Opportunity (TOO) observation of MAXI J1305−704 was triggered on the basis of the *MAXI-Suzaku* collaboration, while those of H 1743−322 were on the basis of an approved AO-7 proposal (Ueda, Shidatsu, et al.). The rest of the work was conducted by myself.

2

X-ray Observing Facilities

2.1 *Suzaku*

Suzaku (Mitsuda et al., 2007) is the fifth Japanese astronomy satellites (following Hakucho, Tenma, Ginga, and ASCA), launched in 2005 July from Japan Aerospace Exploration Agency (JAXA) Uchinoura Space Center. *Suzaku* carries three currently functioning X-ray charge-coupled-devise (CCD) cameras named the X-ray Imaging Spectrometer (XIS; Koyama et al., 2007), which detect X-ray photons of 0.2–12 keV, and a non-imaging collimated hard X-ray sensor called Hard X-ray Detector (HXD; Takahashi et al., 2007), composed of silicon PIN diodes and Gadolinium Silicate crystal (GSO) scintillators covering the 10–70 keV and 40–600 keV bands, respectively (Kokubun et al., 2007). The overview of *Suzaku* is shown in Figure 2.1, and the capability of the individual detectors are summarized in Table 2.1.

The XIS consists of frontside-illuminated cameras (FI-XISs; XIS-0 and XIS-3) and a backside-illuminated camera (BI-XIS; XIS-1)[1], which is more sensitive to soft X-rays below ≈1.5 keV than FI-XISs. FI- and BI-XISs are operated either in the normal two-dimensional mode or the P-sum mode, which compresses the image into one-dimension and provide much better time resolution than that of the former mode. The normal mode provides two options: the window option and the burst option. The former uses only a selected part of a CCD, while the latter adopts a reduced exposure time in the readout intervals. These options are useful to avoid photon pile-up in observing

---

[1] XIS-2, another backside-illuminated camera, was only usable until the unrecoverable damage in 2009 November possibly caused by micro-meteorite hits.

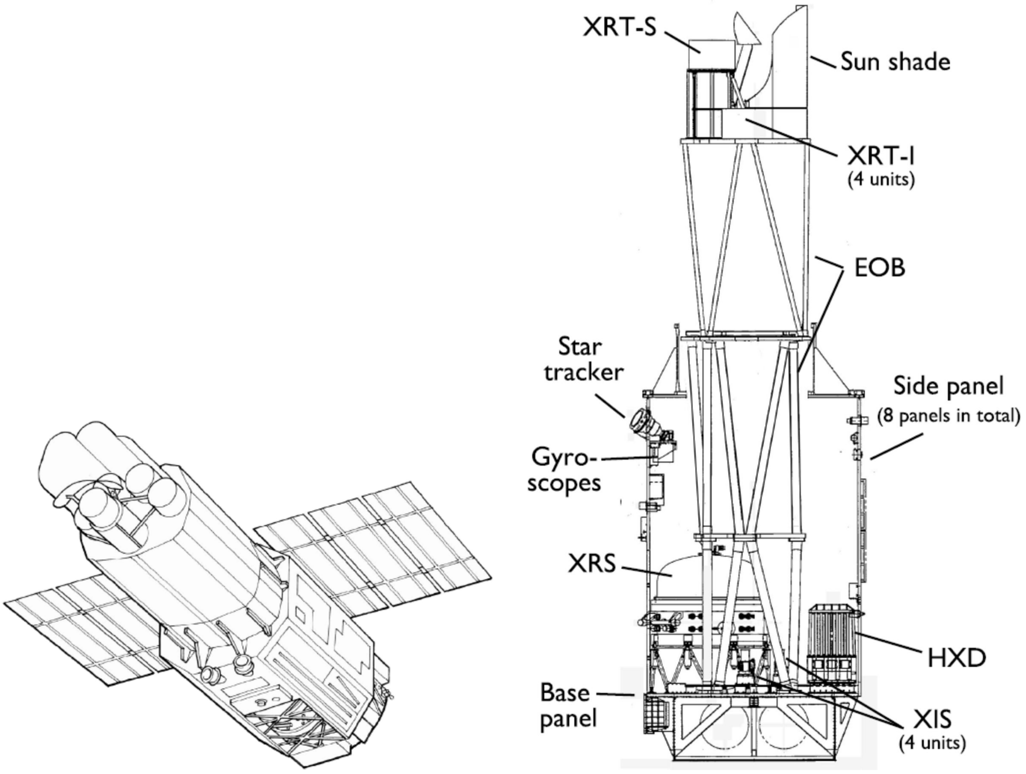

Figure 2.1: Left: Schematic view of *Suzaku*. Right: Internal Structures of *Suzaku*. Both pictures are taken from Mitsuda et al. (2007).

bright sources such as outbursting BHXBs. Each XIS is placed on the focal plane of a dedicated telescope called the X-ray Telescope (XRT; Serlemitsos et al., 2007). The XRTs, consisting of nested thin-foil conical mirrors, have large effective areas up to ≈10 keV (440 cm^2 at 1.5 keV and 250 cm^2 at 8 keV per telescope) and moderate angular resolution (≈2').

Combination of the XIS and HXD gives a very wide energy coverage from 0.2 to 600 keV. This is ideal to study the inner disk structure of BHXBs, as it allows to detect both the soft X-ray emission from the standard accretion disk and the hard X-ray component generated by Compton scattering of the disk emission by energetic electrons in the corona. Because BHXBs often exhibit large variability in X-ray spectra, it is critical to detect these two components simultaneously. Moreover, the good energy resolution below 10 keV enables to study the profiles of fluorescent iron lines, often seen in the soft X-ray spectra of BHXBs.

Parameter	**XIS**	**HXD**
Field of view	$17'$ ($13'$) at 1.5 keV (8 keV)	$17'.8 \times 17'.8$
Energy range	0.2–12 keV	10–70 keV (PIN) 40–600 keV (GSO)
Number of pixels	1024×1024	–
Pixel size	24 μm $\times$ 24 μm	–
Effective area	330 cm^2 (FI) 370cm^2 at 1.5 keV (BI)	160 cm^2 at 20 keV 260 cm^2 at 100 keV
Energy resolution (FWHM)	$\sim$130 eV at 6 keV	$\sim$3.0 keV (PIN) $7.6/\sqrt{E_{\rm MeV}}$% (GSO)
Time resolution	8 sec (normal mode)[a] 7.8 msec (P-sum mode)	61 μsec

Table 2.1: Main characteristics of the *Suzaku* XIS and HXD.

[a] The time resolution in the normal mode is reduced by a factor of 4 and 8 with 1/4 and 1/8 window options, respectively.

2.2 *MAXI*

Monitor of All-sky X-ray Image (*MAXI*; Matsuoka et al., 2009) is the Japanese all-sky X-ray monitor mounted onto the Japanese Experiment Module, Exposed Facility on the International Space Station (ISS). It was launched by Space Shuttle Endeavor in 2012 July and since then it has operated for over 5 years by the members of the *MAXI* mission team consisting of JAXA and Rikagaku Kenkyusho (RIKEN; Institute of Physical and Chemical Research), in collaboration with X-ray astronomy groups in more than several Japanese Universities. *MAXI* covers almost all sky for every ISS orbit of ≈92 minutes and monitor X-ray sources with an unprecedented sensitivity. The major goal of the *MAXI* mission is to detect new transients including BHXBs and monitor them as well as known X-ray sources. The information of transient events is quickly released to the astronomers over the world to encourage follow-up observations with pointing X-ray satellites and ground telescopes. Until now, *MAXI* has discovered several black hole candidates, such as MAXI J1659–152 (Negoro et al., 2010a), MAXI J1543–564 (Negoro et al., 2011), and MAXI J1305−704 (Morihana et al., 2013). In addition, *MAXI* gives us a unique opportunity to study the X-ray spectra of BHXBs continuously over a period from the onset of an outburst to its fading phase (see, e.g., Nakahira et al., 2010, 2014; Shidatsu et al., 2011a).

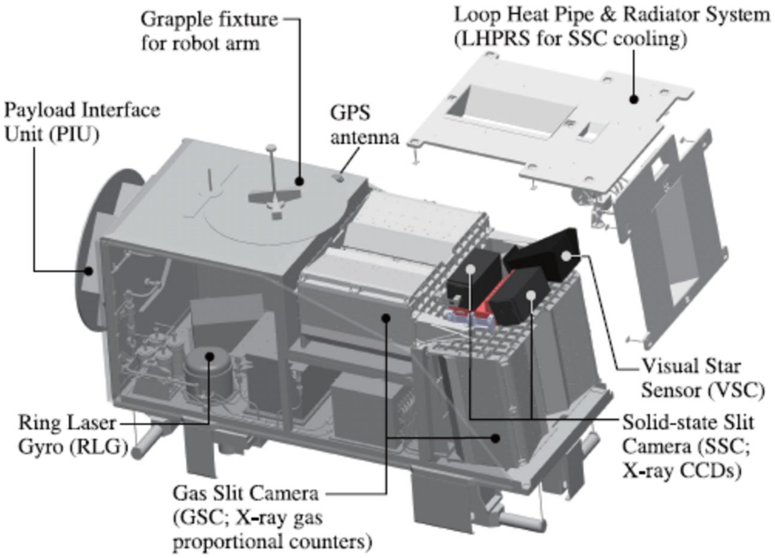

Figure 2.2: Overview of *MAXI*, taken from (Matsuoka et al., 2009). The total size and weight are 1.85 m × 0.8 m × 1 m and 520 kg, respectively.

Figure 2.2 presents the configuration of *MAXI*. *MAXI* has two different types of scientific instruments: the Solid-state Slit Camera (SSC; Tomida et al., 2011), which is composed of 16 X-ray CCDs covering 0.5–10 keV, and the Gas Slit Camera (GSC; Mihara et al., 2011), consisting of one-dimensional gas proportional counters sensitive to X-rays in the 2–30 keV band (see Figure 2.3). In this thesis, we use only GSC data, because the GSC has a larger detection area and is currently better calibrated than the SSC.

The GSC consists of six units that has two counters combined with slit & slat collimators, as presented in Figure 2.3. Three of them have their field of views (FoVs) in the horizontal direction and the rest three in the zenithal direction. Each counter has six parallel carbon-wire anodes with one-dimensional position sensitivity, to detect X-ray photons coming through a slit. The collimators limit the FoVs of the counters in the orthogonal direction of the wires. The GSC has a detection area of 5350 cm^2 in total and achieves higher sensitivity than any other previous all-sky monitors in the 2–20 keV band (see Table 2.2 for more detail of the GSC characteristics).

Parameter	**Value**
Number of counters[a]	12
Composition of gas	Xe + 1% CO_2
Energy range	2–30 keV
Total detection area[b]	5350 cm^2
Sensitivity	$\approx$20 mCrab[b,c]
Energy resolution	18% (at 5.9 keV)
Field of view[d]	$1^\circ.5 \times 160^\circ$
Slit area for a camera unit	20.1 cm^2
Detector position resolution	1 mm
Localization accuracy	$\sim 0^\circ.1$
Time resolution	0.1 msec (minimum)
Weight	160 kg

Table 2.2: Specifications of the Gas Slit Camera.

[a] Six counters observes the zenithal direction, while the rest observe the horizontal direction. A detector unit is composed of two counters whose FoVs are in the same direction. Each counter has its dedicated slit & slat collimator.

[b] When all twelve detectors are operative. Six of them are currently switched off due to the damage caused by discharged events.

[c] 5σ confidence level in one orbit in the 2–30 keV band. 20 mCrab $\approx 7 \times 10^{-10}$ erg cm^{-2} sec^{-1}.

[d] FWHM × full-FoV.

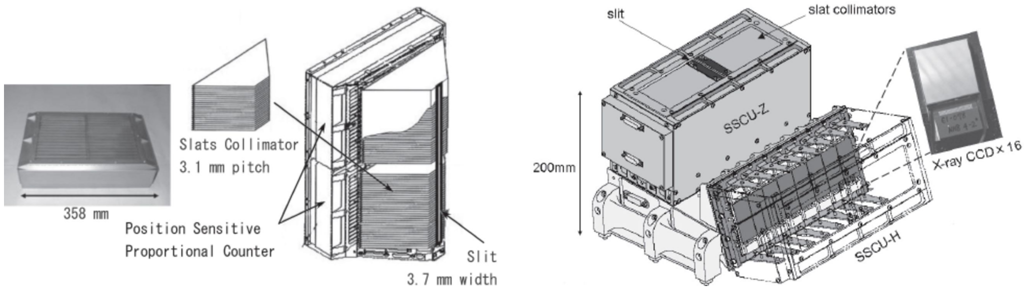

Figure 2.3: Scientific instruments on board *MAXI* (Matsuoka et al., 2009). Left: A GSC unit, consisting of two one-dimensional gas proportional counters (the leftmost picture) and their dedicated triangular slit & slat collimators. Right: The configuration of the SSC.

2.3 *Swift*

The *Swift* Gamma-ray Burst Explorer (Gehrels et al., 2004, Figure 2.4) is a multi-wavelength space observatory of NASA's, launched into orbit in 2004 November. The main goals of *Swift* mission is to determine the origin of GRBs and to probe early universe using GRBs. *Swift* monitors gamma-ray and hard X-ray sky to discover high energy emission from GRBs, and autonomously slews into the direction of the burst events to observe aftergrows in the optical, ultraviolet (UV), and soft X-ray bands.

Swift has three scientific instruments: the Burst Alert Telescope (BAT; Barthelmy et al., 2005), the X-ray Telescope (XRT; Burrows et al., 2005), and the Ultraviolet/Optical Telescope (UVOT; Roming et al., 2005). The main characteristics of the individual instruments are listed in Table 2.3. The BAT is a coded aperture instrument sensitive to 15–150 keV with a large FoV ($\approx$1.4 sr). It detects GRBs and localizes them with an accuracy of $\lesssim 4'$ within $\approx$20 seconds. This position information is immediately distributed to the astronomical community via Gamma-ray burst Coordinate Network (GCN) to promote follow-up observations. *Swift* slews to the position determined with the BAT as soon as possible so that the XRT and UVOT can observe the source. The XRT is a front-illuminated CCD camera, which utilizes a CCD chip and a mirror set developed for the EPIC MOS cameras on *XMM-Newton* and the JET-X on *Spectrum-X-Gamma*, respectively. The XRT is designed to cover the soft X-ray band from 0.2 keV to 10 keV with a good energy resolution (50–200 eV) and to measure burst positions with much more precisely (within a few arcsec) than those determined by the BAT.

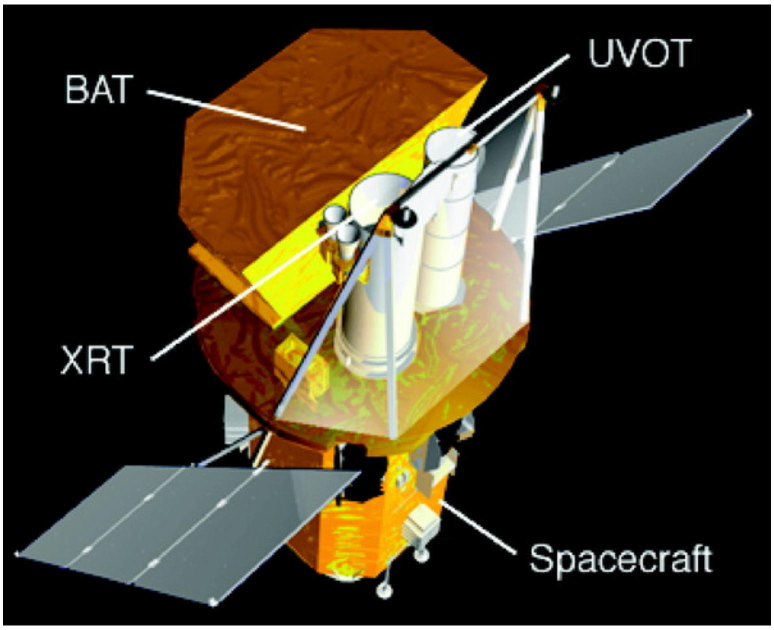

Figure 2.4: Image of the *Swift* satellite (Gehrels et al., 2004). The total weight is 1450 kg.

In addition to the normal operation mode, called the Photon Counting (PC) mode, the XRT provides two timing modes: the Windowed Timing (WT) mode, and the Photodiode (PD) modes. The WT mode sums photon counts of pixels in one direction (like the P-sum mode of the *Suzaku* XIS) to obtain a better time resolution (1.8 msec) than the PC mode, and therefore it makes only one-dimensional imaging. The PD mode integrates the counts over the entire CCD. It gives the best time resolution (0.14 msec), but the spatial information is totally lost. The UVOT, which is co-aligned with the XRT, is built on the basis of the Optical Monitor on *XMM-Newton*, and dedicated to observe the early aftergrows of GRBs in the optical and UV bands from 170 nm to 650 nm. It consists of a modified Ritchy-Chrétien optical configuration with a 30 cm primary mirror, and a fast readout, micro-channel plate (MCP) intensified CCD that records the information of individual photons. The UVOT have seven broadband filters for photometry, and low-resolution UV and optical grism for slitless spectroscopy of bright sources.

Parameter	**BAT**	**XRT**	**UVOT**
Detector type	CdZnTe detector with coded mask	Walter-I telescope & X-ray CCD	Ritchy-Chrétien telescope & MCP intensified CCD
Aperture	coded mask, random pattern, 50% open		30 cm
Detector format	256 modules, 128 elements/module	600 × 600 pixels	256 × 256 pixels[a]
Energy range	15–150 keV	0.2–10 keV	170–650 nm
Energy resolution	∼7 keV	∼150 eV (at 5.9 keV)	$R \sim 150$
Sensitivity	$\sim 10^{-8}$ erg cm^{-2} sec^{-1}	2×10^{-14} erg cm^{-2} sec^{-1} in 10^4 sec	$m_{\rm B} = 22.3$ (in 10^4 sec)[b]
FoV[c]	1.4 sr	$23'.6 \times 23'.6$	$17' \times 17'$
PSF	$17''$	$18''$ HPD at 1.5 keV	$0.9''$ FWHM at 350 nm
Position accuracy	$\lesssim 4'$	$3''$	$\sim 0.5''$
Effective area	5240 cm^2	∼125 cm^2 at 1.5 keV	–[c]
Time resolution	100μsec	0.14 msec, 1.8 msec, or 2.5 sec[d]	11 msec

Table 2.3: Characteristics of the *Swift* instruments.

[a] Each pixel is divided to 8 × 8 virtual pixels in the onboard processor. Thus, 2048 × 2048 virtual pixels are provided in total.

[b] With the white filter.

[c] The effective area depends on filters. See Breeveld et al. (2011) for details.

[d] In the PD, WD, PC modes, respectively.

The flexibility of *Swift* provides opportunities for quick follow-up observations of not only GRBs but also transient events of BHXBs and neutron star binaries, magnetars, nova, X-ray flares from active stars, and so forth. A *Swift*/*MAXI* collaboration program has been working for several years to localize new Galactic X-ray transients detected by *MAXI* (Kennea et al., 2011a). *Swift* is the best observatory for performing the follow-up observations of new *MAXI* sources, because the XRT has a field of view comparable to the typical position accuracy of the *MAXI*/GSC. Moreover, combining the UVOT and XRT data, *Swift* is capable of determining the source positions with sufficient precision to perform further observations by ground-based optical and infrared telescopes. This collaboration program has been proven to be very powerful, and successfully localized more than ten *MAXI* transients so far (e.g., Kennea et al., 2011b; Morihana et al., 2013; Morii et al., 2013), including the black hole candidate MAXI J1305$-$704, which is studied in Section 4 of this thesis. In addition, the wide spatial coverage of the BAT allows long-term monitoring of known X-ray sources[1]. The BAT energy coverage (15–150 keV) is complementary to the *MAXI*/GSC, giving information in the softer X-ray bands within 2–30 keV.

---

[1] The BAT daily and orbital light curves of hundreds of X-ray sources are distributed publicly at http://swift.gsfc.nasa.gov/results/transients/.

3

Inner Disk Structure of H 1743−322 in the Low/hard State

H 1743−322 is one of the well-known black hole binaries. After the discovery in 1977 (Kaluzienski & Holt, 1977), it has displayed more than 10 outbursts thus far. The recent outbursts occurred recurrently with a relatively short interval (≈200 days; e.g., Shidatsu et al., 2012) among Galactic BHBs, and thus this source provides the best opportunity to observe the source in bright X-ray phases with high mass accretion rates. To study the inner disk structure, we conducted *Suzaku* observations of H 1743−322 in the low/hard state in 2012, when the source became bright and active. Quasi-simultaneous observations in the near-infrared (J, H, and K_{S}) and optical (R and i) bands were also carried out with the *Infrared Survey Facility* (*IRSF*) 1.4m telescope and the *Kanata* 1.5m telescope at Higashi-Hiroshima Observatory, respectively. The source was not detected in any bands, however.

This chapter is arranged as follows. Section 3.1 presents a brief observational history of this system. In Section 3.2, we explain the detail of the *Suzaku* observations and the data reduction. Section 3.3 shows the *Suzaku* light curves and power spectra, and Section 3.4 describes the spectral analysis and the results. In Section 3.5, we summarize the optical and near-infrared observations and the results. We discuss the *Suzaku* results in Section 3.6. Throughout the chapter, the distance and inclination of H 1743−322 are assumed as those determined by Steiner et al. (2012): $D = 8.5$ kpc and $i = 75°$, respectively.

3.1 Previous Observations of H 1743−322

H 1743−322 is discovered by *Ariel-V* in 1977 (Kaluzienski & Holt, 1977). The source position was determined more precisely by *HEAO-1* in the same year (Doxsey et al., 1977). Since then, it has exhibited more than 10 outbursts, which were extensively observed by X-ray satellites, such as *EXOSAT*, *RXTE*, *Chandra*, *INTEGRAL*, *Swift* and *Suzaku* (e.g., Cooke et al. 1984; Parmer et al. 2003; Capitanio et al. 2005; Miller et al. 2006c; Prat et al. 2009; Blum et al. 2010). Some of them were "failed" outbursts, which do not show a complete transition to the high/soft state (e.g., Capitanio et al., 2009; Chen et al., 2010). High- and low-frequency QPOs were detected above 100 Hz and below 10 Hz in some of the observations (e.g., Homan et al., 2003, 2005; Tomsick & Kalemci, 2003). X-ray energy spectra of H 1743−322 were also obtained many times during outbursts, including wide-band data up to ∼100 keV taken with *INTEGRAL* and *Suzaku* (Capitanio et al. 2005; Blum et al. 2010). However, the heavy interstellar absorption and effects of dust scattering (see Section 3.4.1) has made it difficult to obtain soft X-ray data below a few keV with sufficient quality (especially in the low/hard state) and to investigate the detailed structure of the inner accretion region. Ionized absorption lines, likely originating from disk winds, were discovered in the high/soft state and the very high state with *Chandra* high-resolution grating spectrometer (Miller et al., 2006c). This suggests that the source has a high inclination angle.

H 1743−322 was also observed in other wavelengths. Optical and near-infrared counterparts were identified by Steeghs et al. (2003) and Baba et al. (2003), respectively. However, the high Galactic extinction has hampered deeper monitoring observations to dynamically measure the black hole mass. Bright radio flares likely associated with relativistic jets were detected in the early phase of the outbursts (e.g., Rupen et al., 2003). In the 2003 outburst, bipolar large-scale X-ray jets were resolved with *Chandra* (Corbel et al., 2005). Combining the *Chandra* image with the radio data obtained with the Very Large Array (VLA) during the same outburst, Steiner et al. (2012) estimated the distance, the inclination angle, and the spin parameter a of the black hole ($a = cJ/GM_{\mathrm{BH}}^2$, where J represents the angular momentum) as 8.5 ± 0.8 kpc, 75° ± 3°, and 0.2 ± 0.3, respectively. They were derived by modeling the trajectories of the bipolar jets with a symmetric kinematic model.

3.2 *Suzaku* Observations and Data Reduction

On 2012 September 24, a brightening of H 1743−322 was reported by Shidatsu et al. (2012) with *MAXI*. About 2 weeks later, we triggered three sequential Target-of-Opportunity (ToO) observations with *Suzaku* (Mitsuda et al., 2007), when the X-ray flux reached the peak (the first observation on October 4; hereafter "Epoch-1") and started decreasing (the following two observations on October 10 and 12; hereafter "Epoch-2" and "Epoch-3", respectively). In all the epochs, the 1/4 window mode and the 1.0 sec burst option were employed for both FI- and BI-XISs to avoid pile-up effects. A summary of the *Suzaku* observations is presented in Table 3.1.

Figure 3.1 plots the long-term X-ray light curves of *MAXI*/GSC and *Swift*/BAT and their hardness ratio, in which the *Suzaku* epochs are marked with shaded regions. Epoch-1 is close to the peak of the BAT hard X-ray flux in the 15–50 keV band and Epoch-2 and -3 are located in the decaying phase, where the fluxes are lower than that of Epoch-1 by ≈20%.

	Epoch-1	**Epoch-2**	**Epoch-3**
ObsID	407005010	407005020	407005030
Start time (UT)	2012 Oct. 4 18:46:29	2012 Oct. 10 15:30:34	2012 Oct. 12 09:43:11
End time (UT)	2012 Oct. 5 14:35:16	2012 Oct. 11 14:04:14	2012 Oct. 13. 08:59:13
XIS window	1/4	1/4	1/4
Burst option	1.0 sec	1.0 sec	1.0 sec
Net exposure			
XIS	21 ksec	21 ksec	21 ksec
HXD	42 ksec	42 ksec	43 ksec

Table 3.1: Log of the *Suzaku* observation

The reduction and analysis of the *Suzaku* data were carried out by utilizing HEASOFT version 6.13 and *Suzaku* Calibration Database (CALDB) released on 2013 March 5. We started with the "cleaned" events (process version 2.8.16.34) provided by the *Suzaku* team and followed the standard procedure of the data reduction[1]. Source pho-

---

[1] The Suzaku Data Reduction Guide: http://heasarc.gsfc.nasa.gov/docs/suzaku/analysis/abc/

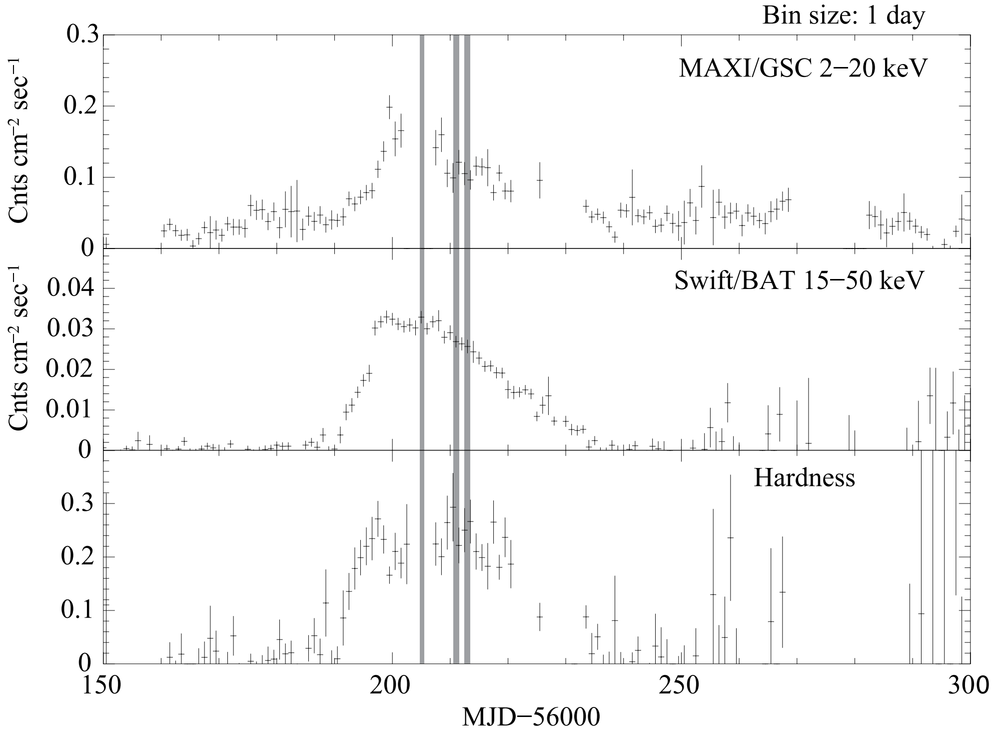

Figure 3.1: Long-term light curves of H 1743−322 in the 2–20 keV band obtained with *MAXI*/GSC (top) and in the 15–50 keV band from *Swift*/BAT (middle), and the hardness ratio calculated from these two light curves (bottom). The shaded regions indicate the *Suzaku* observations. MJD 56201 corresponds to 2012 October 1.

tons were extracted from a circular region with a radius of 110" centering at the target position. Background events were collected within a circle with a radius of 120" taken in a blank-sky area outside of the source region. The XIS response matrices and ancillary response files were generated by `xisrmfgen` and `xissimarfgen` (Ishisaki et al., 2007), respectively. The non X-ray background (NXB) was subtracted from the HXD data using the modeled NXB files produced by the HXD team[1]. As the response files of HXD, `ae_hxd_pinxinome11_20110601.rsp` was used for PIN, and `ae_hxd_gsoxinom_20100524.rsp` and `ae_hxd_gsoxinom_crab_20100526.arf` were used for GSO.

Because H 1743−322 is located in a crowded region close to the Galaxy center ($l, b = 357^\circ.26, -1^\circ.83$), the HXD spectra could be contaminated with the Galactic diffuse X-ray background (GXB) and nearby bright point sources[2]. However, we found that the GXB contributes only ≈1.5% of the total flux in the PIN bandpass, and far less than that in the GSO bandpass, which are negligible. To estimate these values, we assumed the GXB spectrum at $(l, b) = (28^\circ.5, 0^\circ.2)$ shown in Kubota et al. (2010) and converted the fluxes in the PIN and GSO energy ranges to those at the position of H 1743−322 using the spatial profile of the GXB in the 16–70 keV band obtained with *INTEGRAL*/IBIS (Krivonos et al., 2007). The cosmic X-ray background (CXB) is not subtracted from the HXD data, because its contribution is even smaller than that of the GXB. We examined the contamination of nearby sources using the *Swift*/BAT 70 month catalog (Baumgartner et al., 2013), considering the detector's transmission functions (Takahashi et al., 2007). We also checked the variability of the sources through the *MAXI*/GSC and *Swift*/BAT public light curves. The nearby sources were found to contribute only $< 1\%$ and ≈1% of the observed PIN and GSO fluxes, respectively, both of which are ignorable.

3.3 Light Curves and Timing Properties

In Figure 3.2 we presents the *Suzaku* light curves of H 1743−322 in the three epochs, where the source sometimes exhibits significant drops of the soft X-ray flux. These

---

[1] http://www.astro.isas.ac.jp/suzaku/analysis/hxd/pinnxb/tuned/ for the PIN background, and http://www.astro.isas.ac.jp/suzaku/analysis/hxd/gsonxb/ for that of GSO.

[2] The GXB component has been already subtracted from the XIS data, since the total background (CXB+NXB+GXB) contribution was estimated from the nearby off-source area in the XIS image.

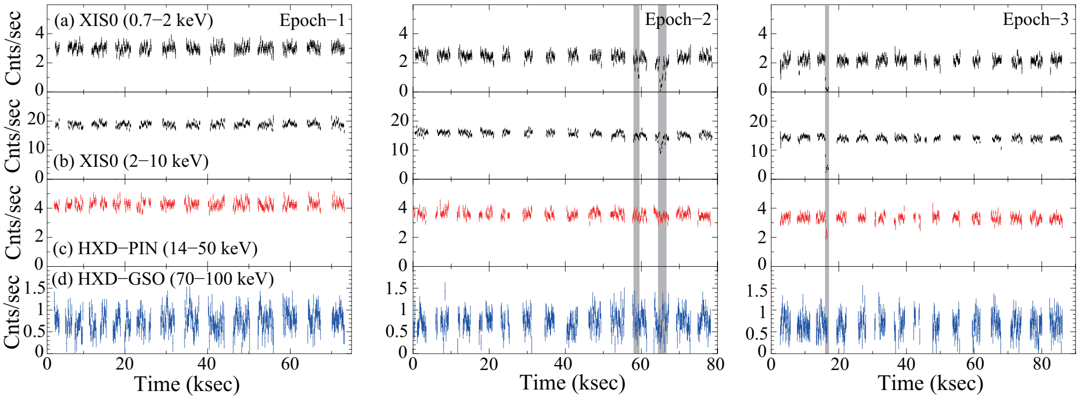

Figure 3.2: *Suzaku* XIS and HXD light curves of Epoch-1 (left), Epoch-2 (middle), and Epoch-3 (right). The shaded regions are dipping periods.

are called "absorption dips", which are thought to be caused by the obscuration of the central X-ray source by the outer edge of the accretion disk hit by the accretion stream from the companion star. As noticed in Figure 3.3, the hardness ratio increases in these dipping periods. This indicates that the dips are caused by photo-electric absorption, although the dipping durations are too short to precise time-resolved spectral analysis of the dips. The presence of similar absorption dips in H 1743−322 was previously reported (e.g., Homan et al., 2005). We define the shaded regions in Fig. 3.2 as the dipping periods, in which the count rate in the 0.7–2 keV band is $\gtrsim$30% smaller than the averaged rate in the individual epochs, and exclude them in the following analysis.

Figure 3.4 plots the normalized PDSs in the three epochs obtained from the PIN data. The PDSs are dominated by a strong noise components with a normalized power of $\approx 10^{-2}$ (rms/mean)^2 in the νP_ν form, consistent with those of typical BHBs in the low/hard state (see e.g., McClintock & Remillard, 2006). A weak, low frequency QPO is also detected in each epoch. Fitting it with a Gaussian model, we estimate the central frequency of the QPO as 0.206 ± 0.003 Hz in Epoch-1, which become 1.4 times lower in Epoch-2 and Epoch-3 (0.147 ± 0.004 Hz and 0.141 ± 0.004 Hz, respectively) as the *Swift*/BAT flux is decreased by $\approx$ 20%. This QPO is detected below 10 keV in the XIS PDSs as well.

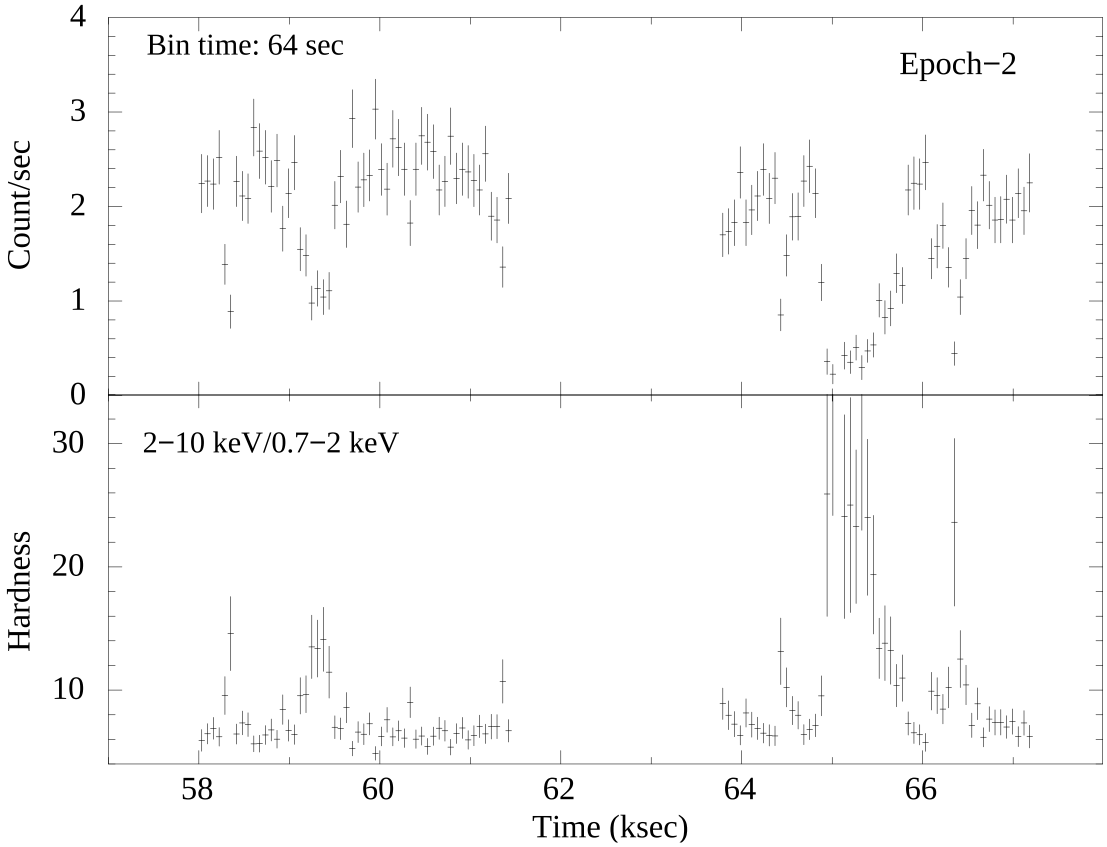

Figure 3.3: *Suzaku* light curve and hardness ratio in Epoch-2 focused on the dipping periods. Top: the XIS-0 light curve in the 0.7–2 keV band with a binning of 64 sec. Bottom: the hardness ratio between the 2–10 keV and 0.7–2 keV bands. Similar hardening can also be seen in the dipping period of Epoch-3 (see Fig. 3.2).

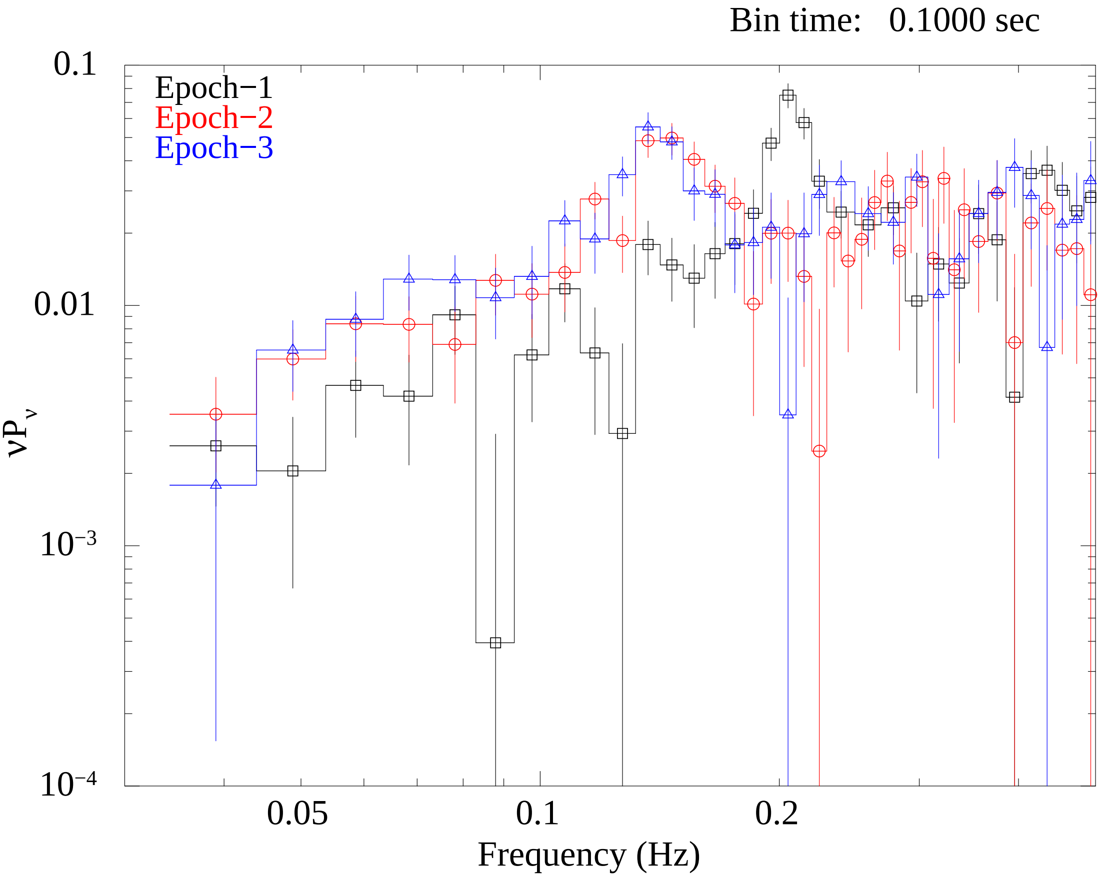

Figure 3.4: Normalized PDSs in the individual epochs created from the PIN light curves with 0.1 sec bins. They are normalized in such a way that their integral gives the squared root mean squared fractional variability. White noise is subtracted from all PDSs.

3.4 Spectral Analysis

We create the time-averaged spectra of the three epochs and analyze them separately on XSPEC version 12.8.0. Considering the signal-to-noise ratio and the reliability of the calibration, we use the data within 1–9 keV, 1–8 keV, and 14–70 keV for FI-XISs, BI-XIS, and PIN, respectively. For the GSO data, we only consider the 50–130 keV (Epoch-1), 50–220 keV (Epoch-2), and 50–200 keV (Epoch-3) bands, above which the signal levels are overcome by the systematic errors ($\lesssim$1% of the total count rate; Fukazawa et al., 2009) in the simulated background. The spectra and responses of FI-XISs (i.e., XIS-0 and XIS-3) are combined to improve statistics. The XIS data of 1.7–1.9 keV are discarded to avoid the uncertainties in the responses at energies around the complex instrumental Si-K edge. Following Makishima et al. (2008), we add a 1% systematic error to every spectral bin in the XIS and HXD data, to account for possible calibration uncertainties. We find that the final best-fit parameters are the same within their 90% confidence ranges even if we assign 0%, 2%, and 3% systematic errors, and that the confidence ranges themselves are increased only by $\lessapprox$ 10% from the case of 0% systematic error to that of 3%. We confirm that the conclusions are not affected. The cross-normalization of the HXD with respect to FI-XISs was fixed at 1.16,[1] while that of BI-XIS is left free. We examine the pileup effects in the XIS data using the software `aepileupcheckup.py`, which estimates the pileup fraction at various radii from the center of the XIS point-spread function (PSF; Yamada et al., 2012). We find that the pileup fraction is negligibly small in all observations, less than 2% even at the cores of the PSFs. Figure 3.5 shows the time-averaged spectra for the three epochs in the νF_ν form.

3.4.1 Dust-scattering Effects

In observations of heavily absorbed sources (with $N_\mathrm{H} \gtrsim 10^{22}$ cm^{-2}), it must be borne in mind that dust scattering as well as photo-electric absorption can significantly affect the observed soft X-ray spectra (Ueda et al. 2010; Hori et al. 2014). Diffuse interstellar (and circumbinary) dust can scatter-out the X-ray photons from the line of sight and at the same time, scatter-in the photons emitted in different directions. Consequently, we see a “dust halo” around a point source. A dust halo was indeed resolved in GX

---

[1] http://www.astro.isas.ac.jp/suzaku/doc/suzakumemo/suzakumemo-2008-06.pdf

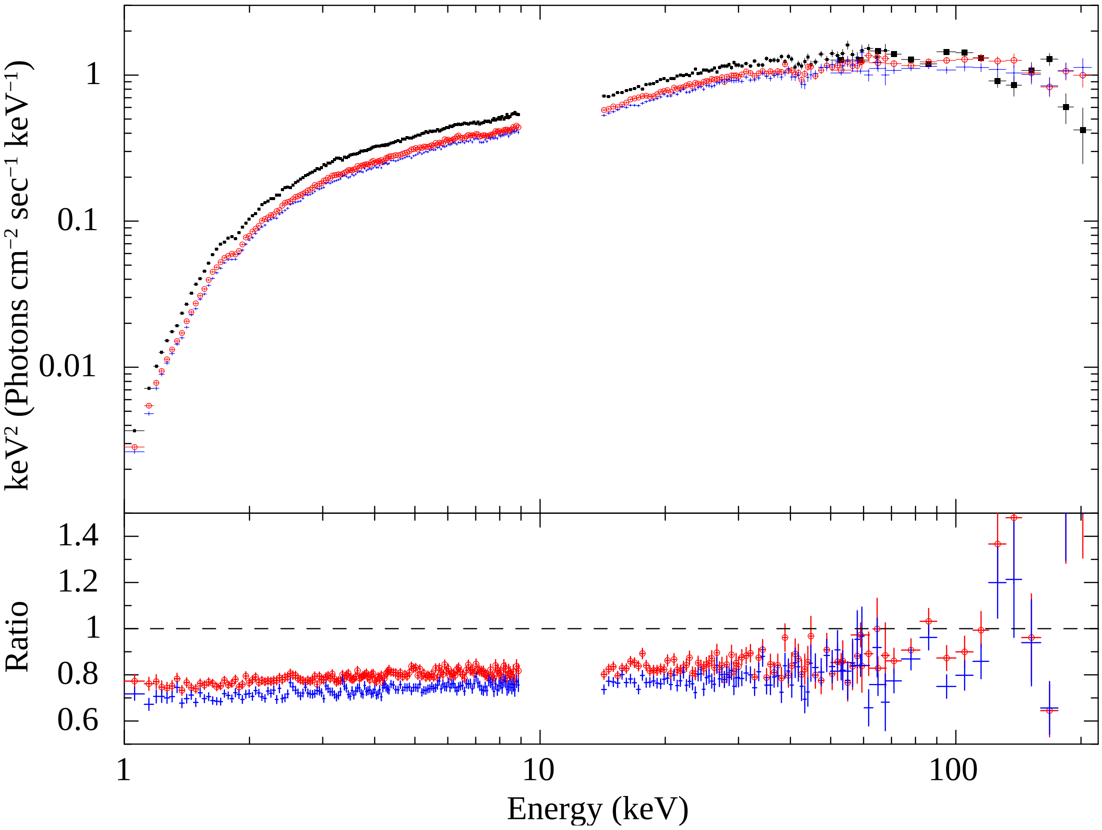

Figure 3.5: Time-averaged spectra in Epoch-1 (black, filled square), Epoch-2 (red, open circle), and Epoch-3 (blue, cross). The spectral ratios of Epoch-2 and Epoch-3 with respect to Epoch-1 are plotted in the lower panel.

13+1 (Smith et al., 2002), which has almost the same column density ($N_{\mathrm{H}} \approx 2 \times 10^{22}$ cm^{-2}) as our target. When we use data that do not fully cover the dust halo, those two scattering effects are not canceled out. In this case, the observed spectra, particularly in the soft X-ray band, are different from what we would expect if there were no dust-scattering. This must be taken into account for accurate spectral modeling. Even if all the scattered photons are collected, the scattered-in and scattered-out components no longer compensate each other in variable sources, due to the difference in arrival time between the scattered photons and those taking the straight path to the observer. In our case, the typical delay time of the scattered photons in the extraction region for the XIS is estimated to be ~1.3 days, by assuming a distance of 8.5 kpc. We confirm for all the *Suzaku* epochs that the flux variability of H 1743−322 on that timescale is low enough to ignore the variability of the scattered-in component.

Following Ueda et al. (2010) and Hori et al. (2014), we use the `Dscat` model to account for the effects of dust scattering in the spectral analysis. This is a local multiplicative model implemented in XSPEC, which estimates both scattering-in and -out components from the scattering fraction (the fraction of the scattered-in photons included in the data) and the hydrogen column density, by assuming the dust scattering cross section for $R_{\mathrm{V}} = 3.1$ calculated by Draine (2003). We fix the scattering fraction at 1.0 (i.e., all the scattered photons are included) for the HXD, which has a sufficiently large field of view to cover the whole dust halo. For the XIS, we adopt the same value (0.65) as Hori et al. (2014), because we used the same region as theirs to extract the source photons from the XIS data. In Hori et al. (2014), this value was estimated in the following manner. Utilizing `xissimarfgen`, they calculated the effective areas in the case of a point source and an extended source, which is assumed to have the same radial profile as that of the dust halo in GX 13+1 (Smith et al., 2002). The ratio of the latter to the former at 1 keV[1] was used as the scattering fraction for the XIS data.

In the following analysis, the column density of the `Dscat` model is always linked to that of the interstellar photo-electric absorption, for which we employ the `phabs` model (Balucinska-Church & McCammon, 1992). We find that ≈30%, ≈8%, and ≈3% of the intrinsic flux from H1743−322 are reduced at 1 keV, 3 keV, and 5 keV by the effects of dust scattering, respectively[2].

---

[1] The energy dependence of the ratio is ignorable.

[2] Here we assume $N_{\mathrm{H}} = 2 \times 10^{22}$ cm^{-2} as a typical column density of H 1743−322.

3.4.2 Modeling Time-averaged Spectra

As noticed in Fig. 3.5, the overall spectral shapes in the three epochs are very similar to one another, although the Epoch-2 and Epoch-3 spectra are slightly harder than that of Epoch-1. All of them are roughly characterized by a hard power-law component with a photon index of ≈ 1.6, suggesting that the source is in the low/hard state during the *Suzaku* observations. The hydrogen column density is estimated to be $\approx 2.0 \times 10^{22}$ cm^{-2} for the photo-electric absorption in cold interstellar medium. This value is well within those obtained in previous studies of H 1743−322 (1.6–2.3 $\times 10^{22}$ cm^{-2}; e.g., Miller et al. 2006c; Capitanio et al. 2009). A high-energy rollover can be found in 50–100 keV, which is likely to correspond to the electron temperature of the thermal corona. No significant emission and absorption lines can be seen in the spectra.

We first fit the spectra with the `nthcomp` model (Zdziarski et al. 1996; Życki et al. 1999) with an interstellar absorption. The `nthcomp` model calculates a thermal Comptonization spectrum parameterized by a photon index, an electron temperature of the Comptonizing corona ($kT_{\rm e}$), and a seed-photon temperature. We could not constrain $kT_{\rm e}$ from a joint fit with the XIS and HXD spectra, due to much poorer statistics of the GSO data compared with those of the XIS that dominate the total χ^2 statistics. We therefore determine $kT_{\rm e}$ only from the GSO spectra,[1] and fix it at the best-fit value in fitting together with the XIS and PIN data. From the joint fit of the XIS+HXD spectra, we obtain χ^2/d.o.f. = 1690/1158 (Epoch-1), 1253/994 (Epoch-2), and 1237/904 (Epoch-3), which are far from acceptable. As can be seen in the middle panel in Fig. 3.6, significant residuals remain in the hard X-ray band above 10 keV. A convex-shaped structure can be found, which is likely originated from the reflection of Comptonized photons on the disk.

We next apply a more sophisticated model to the spectra, considering the general picture of the low/hard state. We use the `diskbb` model (Mitsuda et al., 1984) as the direct emission from the standard disk and the `nthcomp` model as the Comptonization. The seed photon of the `nthcomp` component is assumed to be the multi-color disk emission, and the seed temperature is tied to the inner disk temperature of the `diskbb` component. To account for the reflection component, the `ireflect` model

---

[1] Here the seed temperature is fixed at 0.1 keV to constrain $kT_{\rm e}$ so that it does not affect the spectral shape in the GSO band.

(Magdziarz & Zdziarski, 1995) is convolved to `nthcomp`. This model calculates a reflection spectrum using the ionization parameter ($\xi = L_{\rm X}/(nR^2)$, where $L_{\rm X}$, n, and R are the incident X-ray luminosity, the electron number density and the distance of reflector from the X-ray source, respectively), the temperature ($T_{\rm disk}$), inclination angle (i), and solid angle ($\Omega/2\pi$) of the reflector. We fix $T_{\rm disk}$ at 30000 K, which cannot be constrained from the data. The `ireflect` model does not include any emission lines accompanied by the reflection continuum. We thus combine a Gaussian component to account for the iron K-α emission line, which is normally seen in the low/hard state spectra most significantly. Considering numerical studies (e.g., Matt et al., 1991), we link $\Omega/2\pi$ of `ireflect` and the normalization of the Gaussian to keep the equivalent width with respect to the reflection continuum at 1.0 keV. We note that the equivalent width becomes more than an order of magnitude smaller than what is expected in the numerical calculations, when we unlinked the normalization of the Gaussian and the solid angle of `ireflect`.

The convolution model `kdblur` (Laor, 1991) is also incorporated to model the relativistic blurring by the accretion disk around the black hole. This model uses the index α describing the radial dependence of the emissivity ϵ ($\propto r^{-\alpha}$), inner and outer radii of the accretion disk, and the inclination angle. Here we assume $\alpha = 3$ (i.e., a flat disk) and fix the inner radius at $10R_{\rm g}$ (where $R_{\rm g}$ is the gravitational radius, $GM_{\rm BH}/c^2$), and the outer radius at $R_{\rm out} = 400$, which is the maximum value of the `kdblur` model. The integrated fitting model is described as `phabs*Dscat*(diskbb+kdblur*(ireflect*nthcomp[ref]+gauss)+nthcomp[C])`, where `nthcomp[ref]` and `nthcomp[C]` represent the parts of the Comptonized component that is and is not reflected on the disk, respectively. Because `ireflect` and `kdblur` are convolution models, we extend the energy range to 0.01–1000 keV.

The quality of fit is remarkably improved compared with that of the single `nthcomp` model, yielding χ^2/d.o.f. = 1347/1155 (Epoch-1), 984/991 (Epoch-2), and 995/901 (Epoch-3). The spectra and the best-fit models in the individual epochs are plotted in Figure 3.6 and Figure 3.7, respectively. The resultant parameters are given in Table 3.2.

The inclusion of the relativistic blurring model to the reflection component makes a significant statistical improvement ($\Delta\chi^2 = 70$–90, where the degrees of freedom are not changed). When the `kdblur` component is excluded, we obtain χ^2/d.o.f. = 1435/1155, 1061/991, and 1075/901, for Epoch-1, -2, and -3, respectively. Conversely, the addition

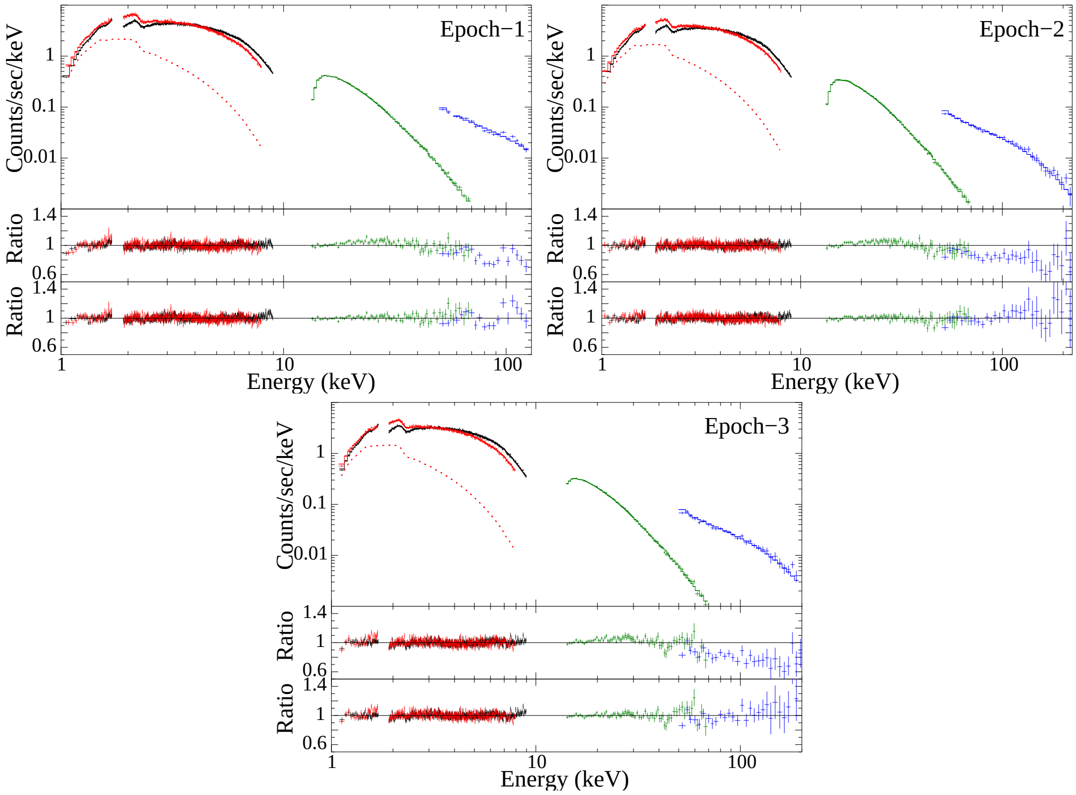

Figure 3.6: Time-averaged spectra of Epoch-1 (top), Epoch-2 (middle), and Epoch-3 (bottom) fitted with the `nthcomp` model. The black (below 9 keV), red (below 8 keV), green (14–70 keV), and blue (above 50 keV) points correspond to the XIS-0+XIS-3, XIS-1, PIN, and GSO data, respectively. The contribution of the scattered flux to the XIS-1 data is shown in red dotted line. The data/model ratio for a single `nthcomp` model and the final best-fit model are plotted in the second and third panels, respectively.

of a narrow Gaussian component at 6.4 keV with a 1-σ width of 10 eV does not improve the quality of fit.

Assuming an isotropic Comptonizated corona and the conservation of the total number of photons from the accretion disk, the inner disk radius can be derived from the formula in Kubota & Makishima (2004);

$$F^p_{\rm disk} + F^p_{\rm thc} 2\cos i = 0.0165 \left[\frac{r_{\rm in}^2 \cos i}{(D/10\ {\rm kpc})^2}\right] \left(\frac{T_{\rm in}}{1\ {\rm keV}}\right)^3 \ \ {\rm photons\ s^{-1}\ cm^{-2}}, \qquad (3.1)$$

where $F^p_{\rm disk}$ and $F^p_{\rm thc}$ are the 0.01–100 keV photon fluxes of the disk and thermal Comptonized components, respectively. Extending the best-fit model to that energy range,

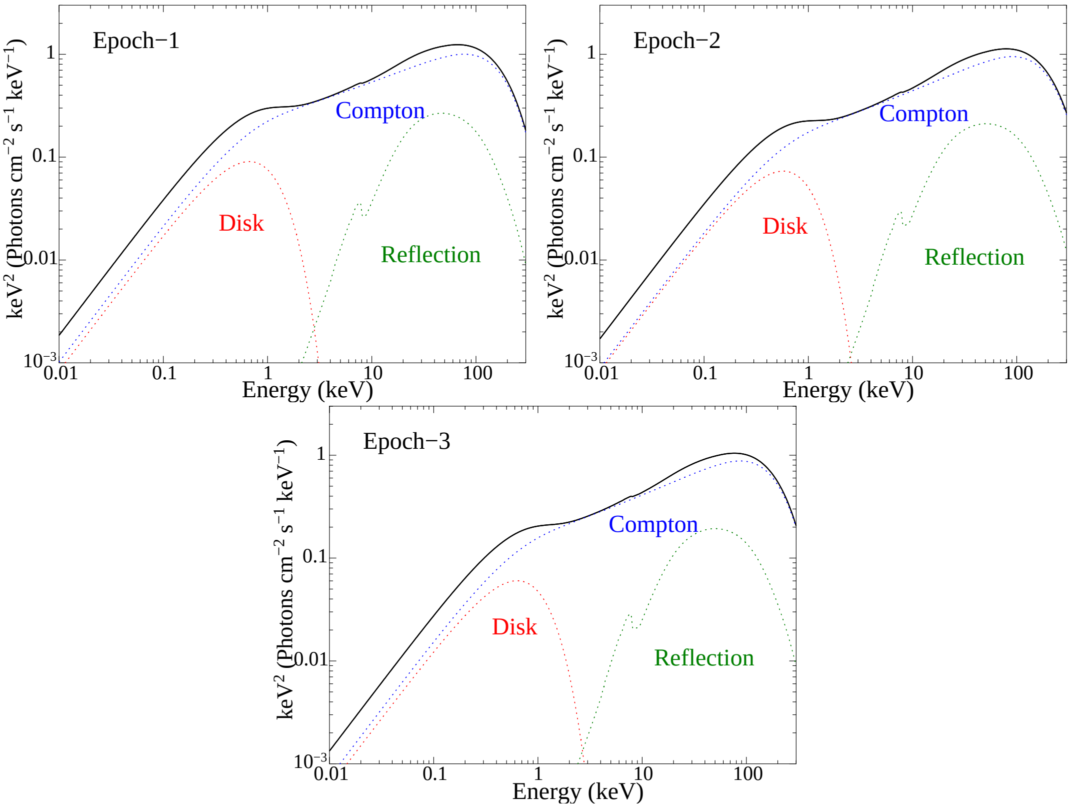

Figure 3.7: Best-fit models in Epoch-1 (top), Epoch-2 (middle), and Epoch-3 (bottom) plotted in the νF_ν form.

we estimate $F^p_{\rm disk} = 0.699$, 0.646, and 0.489 photons cm^{-2} sec^{-1} and $F^p_{\rm thc} = 1.27$, 1.06, and 0.918 photons cm^{-2} sec^{-1} in order from Epoch-1 to Epoch-3. The inner disk radii are thus $r_{\rm in} = 101^{+10}_{-9}\ D_{8.5}(\cos i/\cos 75°)^{-1/2}$ km, $r_{\rm in} = 119^{+24}_{-15}\ D_{8.5}(\cos i/\cos 75°)^{-1/2}$ km, and $r_{\rm in} = 92^{+19}_{-10}\ D_{8.5}(\cos i/\cos 75°)^{-1/2}$ km (where $D_{8.5}$ represents the distance in units of 8.5 kpc). Here we only include the 90% confidence range of the inner disk temperature to estimate the uncertainties of the radii. Multiplying a representative correction factor (1.19) of boundary condition and spectral hardening (Kubota et al., 1998), the actual radii are calculated to be $R_{\rm in} = 120^{+12}_{-11}\ D_{8.5}(\cos i/\cos 75°)^{-1/2}$ km, $R_{\rm in} = 141^{+28}_{-17}\ D_{8.5}(\cos i/\cos 75°)^{-1/2}$ km, and $R_{\rm in} = 110^{+23}_{-12}\ D_{8.5}(\cos i/\cos 75°)^{-1/2}$ km for Epoch-1, -2, and -3, respectively.

The inner radius in the high/soft state is $R_{\rm in} = 64 \pm 2\ D_{8.5}(\cos i/\cos 75°)^{-1/2}$ km (Chen et al., 2010), which is estimated from the direct disk emission without Comp-

Component	**Parameter**	**Epoch-1**	**Epoch-2**	**Epoch-3**
phabs	$N_{\rm H}$ (10^{22} cm^{-2})	$2.01^{+0.04}_{-0.06}$	1.99 ± 0.04	$1.99^{+0.05}_{-0.06}$
diskbb	$kT_{\rm in}$ (keV)	0.28 ± 0.02	$0.24^{+0.03}_{-0.02}$	$0.27^{+0.02}_{-0.03}$
	norm	$2.1^{+0.8}_{-1.0} \times 10^3$	$3.1^{+2.7}_{-1.3} \times 10^3$	$1.7^{+1.3}_{-0.8} \times 10^3$
nthcomp	Γ	$1.668^{+0.009}_{-0.005}$	$1.633^{+0.009}_{-0.008}$	1.629 ± 0.009
	$kT_{\rm e}$ (keV)$^{\rm a}$	< 35	68^{+68}_{-20}	61^{+144}_{-21}
	norm	$0.223^{+0.004}_{-0.006}$	0.174 ± 0.003	0.157 ± 0.004
ireflect	$\Omega/2\pi$	$0.65^{+0.08}_{-0.12}$	0.56 ± 0.07	$0.55^{+0.08}_{-0.07}$
	ξ (erg cm sec^{-1})	< 6	< 31	< 68
	$T_{\rm disk}$ (K)	30000 (fixed)	30000 (fixed)	30000 (fixed)
kdblur	$\alpha^{\rm b}$	3 (fixed)	3 (fixed)	3 (fixed)
	$R_{\rm in}$ ($R_{\rm g}$)	10 (fixed)	10 (fixed)	10 (fixed)
	$R_{\rm out}$ ($R_{\rm out}$)	400 (fixed)	400 (fixed)	400 (fixed)
	i (deg)	75 (fixed)	75 (fixed)	75 (fixed)
gauss$^{\rm c}$	$E_{\rm cen}$ (keV)	6.4 (fixed)	6.4 (fixed)	6.4 (fixed)
	σ (keV)	0.01 (fixed)	0.01 (fixed)	0.01 (fixed)
observed flux	1–10 keV (ergs cm^{-2} sec^{-1})	9.3×10^{-10}	7.5×10^{-10}	6.9×10^{-10}
unabsorbed flux$^{\rm d}$	0.01–100 keV (ergs cm^{-2} sec^{-1})	5.7×10^{-9}	4.8×10^{-9}	4.4×10^{-9}
	χ^2/d.o.f.	1347/1155	984/991	995/901

Table 3.2: Best-fit parameters of the `nthcomp` model

[a] The electron temperature is first estimated only from the GSO data and it is fixed at the best-fit value in the joint fit with the XIS and HXD spectra. Although the upper limit for Epoch-1 is not constrained, we adopted the best-estimate value, $kT_{\rm e} = 57$ keV, in the simultaneous fit.

[b] The emissivity index. The radial dependence of emissivity (ϵ) is expressed with $\epsilon \propto R^{-\alpha}$.

[c] The normalization of the Gaussian is linked to the solid angle of `ireflect` component so that the equivalent width with respect to the reflection continuum is always 1.0 keV.

[d] The flux is corrected for dust-scattering.

tonization. This value is taken from the first two rows of Table 2 in Chen et al. (2010) (which are originally from McClintock et al. 2009 and Capitanio et al. 2009). The fraction of the power-law component in the 2–20 keV flux is less than 6% for these two results and therefore $R_{\rm in}$ is changed by only a few % by including the Comptonized disk photons. The inner radii obtained from the *Suzaku* data are 1.3–2.3 times larger than the value in the high/soft state, suggesting that the standard disk do not extend to the ISCO during the low/hard state observations.

It has been suggested that the Comptonization cloud in the low/hard state has a complex structure. Using *Suzaku* broad-band X-ray data, Takahashi et al. (2008), Makishima et al. (2008), Shidatsu et al. (2011b), and Yamada et al. (2013a) found that the time-averaged spectra can be described with two Comptonization components that have different optical depths. Moreover, Yamada et al. (2013a) detected the second Comptonization component by analyzing the spectral variability. To test the "double Compton" model in the H 1743−322 data, we add one more `nthcomp` component and its accompanying reflection component to our final model, and fit the time-averaged spectra. We find, however, that the inclusion of the second Comptonization component does not improve the quality of fit.

3.4.3 Analysis of Short-term Spectral Variability

We often find it difficult to accurately estimate the cool disk component in the low/hard state by modeling time-averaged spectra, because it is buried in the dominant Comptonized component and coupled with the other structures such as the interstellar absorption and dust scattering. In these cases, the analysis of the short-term spectral variability can be a more powerful approach to separate the disk component. The standard disk and Comptonization in the corona have different properties of spectral variability on the ∼1-sec timescale; the former generally shows significant variation, while the latter is more stable (e.g., Churazov et al., 2001).

Here we apply "intensity-sorted spectroscopy" described in Makishima et al. (2008) and Yamada et al. (2013a) to our *Suzaku* data. Using this technique, Yamada et al. (2013a) successfully separated the cool disk component from the highly variable Comptonization in Cyg X-1. We define the high- and low-intensity phases in the same manner as theirs;

$$\{t|C(t) > (1+f)\overline{C(t)_T}\} \tag{3.2}$$

and

$$\{t|C(t) < (1-f)\overline{C(t)_T}\}, \tag{3.3}$$

respectively, where $C(t)$ is the count rate at the time t for an XIS detector and $\overline{C(t)_T}$ is that averaged over $[t - T/2, t + T/2)$. According to these criteria, we define the time intervals of high- and low-intensity phases using XIS-1 light curves in the 1–10 keV band in 2.0 sec binning. We set $f = 0.2$ and $T = 64$ sec, so that we obtain both the good photon statistics and a sufficiently high contrast of the intensity between the two phases. The XIS-0+XIS-3, PIN, and GSO spectra in these two phases are then extracted from the intervals determined by XIS-1. Thus, by using the independent dataset for the definition of the time regions, we avoid selection biases merely caused by statistical fluctuation in the photon counts in making the intensity-sorted spectra. A summary of the intensity selection is given in Table 3.3, and the XIS-1 light curves in low- and high-intensity phases are presented in Figure 3.8.

The high- and low-intensity spectra ($H(E)$ and $L(E)$, respectively) can be separated to the constant component ($d(E)$) and variable components ($h(E)$ and $l(E)$) as

$$H(E) = \omega(E)(d(E) + h(E)) \tag{3.4}$$

and

$$L(E) = \omega(E)(d(E) + l(E)), \tag{3.5}$$

where $\omega(E)$ represents the photo-electric absorption (which can be regarded as constant on the ∼1-sec timescale). Unlike Yamada et al. (2013a), the constant component $d(E)$ in our data contains not only the direct disk emission but also the scattered-in component, whose short-term variability is smoothed out due to the difference of the light traveling time of each scattered photon. On the other hand, the observed variable component is composed of the Comptonized photons without experiencing dust-scattering. For simplicity, we assume the best-fit models obtained from the time-averaged spectra as the scattered-in disk and Comptonization components, and subtract them from both the high- and low-intensity spectra before calculating the spectral ratio $H(E)/L(E)$.

Figure 3.9 plots the resultant spectral ratio in each epoch. The overall shape is very similar to that of the Cyg X-1 spectra in the low/hard state obtained in Yamada et al. (2013a). A turnover below ~ 2 keV can be seen, suggesting a significant suppression of variability due to the contribution of constant disk component at low energies. The spectral ratios of XIS-0+XIS-3 without removing the scattered-in component are also presented in pink for comparison. These demonstrate how significantly dust scattering affect the results. We note that the turnover is intrinsic, not generated by the dust scattering. The scattered-in component does not have such a steep turnover, and the decline of variability is seen in the spectral ratio including the scattered-in component as well.

Following the procedure of Yamada et al. (2013a), we assume that the ratio $H(E)/L(E)$ can be expressed with a single power-law (αE^{β}) in $E > 2$ keV. We determine α and β by fitting the data in the 2–4 keV band (above which they may affected by the reflection component). Using these parameters and Equation 3.4 and 3.5, we derive

$$\omega(E)d(E) = \frac{\alpha E^{\beta} L(E) - H(E)}{\alpha E^{\beta} - 1}, \tag{3.6}$$

where $d(E)$ is the direct disk spectra. $d(E)$ is then fitted with `phabs*Dscat*diskbb` to estimate the inner temperature and the flux of the constant disk emission. Here the scattering fraction of the `Dscat` model is fixed at 0.0 (i.e., only the effect of scattering-out is considered). We assume $N_{\rm H} = 2.0 \times 10^{22}$ cm^{-2}, which is the averaged value of those determined by the time-averaged spectra in the individual epochs. However, the parameters are only very weakly constrained due to the poor statistics in the soft X-ray band around the turnover of the spectral ratios, although the values are consistent with those estimated from the time-averaged spectra. The fitting parameters are summarized in Table 3.4.

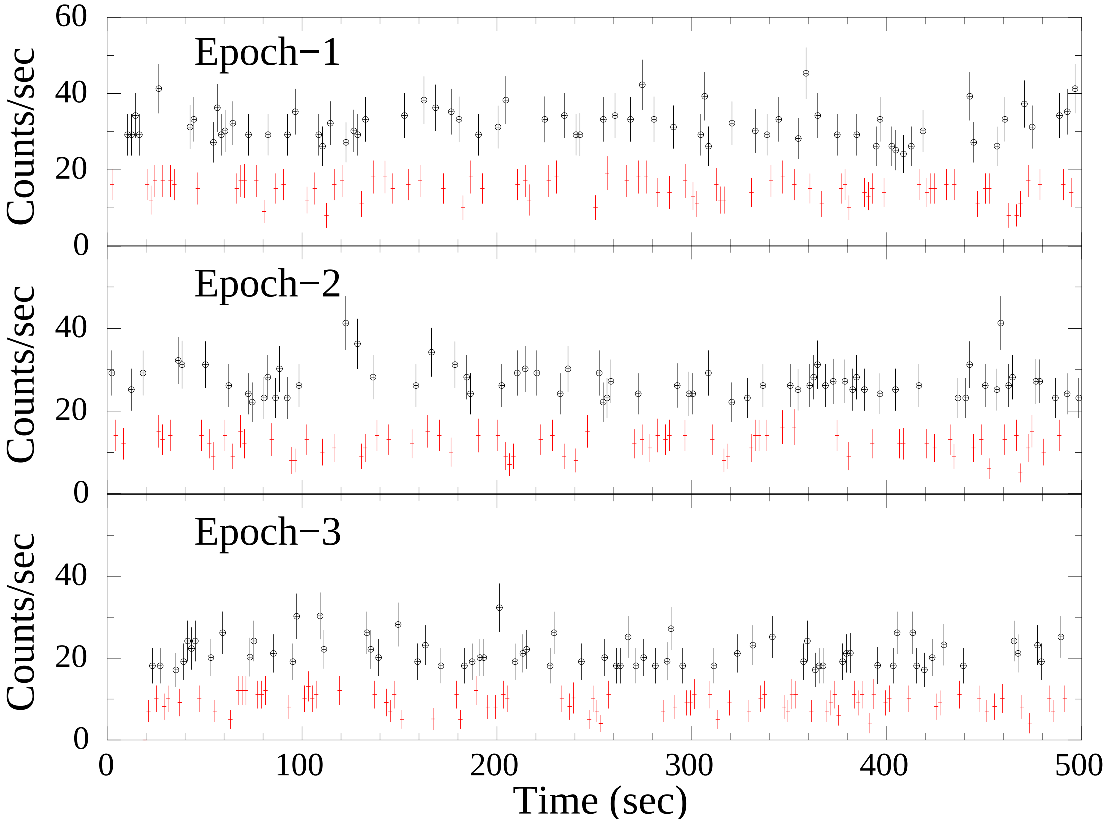

Figure 3.8: The XIS-1 light curves of Epoch-1 (top), Epoch-2 (middle), and Epoch-3 (bottom) in 1–10 keV for the high- (black) and low-intensity (dark gray) phases. The bin size is 2.0 sec.

	Epoch-1		Epoch-2		Epoch-3	
	High	**Low**	**High**	**Low**	**High**	**Low**
frac. exp. (%)[a]	24	27	24	28	25	29
ave. rate (cnt sec^{-1})[b]	27	18	22	15	20	14

Table 3.3: Summary of the high- and low-intensity selection.

[a] The fraction of time that the source was in high- and low-intensity phases with respect to the total exposure for each epoch.

[b] Averaged XIS-0 count rates in 1–10 keV.

Parameter	**Epoch-1**	**Epoch-2**	**Epoch-3**
$\boldsymbol{h(E)/l(E)}$[a]			
α	2.1 ± 0.1	2.1 ± 0.2	2.0 ± 0.1
β	-0.24 ± 0.06	-0.23 ± 0.06	-0.19 ± 0.06
χ^2/d.o.f.	6.1/6	8.1/6	13.4/13
$\boldsymbol{\omega(E)d(E)}$[b]			
N_{H} (10^{22} cm^{-2})	2.0 (fixed)	2.0 (fixed)	2.0 (fixed)
scatf[c]	0.0 (fixed)	0.0 (fixed)	0.0 (fixed)
T_{in}	$0.22^{+0.40}_{-0.08}$	< 0.33	$0.11^{+0.19}_{-0.06}$
norm	$< 8 \times 10^5$	$> 2 \times 10^3$	$< 1 \times 10^{12}$
χ^2/d.o.f.	3.1/6	4.2/3	11.3/8

Table 3.4: Results from the analysis of intensity-sorted spectra.

[a] $h(E)/l(E)$ is fitted with αE^{β} in the 2–4 keV band.

[b] $\omega(E)d(E)$, calculated by using the best-fit values of α and β, is fitted with `phabs*Dscat*diskbb`.

[c] The scattering fraction in the `Dscat` model.

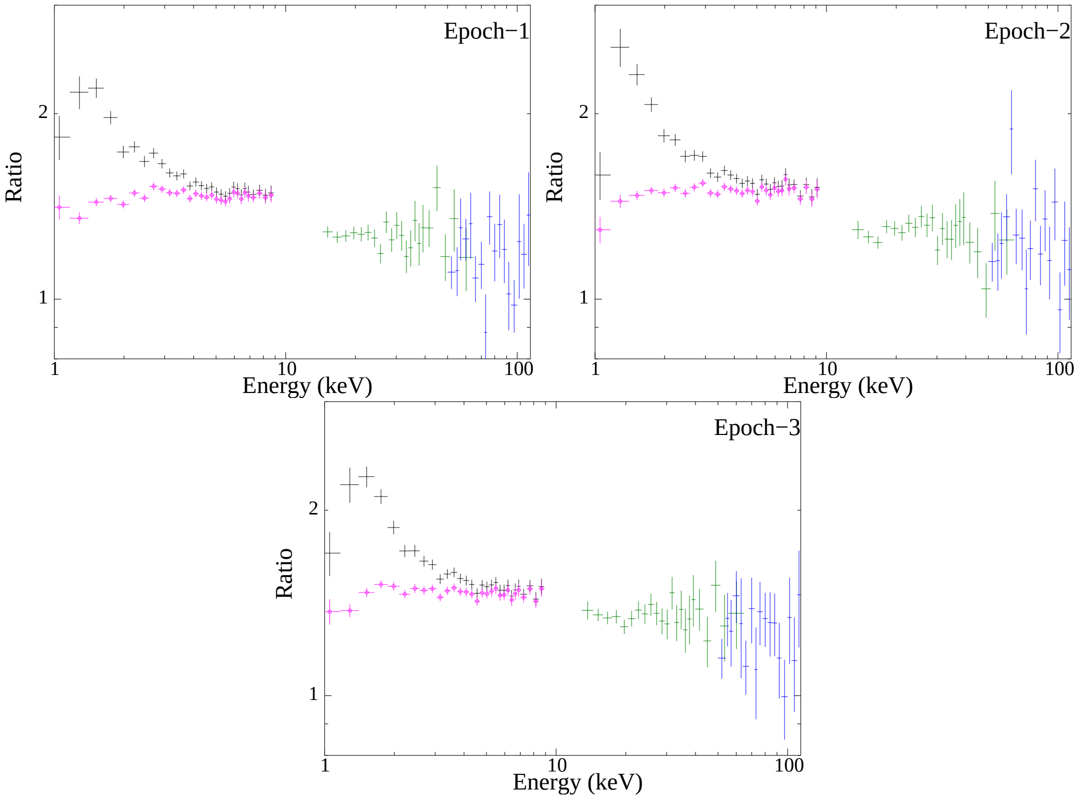

Figure 3.9: The ratios between the high-intensity and low-intensity spectra in Epoch-1 (top), Epoch-2 (middle), and Epoch-3 (bottom). The ordinate axis in each panel is logarithmically scaled. The scattered-in components are already subtracted from the XIS spectra. The same colors as Figure 3.6 are used. The XIS-1 data, which are used to determine the intervals of high- and low-intensity phases, are not shown here, because they are affected by Poisson fluctuation of signal counts. The XIS spectral ratio including the scattered-in component is also plotted in pink (open circle).

3.5 Near-infrared and Optical Observations and the Results

In addition to the X-ray observations with *Suzaku*, we performed infrared photometric observations of H 1743−322 in the J (1.25 μm), H (1.63 μm), and K_s (2.14 μm) bands, with the SIRIUS camera (Nagayama et al., 2003) on the 1.4m *IRSF* telescope at South African Astronomical Observatory during the 2012 outburst. Optical observations through R_C and I_C filters were also carried out by using Hiroshima One-shot Wide-field Polarimeter (HOWPol; Kawabata et al., 2008) attached to the 1.5m *Kanata* telescope at Higashi-Hiroshima Observatory. The counterpart of H 1743−322 was not detected in any bands, however. The typical seeing was ≈ 1".8 for the *IRSF* J band and 2".3 for the *Kanata* R_{C} band in full width at half maximum.

In the analysis of the *IRSF* data, we combine all the frames taken in one night and perform dark-subtraction, flat-fielding, sky-subtraction, and combining the dithered images using the SIRIUS pipeline software running on IRAF (Image Reduction and Analysis Facilities; Tody, 1986) version 2.16. H 1743−322 is located in a crowded region close to the Galactic center, and the near-infrared counterpart in the *IRSF* images is buried in nearby bright sources. We estimate the upper flux in each band from the counts on the pixel at the position of H 1743−322. Count-flux conversion is made by comparison with the stellar photometry of nearby sources with the 2MASS (Two Micron All Sky Survey) magnitude (Skrutskie et al., 2006). We reduce the *Kanata* data in a standard way for the aperture photometry of optical CCD data. The upper magnitudes in the R_{C} and I_{C} bands are determined by the detection limits of a point source in the image, estimated from the background level of source-free regions near H 1743−322.

Figure 3.10 presents the upper limits of the optical and near-infrared fluxes on 2012 October 12, together with the contemporaneous *Suzaku* spectrum (in Epoch-3). The flux limits in the optical and near-infrared bands are corrected for the Galactic extinction. Substituting the hydrogen column density of H 1743−322 ($N_{\mathrm{H}} \approx 2 \times 10^{22}$ cm^{-2}) into the N_{H} versus A_{V} relation (where A_{V} represents the extinction in the V band; Predehl & Schmitt, 1995), we derive $A_{\mathrm{V}} \approx 11$. We convert A_{V} to the extinction in the R_{C}, I_{C}, J, H, and K_{S} bands using the extinction curve for $R_{\mathrm{V}} = 3.1$ given by Cardelli et al. (1989). The upper limits of the extinction-corrected absolute R_{C}, I_{C}, J, H, and K_{S} magnitudes are estimated to be −1.9, −0.5, −3.8, −5.2, and −5.8, respectively. We find that if the companion is a main sequence star, it should be a late-B or a less massive star (Wainscoat et al., 1992).

The upper limits are consistent with the intrinsic disk flux including the Compton-scattered photons (shown in red in Fig. 3.10), and with the possible contribution of the synchrotron emission from the compact jet. If the positive relation between radio and X-ray fluxes found by Coriat et al. (2011) holds in the 2012 outburst, the *Suzaku* flux in Epoch-3 (5.2×10^{-10} erg cm^{-2} sec^{-1}in the 3–9 keV band) corresponds to 0.68 mJy at 8.5 GHz flux. Assuming that the flat optically-thick synchrotron spectrum extends up to the optical bands, we estimate the jet contribution to be $\nu F_\nu \approx 4 \times 10^{-12}$ erg cm^{-2} sec^{-1} at 5×10^{14} Hz. This is more than ≈10 times lower than the optical and near-infrared upper flux limits.

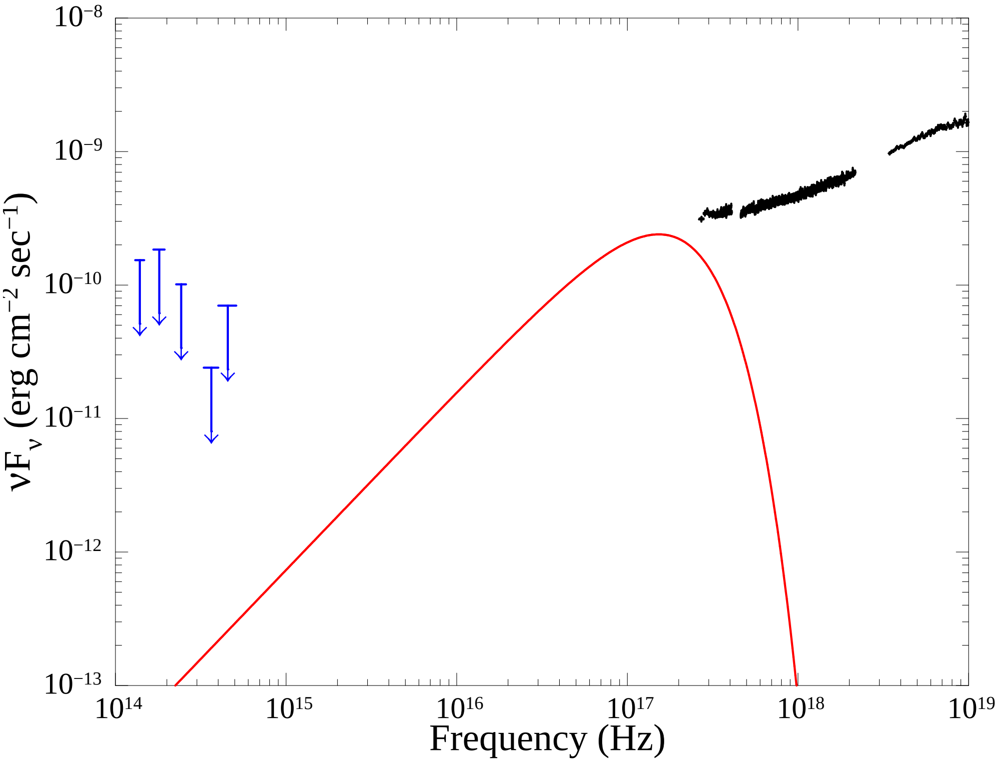

Figure 3.10: Spectral energy distribution of H 1743−322 on 2012 October 12. The upper limits in the extinction-corrected optical ($R_{\rm C}$ and $I_{\rm C}$) and near-infrared (J, H, and $K_{\rm S}$ bands) fluxes are plotted in blue arrows. The black points are the *Suzaku* spectra, corrected for neutral absorption and dust scattering. Red solid line shows the intrinsic disk emission including the Comptonized photons, where the outer disk is assumed to extend to infinity.

3.6 Summary and Discussion

3.6.1 Failed Outburst in 2012 October

We observed H 1743−322 with *Suzaku* at the flux peak and early decaying phase during the outburst in 2012 September and October. The time-averaged spectra in all the three epochs are approximated by a power-law with a photon index of ≈1.6, which is well within the typical values in the low/hard state (1.5–2.0; e.g., Done et al., 2007). The

PIN power spectra in the 14–70 keV band show strong variability above ≈0.1 Hz with a power of 1×10^{-2} (rms^2/Hz^2), which most likely corresponds to the flat part of the band-limited noise. These X-ray spectral and timing properties support that the source was in the low/hard state during the *Suzaku* observations.

As noted in Fig. 3.1, the long-term *MAXI* data do not show significant softening around the peak flux. This suggests that the state transition from the low/hard state to the high/soft state (hard-to-soft transition) did not occur in the late 2012 outburst. This type of outburst is often classified as a "failed outburst", which exhibits no hard-to-soft transition or an incomplete transition only reaching the intermediate state. A few failed outbursts have been reported in H 1743−322 so far (Capitanio et al., 2009; Chen et al., 2010). In addition to this source, there are few other BHBs that underwent failed outbursts, like XTE J1550−564 and MAXI J1836−164 (Sturner & Shrader 2005; Ferrigno et al. 2012). The 1–500 keV unabsorbed luminosity in Epoch-1 (calculated from the best-fit model) is estimated to be 6.1×10^{37} $D_{8.5}^2$ erg sec^{-1}. This is a few times lower than the luminosity at which H 1743−322 generally makes a hard-to-soft transition (e.g., McClintock et al., 2009; Zhou et al., 2013), suggesting that the mass accretion rate was not enough to trigger a transition.

3.6.2 Structure of Inner Disk and Corona

The time-averaged *Suzaku* spectra are well described with thermal emission from the standard disk, its Comptonized emission by a hot corona, and the reflection component from the accretion disk. The overall spectral shape is not largely changed in the three epochs, while the 2–20 keV fluxes in Epoch-2 and Epoch-3 are ≈20% lower than that in Epoch-1. Although the inner disk temperature and the photon index of the Comptonization decrease by 10%–30% and 0.03 from Epoch-1 to the latter two epochs, the other parameters remain the same within their 90% confidence ranges. We find that the double Comptonization model is not necessary to reproduce the spectra. The same was suggested with the *Suzaku* spectrum of MAXI J1305−704 in the low/hard state at $\sim 0.01 L_{\rm Edd}$ (Shidatsu et al., 2013). In the case of Cyg X-1, the softer Comptonization component is more clearly seen in the brighter low/hard (or hard intermediate) states (Yamada et al., 2013a). Thus, the luminosities of H 1743−322 in the *Suzaku* observations ($\approx 0.04\ D_{8.5}^2 M_{10}^{-1}\ L_{\rm Edd}$ in the 1–500 keV band) may not be sufficiently high to detect the softer Comptonization component significantly.

As noted in Fig. 3.5, the GSO spectra suggest the evidence of the high-energy rollover around 50–100 keV, likely correspond to the electron temperature of the Comptonized corona. From the spectral fit with the GSO data, the electron temperature is estimated to be $kT_\mathrm{e} \approx 60$ keV. We note, however, that the value may be somewhat overestimated because the `nthcomp` model does not include relativistic effects properly; its output spectrum drops more sharply above the rollover than the that of the real Comptonization spectrum (see Done, 2010). Previous observations of H 1743−322 with *INTEGRAL* and *Suzaku* at similar luminosities reported the detection of the cutoff energy (e.g., Capitanio et al. 2005; Blum et al. 2010). The anti-correlation between the electron temperature and the X-ray luminosity in the bright ($\lesssim 0.1 L_\mathrm{Edd}$) low/hard state was suggested by Miyakawa et al. (2008) with the *Rossi X-ray Timing Explorer* (*RXTE*; Bradt et al., 1993) spectra of GX 339−4. Chiang et al. (2010) also found in the *RXTE* data of Swift J1753.5−0127 that the electron temperature is relatively low in the bright low/hard state like in our case, and that it moves to higher energies in accordance with the decline of an outburst. It would be explained if inverse Compton cooling in the corona is more efficient by a relatively higher input rate of seed photons in brighter periods (Miyakawa et al., 2008).

We find that the X-ray spectra are dominated by the Comptonized component and that the direct disk emission is very weak in the *Suzaku* bandpass. The disk temperature estimated from the time-averaged spectra is much smaller than typical values in the high/soft state (≈1 keV; e.g., McClintock & Remillard, 2006). We calculate the inner disk radius from the intrinsic disk flux including the disk photons consumed by Compton-scattering in the corona in each epoch. The radii are found to be 1.3–2.3 times larger than that in the high/soft state, supporting the idea that the standard disk does not extend to the ISCO in the low/hard state. This is consistent with the somewhat smaller solid angle of the reflection component than those obtained in the very high state by using similar spectral models (Tamura et al. 2012; Hori et al. 2014).

We note, however, the calculated inner radii should be taken with caution, since this is somewhat dependent on spectral modeling. We considered only the statistical uncertainties of the inner disk temperatures, but additional errors may be produced in modeling the effects of dust scattering. Also, the spectral hardening factor of disk emission for deriving the actual inner radii could be different between the high/soft and low/hard states (e.g., Shimura & Takahara, 1995). Moreover, we assumed that all the seed photons are originated from the disk, but if other emission components contribute, the inner radii could become smaller. For more precise estimation of the inner disk radii, we have to assess these possible uncertainties thoroughly by using higher-quality wide-band spectra, particularly from the sources with a much smaller absorption column. This is left for future work.

We successfully detect the weak, cool disk component independently of the time-averaged spectral modeling, using the spectral variability on a short (≈1 sec) timescale. The overall profile of spectral ratio between high- and low-intensity phases is very similar to what Yamada et al. (2013a) found in Cyg X-1 data during the low/hard state. The power of short-term variability clearly declines below 1–2 keV, suggesting that the constant standard disk component contributes to the soft X-ray flux. Modeling the profile of the spectral ratio in the same manner as Yamada et al. (2013a), we estimate the inner radius and temperature of the disk component. Although the resultant parameters have large uncertainties due to poor statistics, they are consistent with those obtained from the time-averaged spectra.

The mass accretion rate of the disk can be derived through $L_{\rm disk} = GM_{\rm BH}\dot{m}_{\rm disk}/(2R_{\rm in})$, where $L_{\rm disk}$ and $\dot{m}_{\rm disk}$ represent the luminosity and mass accretion rate of the disk component, respectively. We estimate $L_{\rm disk} = 2.5 \times 10^{36}\ D_{8.5}^2$ erg sec^{-1} (the unabsorbed disk luminosity in the 0.01–500 keV band) and $R_{\rm in} = 120\ D_{8.5}(\cos i/\cos 75°)^{-1/2}$ km (for Epoch-1) and thus we have $\dot{m}_{\rm disk} = 4.5 \times 10^{16}\ D_{8.5}^3\ M_{10}^{-1}(\cos i/\cos 75°)^{-1/2}$ g s^{-1}. The accretion rate of corona can be calculated as $L_{\rm c} = \eta\dot{m}_{\rm c}c^2$, where η, $L_{\rm c}$, and $\dot{m}_{\rm c}$ are the radiative efficiency, the luminosity and the mass accretion rate of the corona, respectively. Using the best-fit `nthcomp` component for Epoch-1 as $L_{\rm c}$ ($5.1 \times 10^{37}\ D_{8.5}^2$ erg sec^{-1}), we obtain $\dot{m}_{\rm c} = 5.7 \times 10^{17}\ D_{8.5}$ g s^{-1} if the corona is radiatively efficient ($\eta = 0.1$ is assumed). It can be much more larger in the case of a radiatively inefficient flow. Thus, $\dot{m}_{\rm c}$ is much larger than $\dot{m}_{\rm disk}$, regardless of the radiative efficiency. This is inconsistent with the simple truncation disk model, in which the standard disk makes transition at the truncated radius into the hot inner flow with the same mass accretion rate.

A possible explanation is that there may be a separate coronal accretion flow with a large scale height extending from the outer edge of the disk to the black hole, and that its mass accretion rate is much larger than that of the thin disk. There is another possibility, which reconciles the mass accretion rates of the disk and corona. If the soft

X-ray component is not the disk itself, but is instead originated from a much smaller, hot clumps torn off the inner edge of a much larger disk (Chiang et al., 2010; Yamada et al., 2013a), the true disk component has larger normalization but is truncated at a larger radius. In this case, $\dot{m}_{\rm disk}$ can be comparable to $\dot{m}_{\rm c}$, and the true inner disk temperature can be much lower, making impossible to detect the disk component in the soft X-ray bandpass. The cool disk component peaking in the EUV band was actually detected in a low/hard state spectrum of XTE J1118+480 (Esin et al., 2001), along with a much smaller soft X-ray component (Reis et al., 2009), which would be from the clumps (Chiang et al., 2010).

3.6.3 Ionized Absorber and Disk Wind

Miller et al. (2006c) discovered blue-shifted, ionized absorption lines at 6.7 keV and 7.0 keV (corresponding to He-like and H-like iron Kα lines, respectively) in the *Chandra* high-resolution spectra of H 1743−322 in the high/soft and very high (or soft intermediate) states. These lines, often seen in high inclination sources (e.g., Ueda et al. 1998; Kotani et al. 2000; Lee et al. 2002), likely originated from the disk wind. They show "state-dependent" behavior and are rarely detected in the low/hard state (e.g., Neilsen & Lee, 2009; Ponti et al., 2012). For H 1743−322, the non-detection of the iron absorption lines in the low/hard state was previously reported by Blum et al. (2010) and Miller et al. (2012a).

Our *Suzaku* data do not exhibit any significant absorption features apparently. To check the presence of the ionized iron absorption lines, we add two negative Gaussian components to the best-fit model for the time-averaged spectra. Here we assume a wind velocity of 300 km $\rm sec^{-1}$ and a 1-σ line width of 20 eV (which can be regarded as representative values of Miller et al. 2006c) and fix all the parameter except for the normalizations of continuum and line components. We estimate the 90% upper limits of the equivalent widths in Epoch-2 to be 22 eV for both H-like and He-like iron lines, which are similar or slightly larger values than those obtained in Miller et al. (2006c). Thus, we cannot exclude the presence or disappearance of the ionized iron absorption lines.

3.6.4 Origin of QPO

A weak LF QPO is detected at 0.1–0.2 Hz in each epoch. We find that the QPO frequency becomes ≈30% lower in accordance with the ≈20% decrease of the hard X-ray luminosity in the 15–50 keV band. LF QPOs (below 10 Hz) were detected in many BHBs during the low/hard and intermediate states, such as XTE J150−564 (e.g., Cui et al., 1999; Sobczak et al., 1999) and GX 339−4 (e.g., Miyamoto et al., 1991; Motta et al., 2011; Tamura et al., 2012). Previous studies suggested that their frequencies are positively correlated with the photon index of the Comptonization below ≈10 Hz, at which the correlation saturates (Vignarca et al. 2003; Titarchuk & Fiorito 2004; Titarchuk & Shaposhnikov 2005). Our results follow this ubiquitous correlation between the QPO frequency and the photon index; the photon index becomes by ≈0.03 lower in the ≈30% decrease of the QPO frequency.

The correlations of the observed LF-QPO frequencies with the X-ray flux and the photon index lead us to invoke the idea that they are associated with the inner disk structure. Ingram et al. (2009) suggested the possibility that the LF QPOs originated the Lense-Thirring precession of the hot inner flow extended between the black hole and the inner edge of the disk. Their model can describe both the QPO frequencies and the observed X-ray spectrum, and predicts the anti-correlation with the inner disk radius and the QPO frequency. In the truncation disk model, the inner radius recedes as the mass accretion rate is decreased (see Done et al., 2007). At the same time, the power of seed photons illuminating the hot flow becomes weaker, making the observed X-ray spectrum harder. The decrease of the LF-QPO frequency can be explained if it reflects the timescale at the inner radius, where the standard disk is replaced to the hot flow (Ingram et al., 2009). Axelsson et al. (2014) extracted the spectrum of the pure QPO component from the *RXTE* data of XTE J1550−564 and found that it can indeed be interpreted by the Comptonization in the hot inner flow. Although the inner disk radii that we estimated from the *Suzaku* data in each epoch have large uncertainties, they are compatible to the anti-correlation trend between the QPO frequency and the inner disk.

The QPO frequencies correspond to 40–50 $R_{\rm g}$ in the Lense-Thirring precession model of Ingram et al. (2009), if a black hole mass of $10 M_{\odot}$ is assumed. This is about several to 10 times larger than what we estimated from the time-averaged spectra. The possible reason of this inconsistency would be that the QPO was generated by a more complicated mechanism, or that we are underestimating the true inner disk radius, as is also suggested in Section 3.6.2 by assuming that the mass accretion rate through the disk and that in the coronal flow are the same. A separate, small variable soft component could simultaneously allow the QPO to be consistent with a Lense-Thirring origin, and for the corona to be fed directly by the mass accreting through the disk.

4

Accretion Disk and Ionized Absorber of MAXI J1305−704 in the Low/hard and High/soft States

MAXI J1305−704 is a black hole candidate discovered by *MAXI*/GSC in 2012 April (Sato et al., 2012). A few weeks after the discovery, follow-up observations with *Swift* and *Chandra* detected ionized absorption lines likely produced by disk winds in the high/soft state. To study the detailed structure of the accretion flow and to investigate whether the ionized absorber is also present in a low mass accretion rate, we requested a TOO observation to the *Suzaku* operation team in 2012 July when the source was in the low/hard state.

In this chapter, we present the results from the *Suzaku* observation of MAXI J1305−704. The data obtained from a *Swift*/XRT observation during the high/soft state are also analyzed to be compared with the *Suzaku* results. In addition, we report the near infrared observations with the 1.4 m telescope of *IRSF* performed almost simultaneously with the *Suzaku* observation and in an earlier epoch when MAXI J1305−704 was in the high/soft state. We first give a short history of the source in Section 4.1 and then explain the X-ray observations and the data reduction in Section 4.2. Section 4.3 describes the analyses and results of the X-ray data. Section 4.4 presents the infrared and optical observations and results. In Section 4.5, we summarize and discuss all the results.

4.1 Short History of MAXI J1305−704

MAXI J1305−704 was first detected on the *MAXI* nova atert system (Negoro et al., 2012) on 2012 April 9 (Sato et al., 2012) and precisely localized with *Swift*. The source position is determined as (RA, decl.) = ($13^{\mathrm{h}}06^{\mathrm{m}}53^{\mathrm{s}}.53$, $-70^{\circ}27'.01''.8$) with an 90% uncertainty of $2.0''$ radius (Kennea et al., 2012a). The monitoring results with the *MAXI*/GSC suggest that the source is likely a black hole X-ray binary, as its hardness-intensity diagram showed a q-shaped hysteresis over the whole outburst and the spectrum during the soft phase is well modeled with thermal emission from the standard disk like those of typical BHXBs in the high/soft state (Morihana et al., 2013). A lot of follow-up observations were triggered in X-ray and other wavelengths. Multiple *Swift* X-ray Telescope (XRT) observations discovered dips in the X-ray light curves, whose interval has been however still controversial; 1.5 hours and 2.7 hours were suggested by Kennea et al. (2012b) and Kuulkers et al. (2012). *Swift*/XRT also detected strong ionized absorption lines, likely originated in the disk wind (Miller et al., 2012b). The *Chandra* High Energy Transmission Gratings Spectrometer (HETGS) discovered complex absorption feature around 1 keV, which can be reproduced by ionized iron-L absorption lines (Miller et al., 2012c). Those dips and absorption profiles strongly indicate that the source has a large inclination angle, although the precise value is not determined yet. The optical and near infrared counterparts were also detected in the observations performed about a few days after the start of the outburst (Greiner et al., 2012).

4.2 X-ray Observation and Data Reduction

4.2.1 *Suzaku* Observation in the Low/hard State

We observed MAXI J1305−704 with *Suzaku* (Mitsuda et al., 2007) from 2012 July 20 18:10:29 (UT) to 22 00:30:23 for a net exposure of ≈40 ksec. This was carried out as a TOO observation based on the monitoring by *MAXI*/GSC. In this observation, the 1/4 window option was employed for the XIS. The actual observed count rate was ≈ 5 counts sec^{-1} on average, which is low enough that we can ignore any effects by pileup. The *Suzaku* observation (MJD 56128–55130) corresponds to the period after the spectral hardening at the end of the outburst in 2012 June (Morihana et al., 2013), suggesting that the source was in the low/hard state in our observation.

We utilized the cleaned event data produced by the pipeline processing version 2.7.16.33, and reduced them with HEASOFT version 6.12 and Calibration Database (CALDB) released on 2012 October 5. The source events of the XIS were extracted from a circular region centered on the source position with a radius of 1.9'. The background was taken from a circular region with the same radius in a source-free area. For the non X-ray background of the HXD, we used the modeled background files provided by the *Suzaku* team. The modeled spectrum of the cosmic X-ray background was subtracted from the PIN data, but not from the GSO data, because its contribution is less than 0.1% of the total background rate of the GSO[1]. The PIN and GSO data were corrected for dead time with `hxddtcor`. The XIS response matrix and ancillary response files were created with the `xisrmfgen` and `xissimarfgen`, respectively, to be used in our spectral analysis. We utilized `ae_hxd_pinxinome11_20110601.rsp` as the response file for PIN, and `ae_hxd_gsoxinom_20100524.rsp` and `ae_hxd_gsoxinom_crab_20100526.arf` [2] for GSO. We combined the spectra and response files of the FI-XISs (XIS-0 and XIS-3) to improve statistics. The data in the 1.7–1.9 keV band were always ignored in the spectral fits due to the systematic uncertainties in the instrumental Si-K edge. A 1% systematic error was included in each bin of the XIS and HXD spectra to account for possible calibration uncertainties.

The spectra of the FI-XISs, BI-XIS, and HXD were simultaneously fitted in the spectral analysis. The cross-normalization of the HXD with respect to the FI-XISs was fixed at 1.16[3]. We corrected for cross-calibration errors in the energy responses between the FI-XISs and BI-XIS, as we found that our FI-XIS data resulted in significantly harder spectra than the BI-XIS data from the individual spectral analysis, probably due to uncertainties in modeling the contamination on the XIS window filters. To examine trends of these uncertainties in the period near our observation, we analyzed two *Suzaku* archival data of the blazar PKS 2155−304 observed on 2012 April 27-29 and October 30-31, both of which were operated with the same (1/4) window option. We created

---

[1] http://www.astro.isas.ac.jp/suzaku/analysis/hxd/gsonxb/

[2] http://www.astro.isas.ac.jp/suzaku/analysis/hxd/gsoarf2/

[3] http://www.astro.isas.ac.jp/suzaku/doc/suzakumemo/suzakumemo-2008-06.pdf

time-averaged FI-XIS and BI-XIS spectra separately for the two epochs, using the same versions of HEASOFT and CALDB as those applied in the analysis of the MAXI J1305−704 data. The spectra were fitted with an absorbed power-law model, in which the photon indices were linked between the FI-XIS and BI-XIS data. We found that the FI-XIS spectra show larger N_{H} than the BI-XIS spectra by $\Delta N_{\mathrm{H}} = 1.2 \times 10^{20}$ cm^{-2} and $\Delta N_{\mathrm{H}} = 2.0 \times 10^{20}$ cm^{-2} in the April and October observations, respectively. Similarly, for the case of MAXI J1305–704, we estimated difference of $\Delta N_{\mathrm{H}} = 3 \times 10^{20}$ cm^{-2}. To account for this offset, we unlinked the column density of the neutral absorption along with the flux normalization between the FI-XIS and BI-XIS spectra in the simultaneous fit. In the following section we show the column density obtained from the BI-XIS spectrum as the best estimated value. The inclusion of this correction is found to significantly improve the quality of the fit, although it does not affect the conclusion of this chapter.

MAXI J1305−704 is located near a bright source 4U 1254−690 with a separation angle of $1^{\circ}.41$ and the GSO flux can be contaminated by the emission from this nearby source (Takahashi et al., 2007). However, we confirmed that the contamination is completely negligible as the source is more than several orders of magnitude fainter than our target above 50 keV by considering the previous spectral study of 4U 1254−690 (Díaz Trigo et al., 2009).

4.2.2 *Swift*/XRT Observations in the High/soft State

Since its discovery, MAXI J1305−704 was observed with *Swift*/XRT many times. In order to compare the *Suzaku* data in the low/hard state with *Swift* data in the high/soft state, we analyzed the data of *Swift*/XRT obtained from 2012 April 19 13:19:53 to 21 17:03:00 (UT). This is one of the longest (≈ 10 ksec) *Swift*/XRT observations for this source in the high/soft state. Using this dataset, Miller et al. (2012b) reported the existence of a strong iron-K absorption line around 6.6 keV. In this observation, XRT was operated with the 1-dimensional WT mode. The data are not affected by pile-up, because the averaged count rate (≈ 30 counts sec^{-1}) is much lower than the maximum pileup-free count rate (100 counts sec^{-1}; Romano et al., 2006).

We used *Swift*/XRT archival data and performed the standard reduction with `xrtpipeline`. The source events were extracted from a box region of 40 pixels × 30 pixels along with the X- and Y-axis in the detector coordinates, respectively, with the center located at the target position. The background region was defined as two boxes of 40 pixels × 30 pixels in the source-free area at the same distance from the target position. We included 3% systematic error in each spectral bin to absorb possible calibration uncertainty[1]. We utilized a response matrix file, `swxwt0to2s6_20010101v014.rmf`, taken from the *Swift* CALDB provided on 2012 October 5. The ancillary response file is created by using `xrtmkarf` with the exposure file produced with the pipeline tool.

4.3 Analysis and Results

4.3.1 *Suzaku* Light Curve and Dip Feature

Figure 4.1 shows the *Suzaku* XIS-3 light curves in the soft (0.7–2 keV) and hard (2–10 keV) bands together with their hardness ratio in 128 sec binning. The light curve is highly variable particularly in the soft band, suggesting that the variability is mainly caused by absorption. We can see two dipping features with different mean hardness ratios (≈5–10 for the softer ones and ≈20–30 for the harder ones), in which more than 80% of the averaged flux is lost in the soft band, and those dips with similar mean hardness ratios are observed almost periodically. Here we define the start and end times of the dips as the points at which the hardness ratio crosses a value to 2.6 upward and downward in Fig. 4.1. We then call the dips whose peak hardness ratios reach 20 in 128 sec binning as "deep dips" and the other softer ones as "shallow dips". In shorter time scales, the shallow dips have small variabilities with typical time scale of a few minutes, while this behavior is not significant in the deep dips (Figure 4.2).

1.0

We find each dip recurrently occurs with a period of 9.74 ± 0.04 hours, which is calculated from the intervals of the start times of deep dips obtained in the XIS-3 hardness ratio with 64 sec bin. The error is estimated by propagating the uncertainty of each measured start time, which is assumed as half width of time bins in the light curve (32 sec). This interval, instead of the 1.5 or 2.7 hours suggested by *Swift*/XRT observations with shorter exposure (Kennea et al., 2012b; Kuulkers et al., 2012), likely corresponds to the orbital period. The light curves have data gaps with durations of 0.8–1.1 hours, which are not exactly periodic. The durations of the deep and shallow

---

[1] http://heasarc.gsfc.nasa.gov/docs/heasarc/caldb/swift/docs/xrt/SWIFT-XRT-CALDB-09_v16.pdf

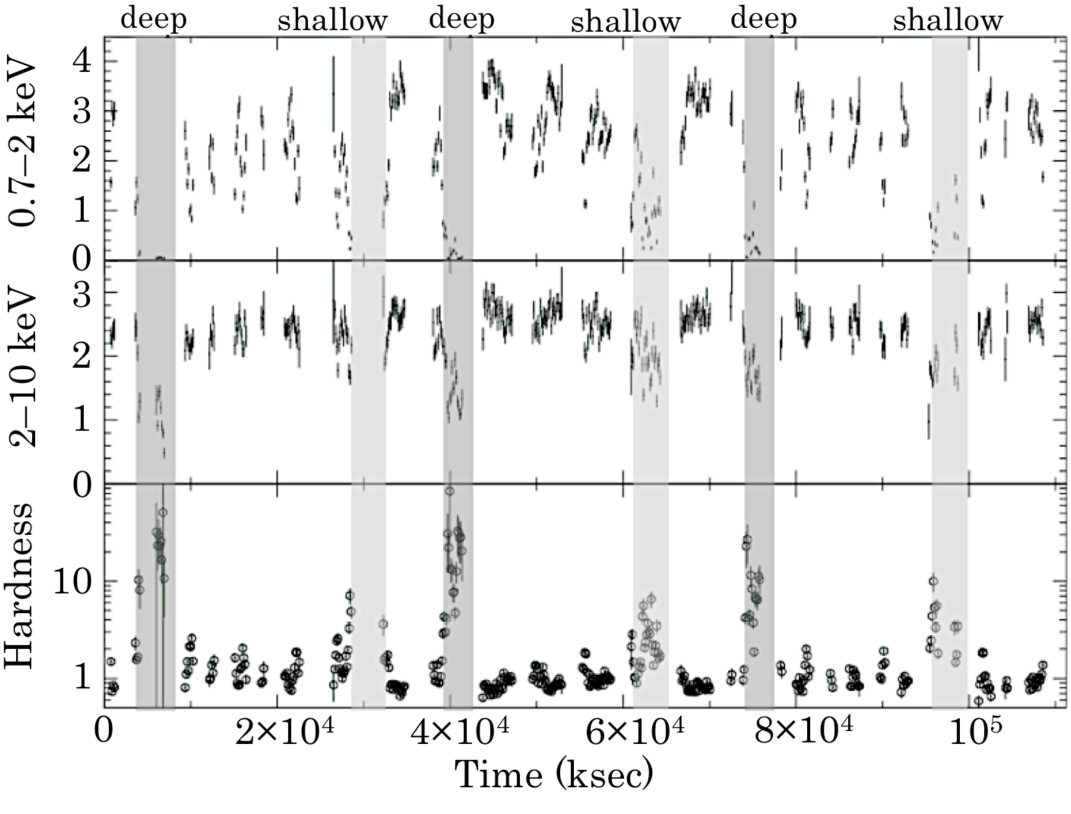

Figure 4.1: XIS-3 light curves in 0.7–2 keV and 2–10 keV, and their ratio in 128 sec binning, from top to bottom. The shadowed regions represent the periods of the deep dips (dark gray) and the shallow dips (light gray).

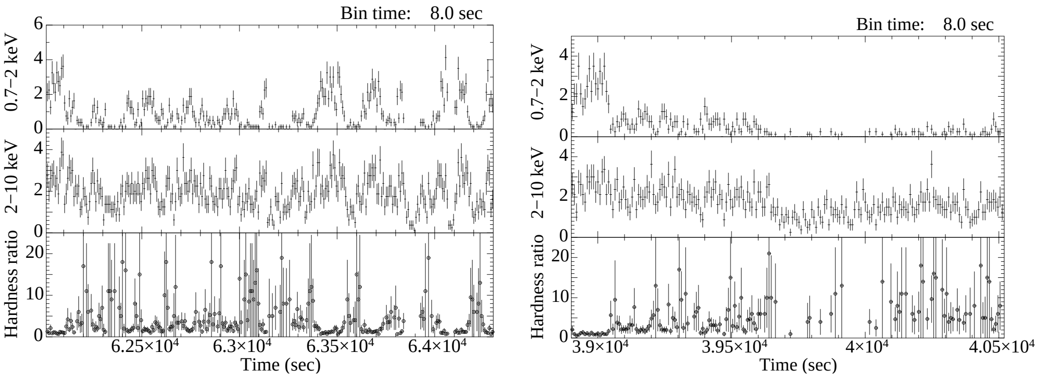

Figure 4.2: Same as Figure 4.1 in 8 second bins. The upper and lower panels present the phases of a shallow dip and a deep dip, respectively.

dips (1.0–1.7 hours) are comparable or larger than those of the data gaps. Because the hardness ratio never exceeds 2.6 outside of the dip phases we identified, it is unlikely that the actual period is shorter than 9.74 hours and we miss other dip events in these data gaps. We also note that dips do not always appear precisely in the same orbital phase, and the interval between the first and second deep dips actually 50 sec longer than that of second and third deep dips, when we measure them from the light curve with shorter time bins. The interval from a deep dip to the next shallow dip is derived to be 6.38±0.04 hours, which is obtained by averaging the intervals between the beginning of deep dips and those of the following shallow dips. However, the durations of the deep and shallow dips are not precisely constant, and consequently their intervals are slightly different event by event.

Figure 4.3 shows the normalized PDSs in the non-dip phases in the 0.7–1 keV, 1–5 keV, and 5–10 keV bands, calculated from the combined light curve of all three XISs with 8 sec bins. We find that the softer energy band has much larger power than those of the harder bands in the frequency range of 10^{-3} to 5×10^{-2} Hz. This suggests that the power is likely dominated by the residual variability of absorption that exists even outside the dips. The source has only small intrinsic power ($\approx 1 \times 10^{-3}$ rms^2/mean^2) in the 5–10 keV band, where the flux variabilities are little affected by absorption. Thus, this frequency region is likely below the low frequency break of the band-limited noise observed from BHXBs in the low/hard state.

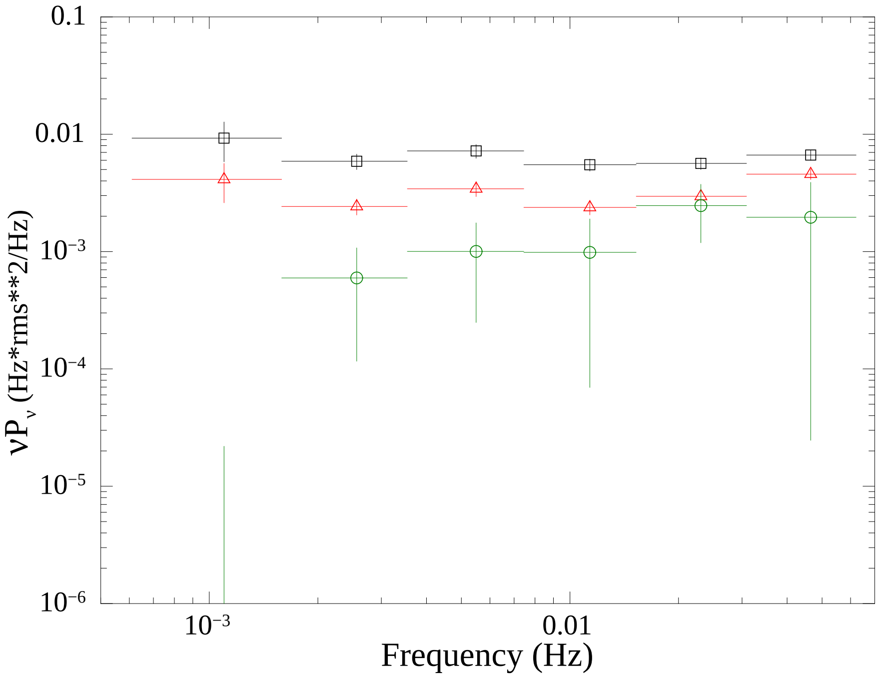

Figure 4.3: XIS power density spectra in the 0.7–1 keV (black, square), 1–5 keV (red, triangle), and 5–10 keV (green, circle) bands, created by using the XIS-0+XIS-1+XIS-3 light curve in the non-dip phases with 8 sec bins. They are normalized in the way that their integral gives the squared root mean squared fractional variability. White noise is subtracted.

4.3.2 Modeling Time-averaged Non-dip Spectrum

We extract the time-averaged XIS and HXD spectra in the deep dip, shallow dip, and non-dip phases and analyze them separately. In this subsection we concentrate on the non-dip spectra. We utilize the energy bands of 0.7–9.0 keV, 0.7–8.0 keV, 12–70 keV, and 50–130 keV for FI-XISs, BI-XIS, HXD/PIN, and HXD/GSO, respectively, where the signal-to-noise ratios are sufficiently good and the calibration is the most reliable.

The non-dip spectrum is roughly characterized by a power-law component extended up to 130 keV with a photon index of $\approx 1.591 \pm 0.005$ (χ^2/d.o.f. = 1472/1171), although we find broad depressions around 0.75 keV and 0.9 keV. These structures likely correspond to the photoelectronic absorption lines and/or edges of highly ionized oxygen-K and iron-L shells, which are similar to "warm absorbers" seen in many active galactic nuclei such as MCG-6–30–15 (e.g., Nandra & Pounds 1992; Fabian et al. 1994) and NGC 4051 (e.g., Pounds et al. 1994; Mihara et al. 1994). The hard spectral shape suggests that the source stayed in the low/hard state during our observation. The exponential cutoff is not detected within the energy band of the non-dip spectrum (<130 keV), and therefore in the following analysis, we fix the cutoff energy at 300 keV, which is within the typical value observed from BHXBs in the low/hard state ($\lesssim$300 keV; see, e.g., Tanaka & Shibazaki, 1996).

To investigate the detailed properties of the accretion flow and the ionized absorber, we next analyze the non-dip spectrum with a more sophisticated model. Following the general description of the X-ray spectrum in the low/hard state (e.g., Gierliński et al., 1997), we adopt a model composed of the multicolor disk (MCD) emission and its thermal Comptonization. The `nthcomp` model (Zdziarski et al. 1996; Życki et al. 1999) and the `diskbb` model (Mitsuda et al., 1984) are employed to represent the Comptonization and direct emission from the disk, respectively. We assume that all the seed photons for the Comptonized component are produced by the disk, and link the seed temperature of the `nthcomp` model to the inner disk temperature of the MCD component. We add `phabs` as interstellar absorption, assuming the solar abundance. To consider reflection of Comptonized photons on the disk, we convolve the `nthcomp` component with the `reflect` model. This model calculates a reflected spectrum from neutral material (Magdziarz & Zdziarski, 1995)[1]. The `reflect` model does not contain

---

[1] We examine the ionization level of the reflector utilizing the `ireflect` model, an ionized version of `reflect`, but the ionization parameter (ξ) is not constrained at all. We obtain the minimum reduced

the iron Kα emission line, whose equivalent width is $\approx$ 1 keV with respect to the reflected continuum, as suggested by numerical calculations (e.g., Matt et al., 1991). Hence, we add a Gaussian component as the iron-Kα emission line and fix the line energy and the line width at 6.4 keV and 10 eV, respectively. The normalization of Gaussian component is linked to the reflection strength $\Omega/2\pi$ of the `reflect` model so that the equivalent width with respect to the reflection continuum is $\approx$ 1 keV (e.g., Matt et al., 1991).[1] The reflection spectrum is smeared with `kdblur`, which calculates relativistic effects from an accretion disk around a rotating black hole using the results of Laor (1991). We assume an inclination angle of 75° (see Section 4.5.1) and an index for the radial dependence of emissivity (β, where emissivity $\propto r^{-\beta}$) of 3, as well as an outer radius of 400 R_g (R_g represents the gravitational radius, GM_BH/c^2). The inner radius is first left as a free parameter, but it is totally unconstrained. We therefore fix the inner radius at 100 R_g in the following spectral fits. The energy range for the model calculation is extended to 0.1–1000 keV to apply the convolution models.

To analyze the ionized absorption features, we create a photoionized absorption model with the spectral synthesis code XSTAR version 2.2.1bk, assuming that the ionized absorber has the solar abundances and that its turbulent velocity is 300 km sec^{-1}. This model can be used in XSPEC as an multiplicative component with free parameters of the equivalent hydrogen column density (N_H), ionization parameter ($\xi = L_\mathrm{X}/n_\mathrm{H}R^2$, where L_X, n_H, and R represent the ionizing flux in the energy range of 1–1000 Ry (Rydberg unit; 1 Ry = 13.6 eV), the number density of hydrogen nuclei, and the distance from the X-ray source to absorber, respectively), and the Doppler shift. The absorption spectra calculated with XSTAR depend on the spectral shape of the incident radiation on the absorber. We first adopt a single power-law model with a photon index of 1.6 as the input spectrum for XSTAR and fit the resulting model to the non-dip spectrum. Next, we re-create an XSTAR absorption model using the best-fit unabsorbed continuum model and then refit the spectrum with the newly obtained absorption model. These steps are performed in an iterative manner, until the parameters of the continuum model become identical to those obtained in the previous

---

chi-squared in the case of a neutral reflector ($\xi = 0$).

[1] We first fitted with the strength of the Gaussian unlinked with that of the reflection continuum. However, the upper limit of the line flux was found to be unreasonably small, an order of magnitude lower than what is expected from the equivalent width with respect to a reflection continuum ($\approx$ 1 keV).

iteration within the ranges of 90% errors. In the following, we show the final best-fit results after the iteration.

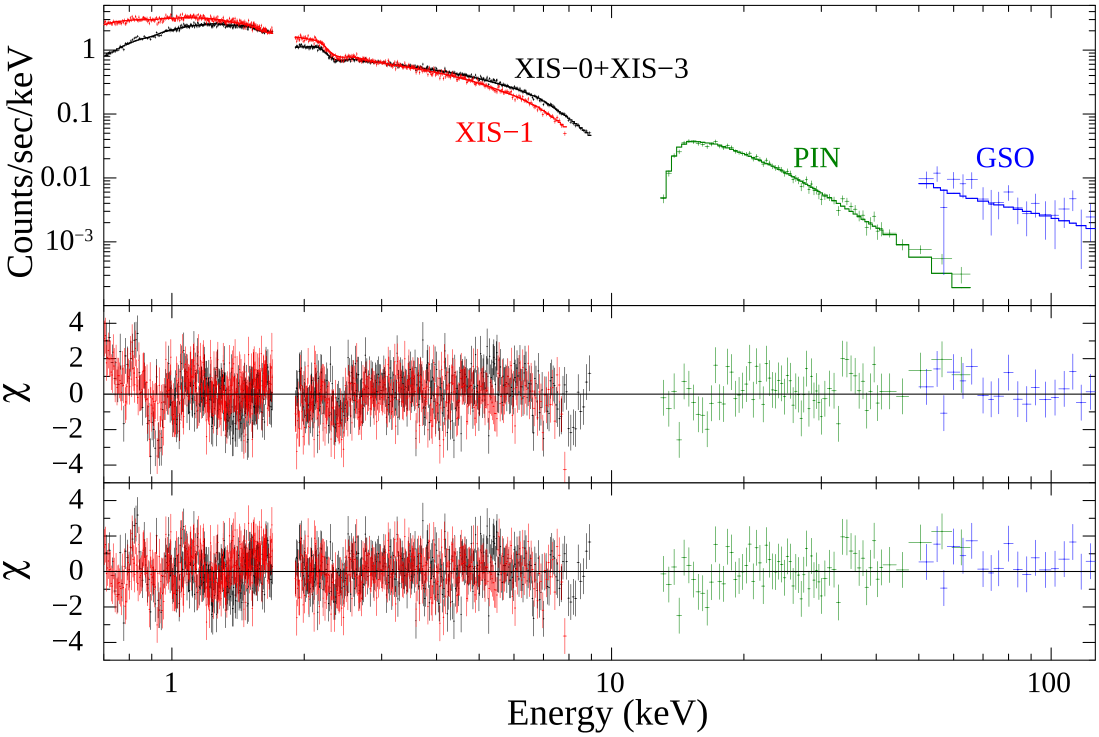

Figure 4.4: Time-averaged *Suzaku* spectra in the non-dip phases fitted with a disk and Comptonization components are plotted in the top panel. The middle and bottom panels show the residuals of the fits with the power-law model and the `diskbb` + `nthcomp` model, respectively.

The final fitting model is thus expressed as `phabs*xsabs*(diskbb+kdblur*(gaussian+reflect*nthcomp))`, where `xsabs` represents the XSTAR ionized absorption model. The spectra and the best-fit model are shown in Figures 4.4 and 4.5, and the resulting parameters are given in Table 4.1. We find that this model describes the *Suzaku* spectra reasonably well, with χ^2/d.o.f. = 1269/1165. The fit quality is improved from that of the power-law model with an F-test probability of 1×10^{-34}. The ionization parameter and column density are estimated as $\log \xi = 2.19 \pm 0.04$ and $N_{\rm H} = (6.1^{+1.0}_{-0.9}) \times 10^{21}$ cm^{-2} for the ionized absorber, respectively. The Doppler shift is not detected with an upper limit of < 2300 km sec^{-1}. A small inner disk temperature ($0.168^{+0.008}_{-0.006}$ keV) and a large normalization of the MCD model ($6.0^{+3.4}_{-2.4} \times 10^3$) are obtained, which suggest that the standard disk is truncated (see Section 4.5.3) during the *Suzaku* observation. The

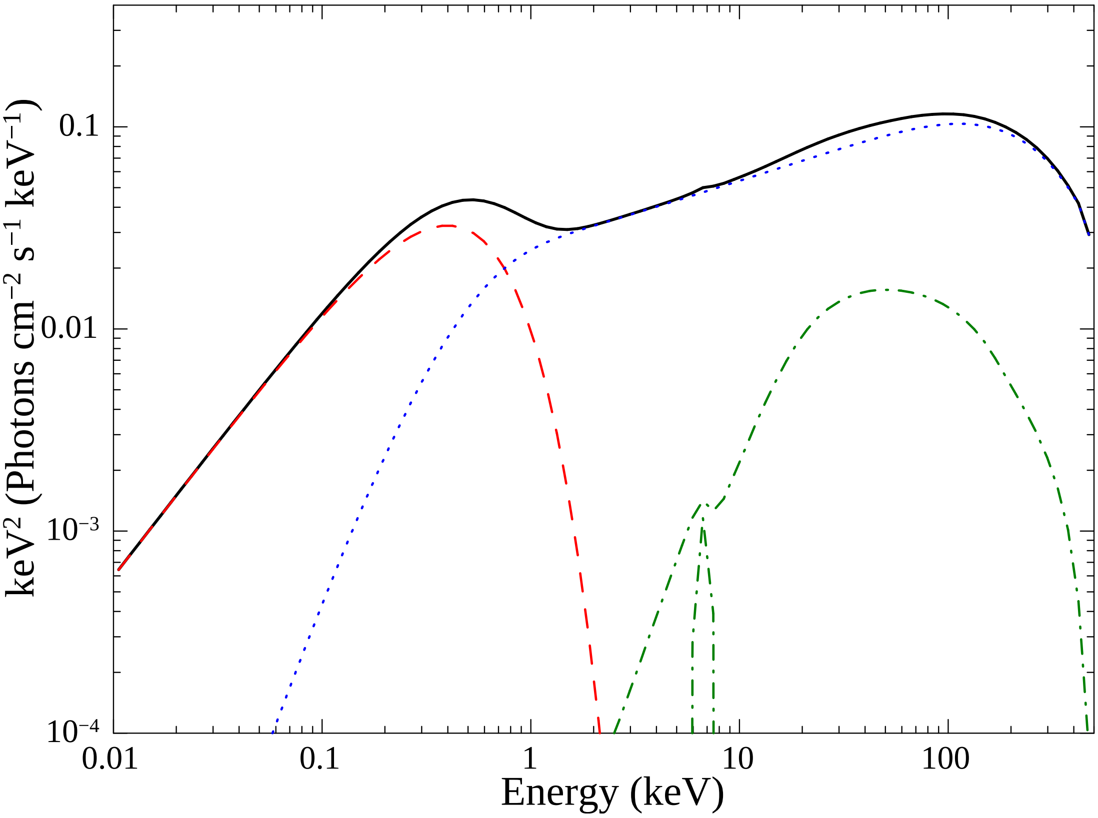

Figure 4.5: The best-fit disk + Comptonization spectrum (black, solid) and each component corrected for absorption are separately plotted in the νF_ν form. The red (dashed), blue (dotted), green (dash-dotted) lines represent the disk, Comptonization, reflection components, respectively.

Component	**Parameter**	**non-dip**	**deep dip**	**shallow dip**
phabs	$N_{\rm H}$ (10^{22} cm^{-2})	0.12 ± 0.03	$0.23^{+0.05}_{-0.04}$	0.17 ± 0.02
xsabs	$N_{\rm H}$ (10^{22} cm^{-2})	$0.61^{+0.10}_{-0.09}$	14.4 ± 0.6	$6.6^{+0.5}_{-0.4}$
	$\log \xi$	2.19 ± 0.04	1.90 ± 0.07	1.79 ± 0.07
	blue shift (km)[c]	< 2300	< 2700	< 5800
	covering fraction	1 (fix)	0.91 ± 0.01	$0.72^{+0.03}_{-0.04}$
diskbb	$kT_{\rm in}$ (keV)	$0.168^{+0.008}_{-0.006}$		
	norm	$6.0^{+3.4}_{-2.4} \times 10^3$		
nthcomp	Γ	$1.70^{+0.03}_{-0.02}$		
	$E_{\rm cut}$ (keV)	300 (fix)		
	norm	$2.46^{+0.09}_{-0.08} \times 10^{-2}$		
reflect	$\Omega/2\pi$	0.4 ± 0.2		
	i (deg)	75 (fix)		
gauss[a]	$E_{\rm cen}$ (keV)	6.4 (fix)		
	σ (eV)	10 (fix)		
χ^2/d.o.f.		1269/1165	540/535	1070/994
flux[b]		1.3×10^{-10}	7.1×10^{-11}	1.0×10^{-10}

Table 4.1: Best-fit parameters of *Suzaku* spectra in the deep dip, shallow dip, and non-dip periods.

[a] The normalization of Gaussian component is linked to the reflection strength $\Omega/2\pi$ of the `reflect` model so that the equivalent width with respect to the reflection continuum is ≈ 1.0 keV.

[b] absorbed 1–10 keV flux (ergs cm^{-2} sec^{-1}).

[c] Positive values represent blue shifts.

Notes. The non-dip spectrum is fitted with `phabs*xsabs*(diskbb+kdblur*(reflect*nthcomp+gauss))`, where `xsabs` is an ionized absorption model created with XSTAR. In fitting the two dip spectra, all the parameters except for those of the neutral and ionized absorption components are fixed at the best-fit values of the non-dip spectrum. The blank columns in the table of the dip spectra are the fixed parameters. Partial covering of the ionized absorber is included in the model of dipping spectra.

hydrogen column density of neutral absorption, $(1.2 \pm 0.3) \times 10^{21}$ cm^{-2}, is comparable to the total Galactic column in the direction of MAXI J1305−704 ($\approx 1.8 \times 10^{21}$ cm^{-2}), estimated from the HI all-sky map by Kalberla et al. (2005) by utilizing the `nh` ftool.

Recent *Suzaku* observation of BHXBs in the low/hard state have revealed that the Comptonized plasmas are more complex than a single-zone homogeneous structure. Takahashi et al. (2008), Makishima et al. (2008), and Shidatsu et al. (2011b) reproduced the time-averaged spectra with double Comptonization components that have different optical depths. Furthermore, Yamada et al. (2013a) successfully separated the second variable component from the *Suzaku* spectra of Cyg X-1 in the low/hard state by considering timing information. Here we investigate whether or not these complex structures are also detected in MAXI J1305−704. We add another `nthcomp` component to the single `nthcomp` model to consider the double Comptonization corona. The seed temperatures of the two `nthcomp` models are linked to the inner disk temperature of the MCD component. We find, however, that this "double `nthcomp`" model does not improve the fit.

4.3.3 Analysis of Dip Spectra

We analyze the deep and shallow dip spectra with the same model that used for the non-dip spectrum. Figure 4.6 compares the XIS and HXD spectra in the deep dip, shallow dip, and non-dip phases. We obtain the HXD/PIN spectrum up to 60 keV for the shallow dip and up to 50 keV for the deep dip. The HXD/GSO data in the dips are not usable due to the limited photon statistics, however. We employ the final results described in the previous section and fix all the parameter at the best-fit value of the non-dip spectrum, except for those of the neutral and ionized absorption components. Considering that dipping spectra are often modeled with partial absorbers, we introduce a covering fraction of the ionized absorber. The total fitting model for the dip spectra is described as `phabs*(f*xsabs+(1-f))*(diskbb+kdblur*(gaussian+reflect*nthcomp))`, where `f` corresponds to the covering fraction.

This model successfully reproduce the dip spectra, yielding χ^2/d.o.f. = 540/535 and 1070/994 for the deep and shallow dips, respectively. We find that the two dip spectra can be described with more than one order of magnitude larger column densities and about a factor of 2 smaller ionization parameters than those of the non-dip spectrum. The column density of the deep dip is twice as much as that of the shallow dip. The

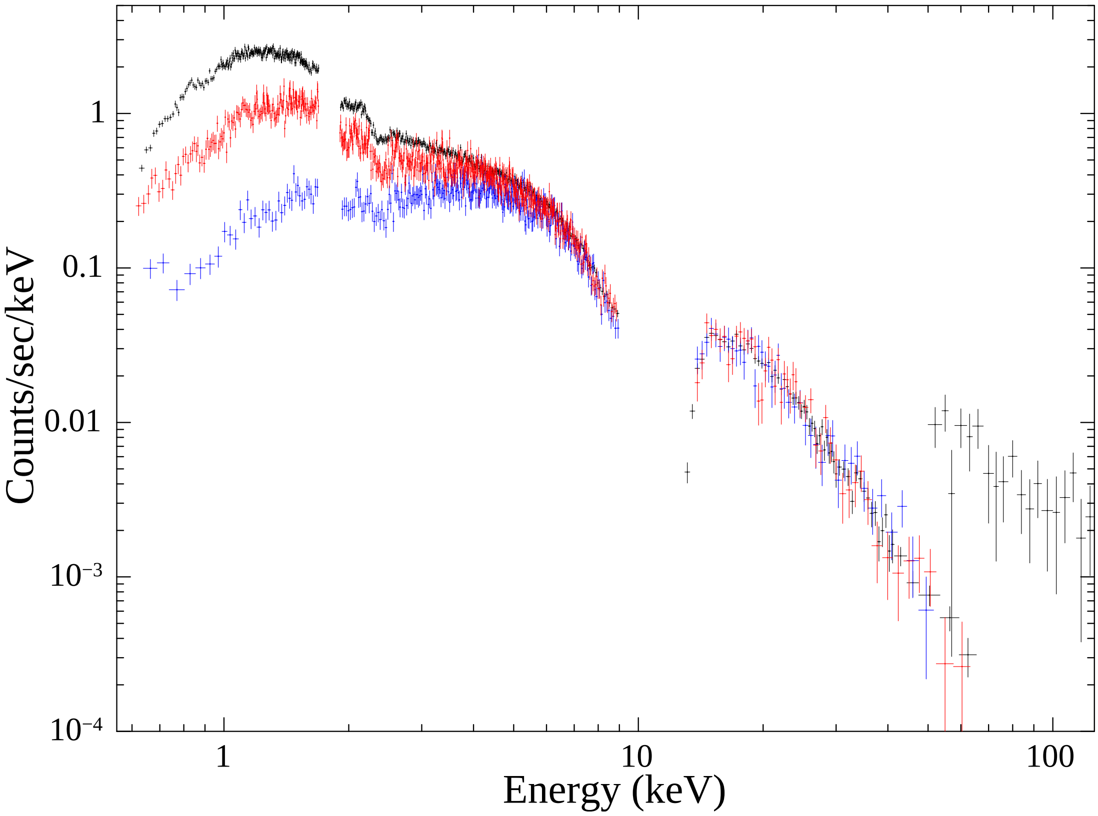

Figure 4.6: Time-averaged *Suzaku* spectra in the deep dip (blue, hardest one) and the shallow dip (red, second hardest one), compared with that in the non-dip period (black). The XIS-1 spectra are not shown for clarity.

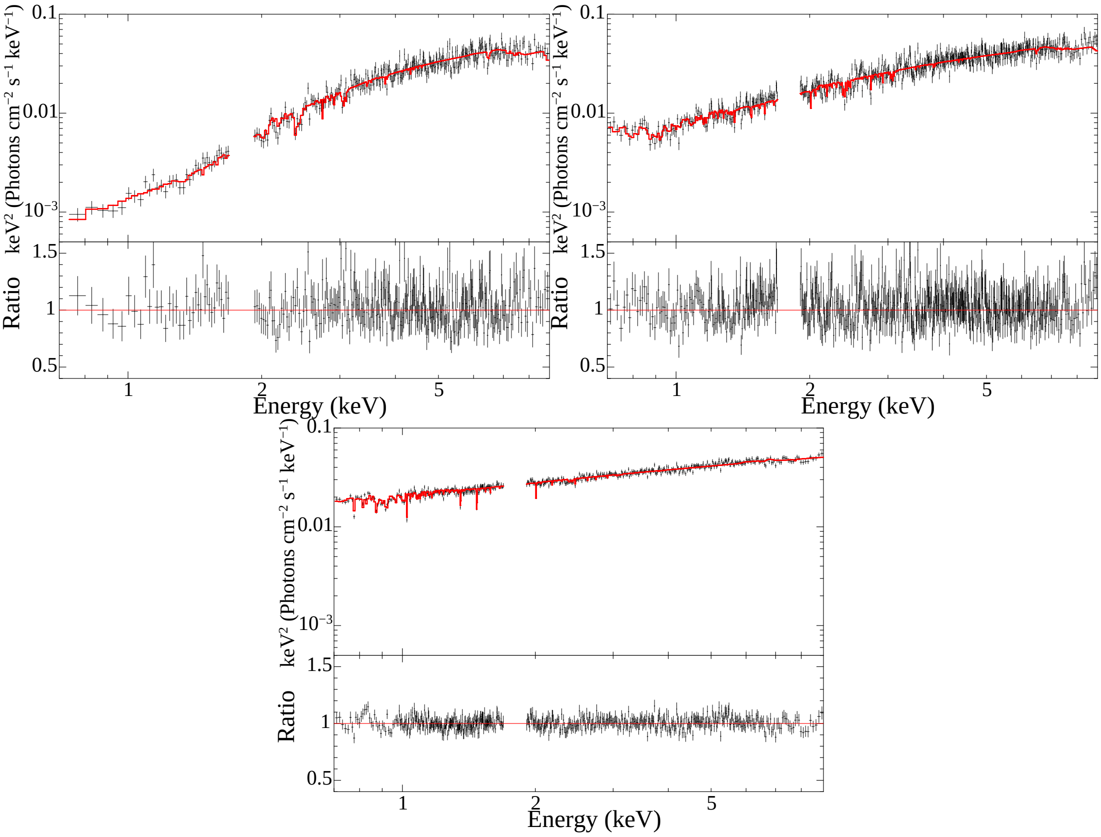

Figure 4.7: The spectra, best-fit models, and data vs. model ratios in the dipping and non-dip phases. The top, middle, and bottom panels show the results in the deep dip, shallow dip, and non-dip phases, respectively. The dipping spectra are fitted with the best-fit model of the non-dip spectrum. The XIS-1 and HXD spectra are ignored in all panels for illustrating purposes.

covering fraction f is estimated as $0.72^{+0.03}_{-0.04}$ for the shallow dip, while the deep dip spectrum is almost totally absorbed, with $f = 0.91 \pm 0.01$. The resulting parameters are listed in Table 4.1 and the best-fit spectra are plotted in Figure 4.7.

The xsabs model do not include the Comptonization in the ionized absorber itself. This might affect the fits, particularly for the deep dip spectrum, in which the ionized absorber has a relatively large column density ($N_{\rm H} \sim 10^{23}$ cm^{-1}). To account for the possible effects of Compton scattering, we add the `cabs` model to the final model with its column density linked to that of the ionized absorber, and re-fit the deep dip spectrum. We find, however, that the effects are negligible and all the parameters remain unchanged within their 90% confidence ranges. We confirm that the energy dependence of the scattering cross section which is not included in `cabs`, is also negligible in our energy range. The column density of the deep dip corresponds to an optical depth of $\tau \approx 0.1$ in Thomson scattering, which only reduces to $\tau \approx 0.08$ at 50 keV.

4.3.4 *Swift*/XRT Spectrum in the High/soft State

To compare the *Suzaku* non-dip spectrum in the low/hard state with spectra in the high/soft state, we analyze a *Swift*/XRT spectrum of MAXI J1305−704 obtained from 2012 April 19 to 21 during the high/soft state. As described in Miller et al. (2012b), these XRT data also show dipping behaviors. We create a time-averaged non-dip spectrum by extracting the events when the count rate exceeds 20 counts sec^{-1} in the 1–10 keV light curve with 16 sec bins. Following the release note for the *Swift* XRT CALDB[1], we use the data down to 0.3 keV for the following spectral fit, where the calibration of the energy response is reliable.

First we fit the XRT spectrum using an MCD model with a neutral absorption. A `simpl` model (Steiner et al., 2009) is also incorporated to account for Comptonization, with a fixed photon index of 2.2, a typical value in the high/soft state of BHXBs (e.g., Done et al., 2007; Ebisawa et al., 1994; Kolehmainen et al., 2011). We extend the energy range to 0.01–100 keV for the model calculation as `simpl` is a convolution model. We find that this model, `phabs*simpl*diskbb`, roughly describes the XRT spectrum with an inner disk temperature (≈ 1.0 keV) and a small scattering fraction ($< 2.6\%$ of the total disk emission), although the fit is far from acceptable (χ^2/d.o.f. = 1749/370) mainly due to the broad absorption- (and/or emission-) like structures in the soft band below ≈1 keV. These large residuals are probably a composition of the iron-L absorption lines, which are detected in the *Chandra* HETGS observation on 10 days after the *Swift* observation, as reported by Miller et al. (2012c). The XRT spectrum also has a narrow absorption line at about 6.6 keV, which likely corresponds to Kα lines of highly ionized iron ions. By fitting the line with a negative Gaussian, its center energy, line flux, and equivalent width are estimated to be $6.57^{+0.09}_{-0.08}$ keV, $2.7^{+1.4}_{-1.1} \times 10^{-4}$ ergs cm^{-2} sec^{-2}, and 49^{+27}_{-23} eV, respectively.

---

[1] http://heasarc.gsfc.nasa.gov/docs/heasarc/caldb/swift/docs/xrt/SWIFT-XRT-CALDB-09_v16.pdf

We find that the unabsorbed flux in the 0.01–100 keV band, 1.4×10^{-9} erg cm^{-2} sec $^{-1}$, is only ≈ 2.3 times larger than that of the *Suzaku* non-dip spectrum (6.1×10^{-10} erg cm^{-2} sec $^{-1}$). This suggests that MAXI J1305−704 was in a relatively faint high/soft state and that the bolometric luminosity in the *Swift* observation was comparable with that in the soft-to-hard transition, typically $\approx 0.02 L_{\rm Edd}$ (Maccarone, 2003). However, the inner disk temperature is too high to be expected for such a faint high/soft state with a low accretion rate. This could be understood in the way that the strong relativistic beaming effects due to a high inclination angle and/or a high black hole spin significantly modify the disk spectrum and consequently we obtain an apparently higher inner temperature than the intrinsic one. We therefore replace `diskbb` with `bhspec` (Davis et al., 2005), a relativistic disk emission model, to fit the spectra (i.e., `phabs*simpl*bhspec`; Model 1 in Table 4.2). The `bhspec` model calculates the radiation transfer in the accretion disk around a black hole by self-consistently considering its vertical structure. The model parameters are the black hole mass ($M_{\rm BH}$), spin parameter ($a = cJ/GM_{\rm BH}^2$, where J represents angular momentum of the black hole), distance, inclination angle, disk luminosity, and the α parameter, which we fix at 0.01. Here we assume a black hole mass of $M_{\rm BH} = 3M_\odot$, a high inclination, $i = 75°$ (see Section 4.5.1), and a disk luminosity corresponding to $0.05 L_{\rm Edd}$, and leave a and the normalization K, which is related to the distance d via $K = (10 \text{ kpc}/d)^2$, as free parameters. We find that the *Swift*/XRT spectrum favors this `bhspec` model better than the `diskbb` model with a smaller reduced chi-squared value (χ^2/d.o.f. = 1687/370). A moderate spin parameter ($a \approx 0.7$) is obtained.

To investigate the properties of the ionized absorber responsible for the structures at 6.6 keV and below ≈ 1 keV, we create a multiplicative photoionized absorption model by utilizing XSTAR to fit the non-dip XRT spectrum. We adopt an MCD with an inner temperature of 1.0 keV as the incident spectrum in the energy range of 1–1000 Ry. The ionized absorber is assumed to have the solar abundances and a turbulent velocity of 300 km sec^{-1}. The fit is much improved (χ^2/d.o.f. = 1018/367) by using this model, `phabs*xsabs*simpl*bhspec` (Model 2 in Table 4.2), where the `xsabs` represents the photoionized absorption. We obtain an ionization parameter of $\log \xi \approx 2.6$ and an equivalent hydrogen column density of $\approx 8 \times 10^{22}$ cm^{-2}.

The fit is still far from acceptable, however, due to the large residuals at around 0.7 keV and 1.2 keV, which cannot be explained by calibration uncertainties of the

Component	**Parameter**	**Model1**[a]	**Model2**[b]	**Model3**[c]	**Model4**[d]
phabs	$N_{\rm H}$ (10^{22} cm^{-2})	0.097 ± 0.002	0.123 ± 0.004	$0.097^{+0.020}_{-0.018}$	0.098 ± 0.006
xsabs1[e]	$N_{\rm H}$ (10^{22} cm^{-2})	–	$7.8^{+1.4}_{-1.3}$	$5.1^{+3.8}_{-2.8}$	$5.8^{+41.7}_{-3.4}$
	$\log \xi$	–	2.64 ± 0.06	$2.86^{+0.52}_{-0.18}$	$3.13^{+1.87,\rm pegged}_{-0.26}$
	blue shift (km)[f]	–	1700^{+1000}_{-1200}	< 4800	< 4300
xsabs2[e]	$N_{\rm H}$ (10^{22} cm^{-2})	–	–	$1.0^{+0.4}_{-0.3}$	$1.5^{+0.6}_{-0.5}$
	$\log \xi$	–	–	1.2 ± 0.2	1.7 ± 0.1
	blue shift (km)[f]	–	–	0 (fix)	0 (fix)
diskbb	$T_{\rm in}$ (keV)	–	–	–	$0.88^{+0.03}_{-0.04}$
	norm	–	–	–	139^{+26}_{-45}
bhspec[g]	a	0.69 ± 0.01	0.56 ± 0.02	0.46 ± 0.06	–
	norm	$1.77^{+0.01}_{-0.02}$	2.35 ± 0.06	$2.5^{+0.3}_{-0.2}$	–
simpl	Γ	2.2 (fix)	2.2 (fix)	2.2 (fix)	2.2 (fix)
	scattering fraction	< 0.003	0.02 ± 0.01	0.03 ± 0.01	0.04 ± 0.01
gauss	line energy (keV)	–	–	$1.17^{+0.03}_{-0.04}$	$1.18^{+0.06}_{-0.05}$
	σ			0.14 ± 0.03	$0.12^{+0.04}_{-0.07}$
	norm	–	–	$0.022^{+0.009}_{-0.008}$	$0.017^{+0.006}_{-0.008}$
	E.W. (eV)	–	–	61^{+35}_{-22}	53^{+32}_{-29}
gauss	line energy (keV)	–	–	0.74 ± 0.01	0.75 ± 0.01
	σ			0.10 ± 0.01	0.10 ± 0.01
	norm	–	–	0.11 ± 0.01	0.10 ± 0.01
	E.W. (eV)	–	–	159^{+22}_{-14}	183^{+18}_{-17}
χ^2/d.o.f		1687/370	1018/367	294/359	292/359

Table 4.2: Fitting results of *Swift*/XRT non-dip spectrum.

[a] `phabs*simpl*bhspec`.

[b] `phabs*xsabs1*simpl*bhspec`.

[c] `phabs*(xsabs2*xsabs1*simpl*bhspec+gauss+gauss)`.

[d] `phabs*(xsabs2*xsabs1*simpl*diskbb+gauss+gauss)`, for direct comparison with the disk flux obtained from the *Suzaku* non-dip spectrum.

[e] Ionized absorption model created with XSTAR. Incident spectrum is defined as the `diskbb` model with a inner temperature of 1.0 keV. We assume a turbulent velocity of 300 km sec^{-1}.

[f] Positive values represent blue shifts.

[g] We assume $i = 75°$, $M_{\rm BH} = 3M_{\odot}$, luminosity $= 0.05L_{\rm Edd}$, and $\alpha = 0.01$, where α represents the viscosity parameter in the Shakura & Sunyaev (1973) prescription for the stress $\tau_{r\phi} = \alpha \times P$ (P is the total pressure).

response. The iron-K absorption line is not well modeled either, likely because these large structures at around 1 keV lead to wrong constraints on the parameters of the ionized absorption component. Moreover, the residuals are not originated from the uncertainties of `bhspec` in modeling absorption edges. We confirm that the quality of fit is not improved by replacing the `bhspec` component with another relativistic disk emission model, `kerrbb`, which does not consider the vertical structure of the disk and has no absorption edges. Furthermore, they are reproduced neither by ionized O and Ne edges of additional absorption components nor by a superposition of emission lines created by the ionized absorber, which can never produce huge equivalent widths to fit the structures. We also change the oxygen, neon and iron abundances in the model, which could produce artificial emission and/or absorption-like structures around 0.5–1.0 keV if not appropriate. While the fit is not improved by varying the iron abundance, a better fit is obtained with a smaller oxygen abundance: χ^2/d.o.f. = 734/367 for an oxygen abundance of 0.5 in the solar unit both for neutral and ionized absorbers. Nevertheless, we find that huge residuals still remain at ≈ 0.7 keV even in the extreme case of no oxygen. A larger neon abundance also gives a better fit but the improvement of chi-squared value is not as significant as the oxygen abundance (at best χ^2/d.o.f. = 930/366 for a neon abundance of 9.0 in the solar unit). Thus, the oxygen and neon abundances in the absorbers cannot entirely explain the differences between the data and model in the soft energy band.

We find that the structures below $\approx$1 keV are well reproduced by empirically adding two broad Gaussian components at 0.75 keV and 1.2 keV with line widths of $\approx$ 100 eV and 140 eV, and equivalent widths of $\approx$ 160 eV and 60 eV, respectively. The fit is significantly improved and becomes acceptable (χ^2/d.o.f. = 313/361) with this model `phabs*(xsabs*simpl*bhspec+gauss+gauss)` where the solar abundances are assumed for both the ionized and neutral absorbers. For the ionized absorber, the resulting ionization parameter is $\log \xi = 1.7 \pm 0.1$ and the column density is $(1.4^{+0.4}_{-0.3}) \times 10^{22}$ cm^{-2}. However, the equivalent width of the iron-K absorption line estimated from this model is somewhat smaller than what is actually seen in the *Swift*/XRT spectrum. We therefore add another ionized absorption component and fit the spectrum with the model expressed as `phabs*(xsabs*xsabs*simpl*bhspec+gauss+gauss)` (Model 3 in Table 4.2). This model excellently describes the overall spectrum and further decreases the reduced chi-squared value (χ^2/d.o.f. = 294/359). The resulting model is

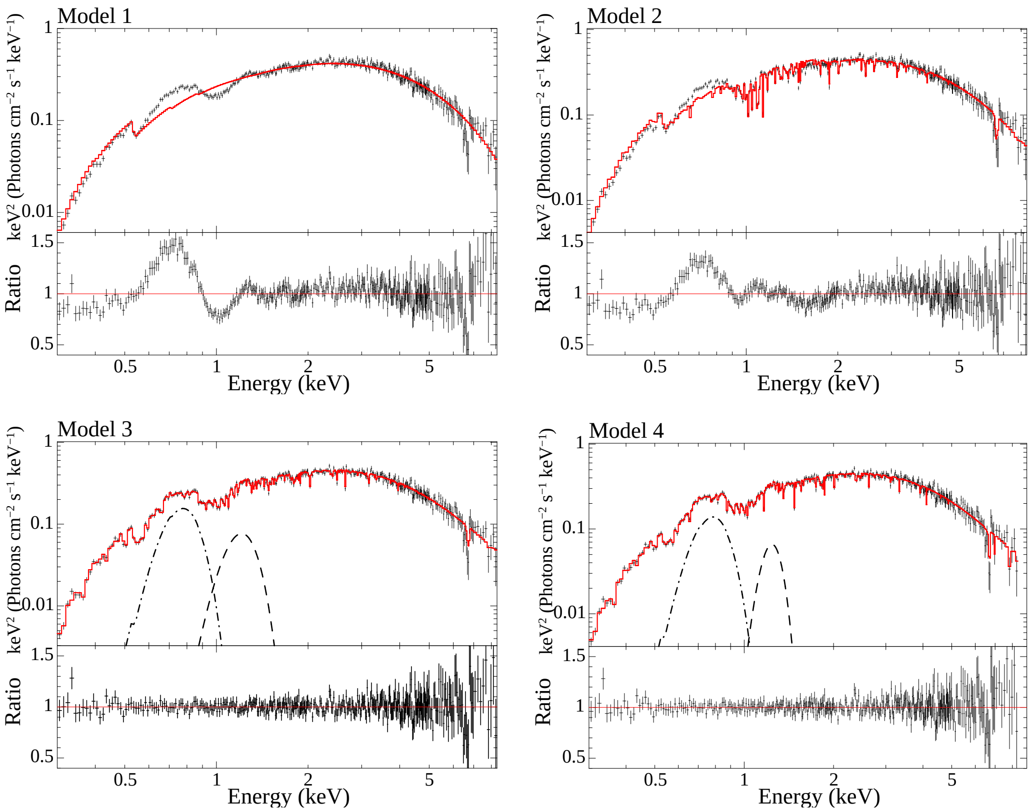

Figure 4.8: The time-averaged spectrum of the XRT spectrum fitted with various models. The lower panel represents the data vs. model ratios in each bin. Top left: `phabs*simpl*bhspec`. Top right: `phabs*xsabs1*simpl*bhspec`. Bottom left: `phabs*(xsabs1*xsabs2*simpl*bhspec+gauss+gauss)`. Bottom right: `phabs*(xsabs1*xsabs2*simpl*diskbb+gauss+gauss)`, where "xsabs" is the ionized absorption model created with XSTAR.

plotted in Figure 4.8, and the best-fit parameters are given in Table 4.2. The ionization parameter and column density are $\log\xi = 2.86^{+0.52}_{-0.18}$ and $5.1^{+3.8}_{-2.8} \times 10^{22}$ cm^{-2} for one ionized absorber responsible for the iron Kα absorption line, and $\log\xi = 1.2 \pm 0.2$ and $1.0^{+0.4}_{-0.3} \times 10^{22}$ cm^{-2} for the other. The spin parameter is estimated as $a = 0.46 \pm 0.06$.

For direct comparison of the disk emission between the low/hard state (*Suzaku*) and the high/soft state (*Swift*), we replace `bhspec` in the final model with `diskbb` (`phabs*(xsabs*xsabs*simpl*diskbb+gauss+gauss)`; Model 4 in Table 4.2) and fit the *Swift*/XRT spectrum. The fit is again acceptable (χ^2/d.o.f. = 292/359), and the inner disk temperature and normalization of `diskbb` are estimated to be $0.88^{+0.03}_{-0.04}$ keV

Date (2012)	**Number of observations**[a]	**Integration time in each frame (sec)**	**Magnitude**[b,c] J	H	K_S
Apr. 27	1	30	15.95 ± 0.53	15.69 ± 0.57	14.99 ± 0.59
Apr. 28	1	30	15.84 ± 0.51	15.49 ± 0.49	15.32 ± 0.59
Apr. 29	54	30	15.74 ± 0.47	15.43 ± 0.47	15.19 ± 0.47
Jul. 22	1	15	16.63 ± 0.10	16.20 ± 0.05	15.86 ± 0.09
Jul. 23	1	15	16.46 ± 0.04	16.08 ± 0.04	15.88 ± 0.08
Jul. 24	1	15	16.66 ± 0.05	16.24 ± 0.03	16.03 ± 0.08

Table 4.3: Log of *IRSF* observations.

[a] 10 and 15 dithered frames are combined for each observation at the first and last three nights, respectively.

[b] All the object frames are added for each night separately to measure the magnitudes.

[c] Systematic errors due to the installation of the polarizer (3% of the observed magnitude at the maximum) are included in the data of the April observations.

and 139^{+26}_{-45}, respectively. The normalization is about 35 times smaller than that of the direct MCD component obtained from the *Suzaku* best-fit model. This indicates that the inner disk radius is smaller during the *Swift* observation in the high/soft state than during the *Suzaku* observation in the low/hard state. These *Swift*/XRT results are summarized in Table 4.2 and Figure 4.8.

4.4 Near-infrared Observations and Results

Photometric observations of MAXI J1305−704 in the J (1.25μm), H (1.63μm), and K_s (2.14μm) bands were carried out over six nights by using the SIRIUS camera (Nagayama et al., 2003) on the 1.4m *IRSF* telescope. The first three nights (2012 April 27, 28, and 29) were about 20 days after the beginning of outburst; the source was stayed in the high/soft state, while it was in the low/hard state on the last three nights (2012 July 22, 23, and 24). The July observations with *IRSF*/SIRIUS were made only one day after the end of the *Suzaku* X-ray observation. The typical seeing in full width at half maximum was ≈1".5–2".0 (3.5–4.5 pixels) in the J band. The observation log is given in Table 4.3.

We performed the standard data reduction (i.e., dark subtraction, flat-fielding, sky subtraction, and combining dithered images) with *IRSF* pipeline software on IRAF

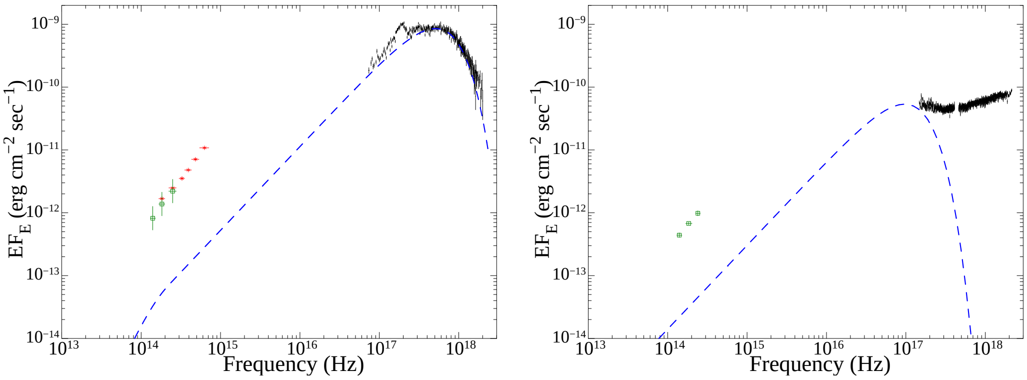

Figure 4.9: The spectral energy distributions of MAXI J1305−704 in the high/soft state and low/hard state are plotted in the left and right panels, respectively. The *IRSF* fluxes in the J (1.25 μm), H(1.63 μm), and K_S (2.14 μm) bands are obtained on 2012 April 29 (left) and July 22 (right), which are corrected for interstellar extinction (green, open square). The black points are the *Swift*/XRT (left) and *Suzaku* (right) spectra, corrected for neutral and ionized absorptions. Blue dashed lines show the intrinsic disk spectra including the Comptonized photons, where the outer disk radius is assumed to be the Roche lobe size. The optical and near-infrared fluxes obtained from the GROND observation on April 11 are also shown in the left panel (red cross).

version 2.16. We combined all the object frames obtained in one night to maximize the signal-to-noise ratio. We found the most probable near-infrared counterpart of MAXI J1305−704 at R.A. = $13^{\rm h}06^{\rm m}55^{\rm s}.3\pm0^{\rm s}.1$ and decl. = $-70°27'05''.1\pm0''.1$ (J2000), which is located in the *Swift*/XRT 90% error circle (Kennea et al., 2012a) and is consistent with the position of the optical/near-infrared counterpart discovered on April 11 by Greiner et al. (2012) with the GROND instrument mounted on the 2.2 m telescope in the MPI/ESO La Silla observatory. The *IRSF*/SIRIUS position is also consistent with those estimated in the *Swift*/UVOT (Ultraviolet/Optical Telescope) and *Chandra* HETGS observations (Greiner et al., 2012; Miller et al., 2012c) performed on April 10 and 29, respectively. The magnitudes in the three bands on each night are listed in Table 4.3. These were obtained by performing aperture photometry calibrated with the Two Micron All-Sky Survey (Skrutskie et al., 2006) photometric data of the stars in the field of view.

Figure 4.9 shows the *IRSF* fluxes on April 29 in the high/soft state (left panel) and on July 22 in the low/hard state (right panel). These fluxes were corrected for Galactic extinction. Considering the *Suzaku* and *Swift* results, we assumed the hydrogen column density of interstellar absorption as $N_{\rm H} = 1 \times 10^{21}$ cm^{-2} and derived the extinction in each band as $A_J = 0.15$, $A_H = 0.09$, and $A_K = 0.06$ by combining the conversion factors given by Predehl & Schmitt (1995) and Rieke & Lebofsky (1985).

In Figure 4.9, the quasi-simultaneous X-ray data obtained in the *Swift* and *Suzaku* observations are plotted in the left and right panel, respectively. The best-fit intrinsic disk components are separately shown. The X-ray spectra are corrected for both neutral and ionized absorptions. The GROND data in the optical and near infrared bands (g', i', r', z', J, and H; Greiner et al., 2012) are also plotted in Fig. 4.9 together with our *IRSF* ones obtained in the high/soft state. As noticed from the figure, these fluxes in the high/soft and low/hard states are ≈ 10 times larger than those of the intrinsic disk components estimated from the X-ray data. The flux levels in the optical and near infrared bands were decreased by ≈ 50% from the high/soft state to the low/hard state. These results suggest that in addition to the direct disk emission and the constant black body radiation from the companion star, another component (probably irradiation in the outer disk region) significantly contributes to the optical and near infrared fluxes (see also Section 4.5.1). The *IRSF* fluxes on July 24, which are the weakest ones of the six nights, correspond to the absolute magnitudes of 2.8, 2.4, and 2.1 in the J, H, and $K_{\rm S}$ bands (where the distance of MAXI J1305−704 is assumed as 6 kpc), respectively. If the companion is a main-sequence star, these magnitudes indicate that it is a late F-type or smaller mass star (Wainscoat et al., 1992).

4.5 Discussion

4.5.1 Implications for the System Parameters

It is likely that the compact object of MAXI J1305−704 is a black hole because the behavior of spectral evolution in the outburst is quite similar to those of typical BHXBs (Morihana et al., 2013). However, no constraint has been obtained so far on the black hole mass of this source, as well as its distance and the mass of the companion star. Here we summarize what we find about these system parameters from the *Suzaku* and *Swift* results.

The power spectrum obtained with the XIS light curve shows very weak intrinsic variability with a fractional rms^2 of $\sim 10^{-3}$ Hz^{-1} from 1×10^{-3} Hz to 5×10^{-2} Hz. This result suggests that the low-frequency break of the band-limited noise is located above the frequency range. Normally, BHXBs have an order of magnitude stronger power and the break frequency is much lower when they are in the low/hard state, although weaker variability is sometimes observed from low-mass black holes like GRO J1655−40 (5–7 $M_\odot$, Remillard et al. 1999) in that state. This might suggest that MAXI J1305−704 also have a relatively small mass black hole. However, even with a low-mass black hole it is difficult to explain the lack of the variability power for such a very hard spectrum with a photon index of ≈ 1.6.

Since the source shows dips but no eclipse, its inclination angle i is estimated to be $\approx 60°$–$75°$ (Frank et al., 1987). The dips seen in MAXI J1305−704 are deeper and more periodic than those in GRO J1655−40, whose inclination angle is $69^\circ.50 \pm 0^\circ.08$ (Orosz & Bailyn, 1997). This suggests that MAXI J1305−704 has a larger inclination angle than GRO J1655−40, likely $\approx 75°$, and that the complex dips originate in absorbing structures with small scale heights above the disk crossing the line of sight. From the *Suzaku* XIS light curve, the dip interval is estimated as 9.74 ± 0.04, which likely corresponds to the orbital period of MAXI J1305−704. We derive the binary size as $\approx 3 \times 10^6 M_{\rm tot4}^{1/3}$ km from Kepler's third law, where $M_{\rm tot4}$ represents the total mass of the companion star and the black hole in the unit of $4M_\odot$. Combining Kepler's third law and the relation between the radius and mass of the Roche lobe in a semi-detached binary system (Equation 4. in Paczyński, 1971), we have

$$\rho_{\rm c} = 30.375 \, \frac{\pi}{GP^2} \; (0 < M_{\rm c}/M_{\rm BH} < 0.8), \tag{4.1}$$

where $\rho_{\rm c}$, $M_{\rm c}$, and P represent the averaged density and mass of the companion star, which fills its Roche lobe, and the orbital period. From this equation, we derive the averaged density of the companion star as ≈ 1.2 g cm^{-3}, which is smaller than that of the Sun (≈ 1.4 g cm^{-3}). If the companion is a main sequence star, it has a slightly larger mass than the Sun. This is consistent with the near-infrared absolute magnitudes observed with *IRSF* in the low/hard state. However, an upper limit of the stellar radius is imposed by the inclination angle and binary size, $\approx 7 \times 10^5 \, (\cos i/\cos 75°) \, M_{\rm tot4}^{1/3}$ km, or $\approx 1 \, (\cos i/\cos 75°) \, M_{\rm tot4}^{1/3} \, R_\odot$, by considering that the source has no eclipses. This radius and the averaged density of the Roche lobe give a somewhat smaller mass of the companion star than that of the Sun, $< 0.9 \, (\cos i/\cos 75°)^3 \, M_{\rm tot4} \, M_\odot$, although this limit strongly depends on the assumed inclination angle and the total mass of the binary system. Thus, it is also possible that the companion is an evolved star with a mass of $\lesssim 1M_\odot$, instead of an earlier-type main sequence star than the Sun.

As presented in Fig. 4.9, the near-infrared and optical fluxes of MAXI J1305−704 in the high/soft state is $\approx$ 10 times higher than the flux level of the multicolor disk component, suggesting that the fluxes are dominated by other components, likely reprocessed emission from the irradiated outer disk and the black body emission from the companion star. To estimate the contributions of these two components to the optical and near-infrared spectral energy distribution (SED), we fit the *Swift*/XRT (X-ray), GROND (optical and near infrared), and *IRSF* (near-infrared) data in the high/soft state using the `diskir` (Gierliński et al., 2008, 2009) plus `bbodyrad` model, which represent the direct and reprocessed emission from the disk and the black body component from the companion star, respectively. The `diskir` model calculates the total spectrum of the disk emission and its Comptonization, including the reprocessed emission from the irradiated outer disk, by using the inner disk temperature ($kT_{\rm in}$), photon index and electron temperature of the Comptonized component (Γ and $kT_{\rm e}$, respectively), the ratio of the luminosity of the Compton tail to disk luminosity ($L_{\rm C}/L_{\rm d}$), the fraction of luminosity of the Comptonized component that is thermalized in the inner disk ($f_{\rm in}$), the fraction of bolometric flux that illuminates the outer disk ($f_{\rm out}$), the radius of the Compton illuminated disk ($r_{\rm irr}$), and the outer disk radius ($R_{\rm out}$). The `bbodyrad` model produces a black body spectrum from a temperature ($kT_{\rm BB}$) and a normalization ($K_{\rm BB}$), which is related to the source radius $R_{\rm BB}$ (km) and distance through $K_{\rm BB} = (R_{\rm BB}/D_{10})^2$, where D_{10} is the distance in units of 10 kpc.

We replace `diskbb` of the best-fit results of Model 4 in the *Swift*/XRT fit (Section 4.3.4) with `diskir` and add `bbodyrad` to fit the multi-wavelength SED. Here we set $f_{\rm in} = 0.1$ and $r_{\rm irr} = 1.1R_{\rm in}$ following Gierliński et al. (2009). The photon index of the Compton tail and the inner disk temperature are fixed at the same values of Model 4, $\Gamma = 2.2$ and $kT_{\rm in} = 0.88$ keV. The electron temperature of the Compton component is set to 300 keV in order not to have an exponential cut-off in the energy range of the *Swift*/XRT. After some trials of the spectral fit, we find that the black body component favors a small temperature and a large normalization. Considering the maximum radius constrained from the absence of eclipse, we vary the normalization of the `bbodyrad` component within $R_{\rm BB} < 1.0D_6\ R_\odot$.

Component	Parameter	Value
diskir	$kT_{\rm in}$ (keV)	0.88 (fix)
	Γ	2.2 (fix)
	$kT_{\rm e}$ (keV)	300 (fix)
	$L_{\rm C}/L_{\rm d}$	0.10 ± 0.02
	$f_{\rm in}$	0.1 (fix)
	$r_{\rm irr}$ ($R_{\rm in}$)	1.1 (fix)
	$f_{\rm out}$	$4.4^{+0.05}_{-0.04} \times 10^{-3}$
	$\log_{10}(R_{\rm out}/R_{\rm in})$	$5.15^{+0.4}_{-0.5}$
	Norm	137 ± 1
bbodyrad	$T_{\rm BB}$ (K)	4200^{+1400}_{-1200}
	$R_{\rm BB}$ ($R_\odot$/6 kpc)	$1.0^{+0,\ \rm pegged}_{-0.2}$
χ^2/d.o.f		415/377

Table 4.4: Best-fit results from the simultaneous fit of the X-ray, optical, and near-infrared data of the *Swift*/XRT, GROND, and *IRSF*.

Notes. The model is `phabs*(xsabs*xsabs*diskir+bbodyrad+gauss+gauss)`. The parameters of neutral and ionized absorptions (`phabs` and `xsabs`, respectively) and two Gaussians are set to the best-fit values of Model 4 in the *Swift*/XRT spectral fit (Table 4.2).

The best-fit parameters of the `diskir` and `bbodyrad` models are listed in Table 4.4. The optical and near-infrared SED in the high/soft state is reproduced reasonably well with the dominant irradiated disk component and the weak black body component from the companion star (Figure 4.10). The irradiation fraction ($f_{\rm out} \approx 4 \times 10^{-3}$) is $\approx$ 10 times smaller than those of GX 339−4 and GRS 1915+105 during the high/soft state (Rahoui et al., 2010, 2012), but $\approx$ 5 times larger than those of XTE J1817−330 in that state (Gierliński et al., 2009). The radius of the companion star is estimated as $R_{\rm BB} > 0.8 D_6\ R_\odot$ and the temperature is found to be smaller than that of the Sun (3000 K $< T_{\rm BB} <$ 5600 K). These results and the averaged density estimated from Equation (4.1) suggest that the companion is likely an evolved star at an early stage that has a smaller mass than $\approx 1 M_\odot$.

We find that the non-dip spectra in the *Swift* and *Suzaku* observations have comparable bolometric luminosities within a factor of 3. This suggests that they are likely to be only a few times more and less than that in the soft-to-hard transition, $\approx 0.02 L_{\rm Edd}$, respectively, by considering the results of Maccarone (2003). However, the inner disk temperature of the `diskbb` component obtained from the *Swift* spectrum ($\approx$ 1.0 keV) is

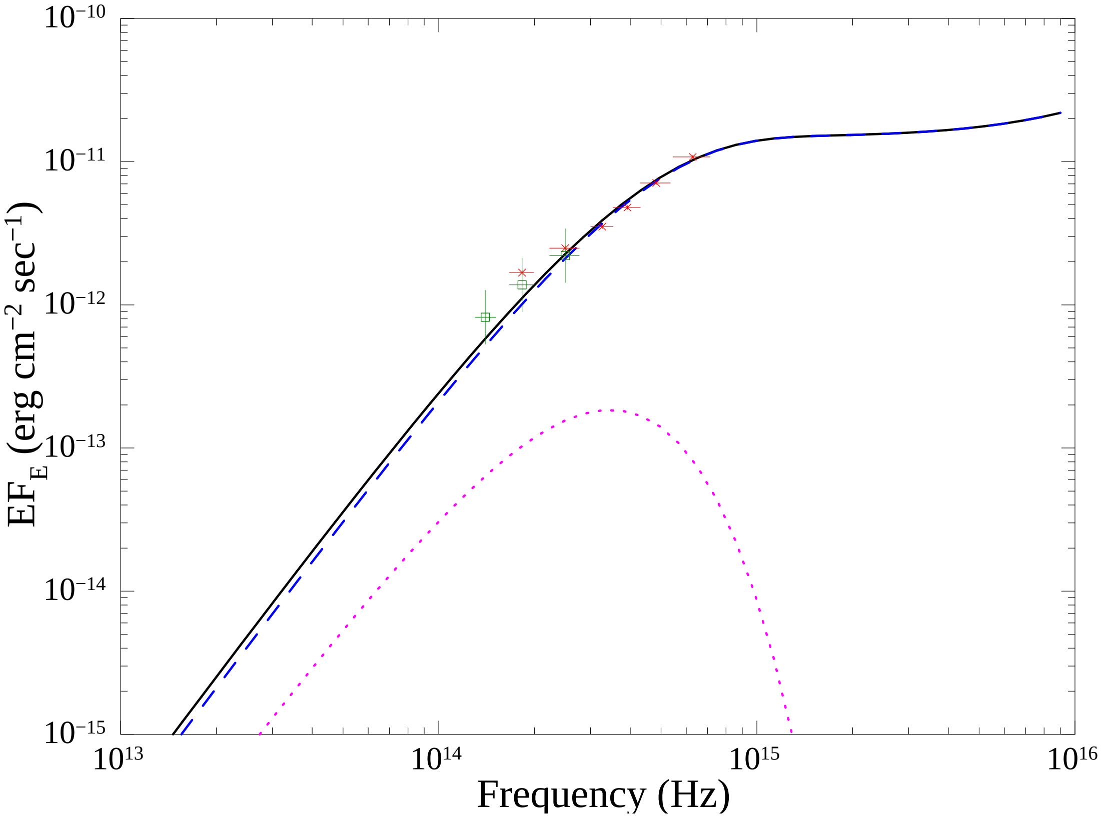

Figure 4.10: The best-fit `diskir+bbodyrad` spectrum in the optical and near-infrared bands. The contributions of `diskir` (blue, dashed) and black body (pink, dotted) components are separately displayed. The GROND fluxes obtained on April 11 (red, cross) and *IRSF* fluxes on April 29 (green, open square) are overplotted.

much higher than what we expect from a faint high/soft state for normal BHXBs. This suggests that the disk spectrum is significantly modified by the Doppler effects due to a very high inclination angle, probably ≈ 75°. Indeed, assuming a black hole mass of $3M_\odot$, a bolometric luminosity of $0.05L_{\rm Edd}$, and an inclination angle of 75°, we successfully reproduce the *Swift* spectrum with a relativistic disk emission model (`bhspec`), and obtain a moderate spin ($a = 0.46 \pm 0.06$) and a distance of $6.3^{+0.4}_{-0.3}$ kpc calculated from the normalization ($2.5^{+0.3}_{-0.2}$). We note that there is strong coupling between the spin, luminosity, and black hole mass in the `bhspec` fit and a smaller spin parameter is obtained when a larger luminosity and/or a lower black hole mass is assumed. For instance, in the cases of $L_{\rm X} = 0.1L_{\rm Edd}$ and $0.01L_{\rm Edd}$, we have $a < 0.16$ and 0.90 ± 0.02, while $M_{\rm BH} = 5M_\odot$ and $10M_\odot$ give $a = 0.63^{+0.05}_{-0.04}$ and 0.80 ± 0.03, respectively.

4.5.2 Dipping Behavior

The *Suzaku* observation revealed that MAXI J1305−704 has two separate periodic dips with different column densities, ionization parameters, and covering fractions of the absorbers. We find that these dips have the same recurrence period of 9.74 ± 0.04 hours and the harder dip (deep dip) is followed by the softer dip (shallow dip) in 6.38 hours. Such strong, softer "secondary dips" are occasionally seen in dipping X-ray binaries (a few neutron star binaries like XB 1916−053; Smale et al. 1992). Dips are generally interpreted as the absorption by the "bulge" formed in a region where the accretion stream from the companion star impacts the outer boundary of the disk, but what is the origin of a secondary dip? It may be the result of the accretion stream hitting the disk again and splashing at its circularization radius, which is smaller than the outer disk radius (Frank et al., 1987, 1992). Frank et al. (1987) suggest that the stream causes ionization instabilities at the second impact and creates patchy cold clouds within a hot medium. This is consistent with the behavior of the shallow dip, in which significant time variabilities can be seen in the XIS light curve. The shallow dip occurs at the orbital phase of ≈ 0.64 (if the start of the deep dip is assumed to be phase 0), which is also consistent with the picture of Frank et al. (1987).

The properties of time variabilities and absorption profiles in the dipping spectra provide us with key information on the two dips. The shallow dip exhibits significant fast variabilities on the timescale of a few minutes in the XIS light curve, suggesting that the absorber is not a single continuous structure but is composed of blobs.

If the absorber of the shallow dip is created at the circularization radius of 10^6 km and rotates with the Keplerian velocity, one minute corresponds to a typical blob size of $\approx 4 \times 10^4 M_3^{1/2}$ km, where M_3 is defined as $M_{\rm BH}/3M_\odot$. The covering fraction $0.72^{+0.03}_{-0.04}$ in the shallow dip can be understood as the filling factor of blobs in the dipping zone. Interestingly, similar short-time variability was also found in the neutron star XB 1254−690 (Díaz Trigo et al., 2009), suggesting that shallow dips in dipping X-ray binaries may generally consist of clumps. By contrast, in the deep dip, short-time variabilities are not significant and the covering fraction is larger than 90%, suggesting that the absorber of the deep dip has more continuous structure or is filled with much smaller blobs than those of the shallow dip.

We have shown that both non-dip and dip spectra of MAXI J1305−704 obtained with *Suzaku* are successfully modeled by ionized absorbers with different column densities and ionization parameters. The dip spectra have an order of magnitude larger hydrogen column densities and smaller ionization parameters than those of the non-dip spectrum. These results are very similar to those reported by Boirin et al. (2005) and Díaz Trigo et al. (2006) for neutron star low mass X-ray binaries. Thus, it may be a general picture in low-mass X-ray binaries that dips are created by ionized absorbers with much larger column densities and in lower ionization states than those observed in non-dip spectra.

4.5.3 Structure of Accretion Disk and Comptonized Corona

The *Suzaku* non-dip spectrum of MAXI J1305−704 is approximated by a power-law extending up to 130 keV with a photon index of ≈1.6. This hard spectrum indicates that the source was in the low/hard state. By more detailed modeling, we find that the spectrum can be described with a general model in the low/hard state of BHXBs (e.g., Gierliński et al., 1997), a MCD and its Comptonization with a reflection component from the disk. Although recent *Suzaku* studies on other BHXBs report that two Comptonization components with different optical depths are needed to reproduce their spectra in the low/hard state (Takahashi et al. 2008; Makishima et al. 2008; Shidatsu et al. 2011b; Yamada et al. 2013a), our data do not require the second component. The reason is unclear, but it may be because the large inclination of MAXI J1305−704 makes it difficult to detect the softer component (i.e., with a small optical depth) than the other systems, although it may be partially due to the poor statistics of our data.

The smooth spectral profile of MAXI J1305−704 without any complex Comptonized component required, as well as the relatively weak time variability below 5×10^{-2} Hz (see Section 4.5.1), are unusual and interesting properties for a BHXB in the low/hard state.

We obtained a much larger normalization ($6.0^{+3.4}_{-2.4} \times 10^{3}$) and smaller temperature ($0.168^{+0.008}_{-0.006}$ keV) of the direct MCD component than those obtained with the *Swift*/XRT spectrum in the high/soft state. The flux of the `nthcomp` component is estimated as 0.180 photons $\mathrm{cm}^{-2}\ \mathrm{sec}^{-1}$ and that of diskbb component as 0.394 photons $\mathrm{cm}^{-2}\ \mathrm{sec}^{-1}$. Using Equation (3.1) in Chapter 3, we calculate the innermost disk radius of $r_{\mathrm{in}} = 93^{+7}_{-5} D_6 (\cos i / \cos 75°)^{-1/2}$ km, (where D_6 is the distance in unit of 6 kpc). The actual radius is derived to be $R_{\mathrm{in}} = 111^{+8}_{-6} D_6 (\cos i / \cos 75°)^{-1/2}$ km, by multiplying 1.19, a correction factor of the boundary condition and spectral hardening (Kubota et al., 1998).

We compare the inner disk radius in the *Suzaku* and *Swift* observations, using the intrinsic flux of the MCD component. Although the absolute radius obtained from the *Swift* result may be affected by the strong beaming effects, we are able to discuss the relative difference of the radius between the two epochs. Using the `diskbb` normalization obtained with the XRT spectrum (139^{+26}_{-45}) and multiplying the correction factor 1.19 (Kubota et al., 1998), we derive the inner disk radius as $16.5^{+1.5}_{-2.9} D_6$ $(\cos i / \cos 75°)^{-1/2}$ km. Thus, the inner radius obtained from the best-fit model of *Suzaku* data, $111^{+8}_{-6} D_6 (\cos i / \cos 75°)^{-1/2}$ km is 5.8–8.8 times larger than that from the XRT result. Thus, we robustly conclude that the inner radius increased in the *Suzaku* observation, giving strong evidence for disk truncation in the low/hard state.

We find significant broad emission-line like residuals at ≈0.7 keV and ≈1.2 keV in the *Swift*/XRT spectrum, which cannot be reduced by multiple ionized absorptions, partial covering, or emission components from the absorber itself. Also, these residuals are not completely explained by changing the elemental abundances in the neutral and ionized absorbers. It is difficult to know what makes these structures. Because they are not seen in the Suzaku spectra in the low/hard state, their origin would be associated with the geometry of the accretion disk and/or the ionized absorbers in the high/soft state.

Similar features at ≈0.7 keV were reported in several ultracompact low mass X-ray binaries (UCXBs; e.g., Juett et al., 2001), which have very short orbital periods (less than about 80 minutes). Madej et al. (2010) and Madej & Jonker (2011) recently suggested that the structures seen in UCXBs are the relativistically broadened OVIII Lyα line created by reflection on the disk in the vicinity of the accretor with an ionization parameter of $\log\xi \approx 2.3$. Likewise, the residuals in MAXI J1305−704 might originate from reflection on an ionized accretion disk in the strong gravitational field created by the central black hole. Indeed, we find that a relativistic emission line model `laor` instead of a Gaussian model can also give an acceptable fit (χ^2/d.o.f. = 297/360) by assuming an inclination of 75°, an inner radius of $4R_{\rm g}$ (corresponding to $a \approx 0.5$), an outer radius of $400R_{\rm g}$, and an emissivity index (β). The resulting line energy and equivalent width of the `laor` model are 0.66 ± 0.01 keV and 194 eV for the lower energy feature and 1.03 ± 0.02 keV and 83 eV for the higher energy feature (here we vary the emissivity index within $2 \leq \beta \leq 3$ and obtain the best-fit value of $\beta = 2.4 \pm 0.1$). These line energies are consistent with the Kα line from H-like oxygen ions and L-lines from ionized iron ions. The photons to illuminate the disk would be produced from the Comptonizing corona, or from the disk itself whose emission could be partially incident on the disk because of gravitational light bending. If these photons could strongly illuminate the disk, huge emission lines might arise through a temperature inversion region of the irradiated disk atmosphere. The large equivalent width of the emission lines with respect to the continuum emission would be expected for a very high inclination source because of a large optical depth of the disk atmosphere. However, we have no model to accurately evaluate these effects at present. Radiative transfer calculation, including all these possible effects, is left for future studies.

4.5.4 Ionized Absorbers

We find that not only the *Swift*/XRT spectrum in the high/soft state but also the *Suzaku* spectrum in the low/hard state exhibit ionized absorption features. Blue shifts are not significantly detected with upper limits of 2300–5800 km s^{-1}. The absorber of the *Suzaku* non-dip spectrum has a column density of $N_{\rm H} = 6.1^{+1.0}_{-0.9} \times 10^{21}$ cm^{-2} and an ionization parameter of $\log\xi = 2.19 \pm 0.04$, while the *Swift*/XRT spectrum requires two ionized absorbers with different parameters, $N_{\rm H} = 5.1^{+3.8}_{-2.8} \times 10^{22}$ cm^{-2} and $\log\xi = 2.86^{+0.52}_{-0.18}$ for one, and $N_{\rm H} = (1.0^{+0.4}_{-0.3}) \times 10^{22}$ cm^{-2} and $\log\xi = 1.2 \pm 0.2$ for the other. As discussed in Section 4.5.2, the dip spectra of *Suzaku* are also described with ionized absorbers but with much larger column densities and lower ionization parameters, $N_{\rm H} = (1.44 \pm 0.06) \times 10^{23}$ cm^{-2} and $\log\xi = 1.90 \pm 0.07$ for the deep dip, and $N_{\rm H} = 6.6^{+0.5}_{-0.4} \times 10^{22}$ cm^{-2} and $\log\xi = 1.79 \pm 0.07$ for the shallow dip.

To investigate the origin of the ionized absorbers, we estimate their distances from the X-ray source (R) from the definition of the ionization parameter (see Equation 1.7 in Chapter 1). Here $L_{\rm X}$ is the incident luminosity, whose energy range is 1–1000 Ry in the definition of XSTAR. $L_{\rm X}$ is estimated as $1.3 \times 10^{36} D_6^2$ erg sec^{-1} for the *Suzaku* observation, and $8.1 \times 10^{36} D_6^2$ erg sec^{-1} for the *Swift* observation. Assuming $\Delta R/R = 1$, we obtain $R \approx 1.4 \times 10^7$ km for the absorber seen in the *Suzaku* non-dip spectrum. For the *Swift*/XRT data, we estimate $R \approx 2.2 \times 10^6$ km for the absorber with a higher ionization state and $R \approx 5.1 \times 10^8$ km for the absorber with a lower ionization state. All these radii are more than an order of magnitude larger than predicted values for thermally driven disk winds in BHXBs ($R \sim 10^5$ km; e.g., Begelman et al. 1983; Woods et al. 1996; also see below). Furthermore, they are comparable to or even larger than the binary size (see Section 4.5.1). Hence, if the ionized absorbers of MAXI J1305−704 are located on the disk, $\Delta R/R$ should be much less than 1. This suggests that the absorbers are originated from rather compact structures and do not largely extend in the radial direction. The absorbers in the deep and shallow dips are calculated to be $R \approx 1.1 \times 10^6$ km and $R \approx 3.2 \times 10^6$ km, respectively, which are comparable to those seen in the *Suzaku* and *Swift*/XRT non-dip spectra.

Table 4.5 summarizes the physical properties of ionized absorbers reported in previous studies of black hole or neutron star X-ray binaries. The ionization parameter, column density, Doppler velocity, and luminosity taken from the literature are listed. We then calculate the apparent distance R by assuming $\Delta R/R = 1$ for each set of parameters. Although there is considerable variety in each parameter, almost all of the absorbers in the BHXBs are found to be outflowing with a velocity of 100–1000 km sec^{-1}. Typically, they are located at $R \sim 10^4$–10^5 km when $\Delta R \sim R$ is assumed. They are interpreted as thermally (e.g., Kubota et al., 2007), radiatively (Kotani et al., 2000), or magnetically driven disk winds (Miller et al., 2008). By contrast, ionized absorbers in neutron star low mass X-ray binaries do not often exhibit significant blue shifts, except for some sources such as GX 13+1 (Ueda et al., 2004) and Cir X-1 (Schulz et al., 2008), which are known to have powerful outflows. This implies that the photoionized plasma on neutron star dippers remain gravitationally bound to the system as disk atmosphere and is not outflowing due to a small system size and a low luminosity of the central X-ray source (see Díaz Trigo & Boirin, 2013).

From the comparison, we find that MAXI J1305−704 has somewhat lower ionization parameters ($\log \xi < 3$) and consequently larger R than those of typical disk winds observed in other BHXBs. By contrast, absorbers in neutron star dippers sometimes have similar R values (see the table of XB 1916−053 and EXO 0748−676) and exhibit complex and deep dips like MAXI J1305−704. Although the BHXB GRO J1655−40 shows a similar value of R (4×10^6 km and 1.3×10^7 km) based on the results by Díaz Trigo et al. (2007), the turbulent velocity ($v_{\rm turb}$) adopted there is much higher than that assumed for MAXI J1305−704 in this chapter. We have to note that a larger $v_{\rm turb}$ value gives a smaller column density; in the case of 4U 1630−47, about 10 times larger values of $N_{\rm H}$ was obtained with $v_{\rm turb} = 2000$ km sec^{-1} than that with $v_{\rm turb} = 100$ km sec^{-1} (Kubota et al., 2007). If we assumed $v_{\rm turb} \sim 5000$ km sec^{-1}, the R values of the MAXI J1305−704 would become much larger than those of GRO J1655−40. The BHXB GRS 1915+105 also shows a large apparent distance ($R \approx 10^6$ km), but its binary size is very large ($\sim 10^8$ km) as the source has a very long (33.5 ± 1.5 days; Greiner et al. 2001) orbital period and contains a massive black hole ($\approx 15 M_\odot$). Thus, the distance of the ionized absorber in GRS 1915+105 would be well within the size of accretion disk, even if $R \sim \Delta R$ is assumed. Figure 4.11 plots the values of $N_{\rm H}$ and R for the ionized absorbers in MAXI J1305−704 and those in other BHXBs that exhibit dips and have turbulent velocities less than 1000 km sec^{-1}, except for GRS 1915+105. The absorbers in MAXI J1305−704 have large R values and comparable or smaller $N_{\rm H}$ values compared to those in the other sources.

These properties suggest that the absorbers in MAXI J1305−704 are originated from compact structures like those responsible for the dips, rather than a typical disk wind, which would be widely extended in the radial direction (i.e., $\Delta R/R \sim 1$). The *Suzaku* light curve in the soft band exhibits significant time variability even in the non-dip phases on the shorter time scale than the orbital period. We find these small variabilities occur almost recurrently as well as the deep and shallow dips, by folding the Suzaku light curve with the orbital period. This fact would support the idea that the ionized absorbers in MAXI J1305−704 are associated with the disk and composed of compact clouds, unlike disk winds observed in other BHXBs that distribute quite homogeneously over the orbital phase (Yamaoka et al., 2001). Miller et al. (2014a) have

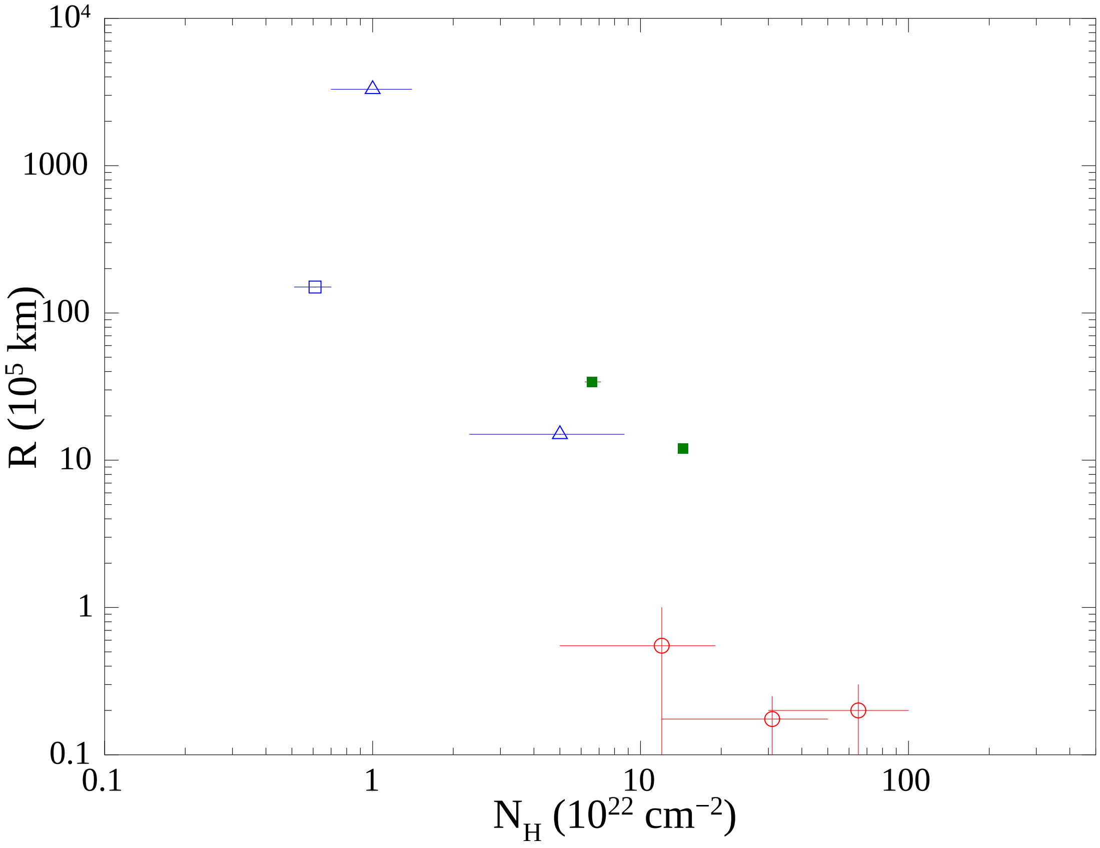

Figure 4.11: $N_{\rm H}$ vs. R for ionized absorbers in persistent spectra of MAXI J1305−704 (blue) in the high/soft state (open triangle) and low/hard state (open square) and other BHXBs that exhibit dips (red circle), except for GRS 1915+105, taken from Table 4.5. Only the absorbers whose turbulent velocities are less than 1000 km sec^{-1} are plotted. The absorbers of MAXI J1305−704 in the dipping periods are also plotted (green, filled square).

recently obtained a very large number density ($n_{\rm H} \approx 10^{17}$ cm^{-3}) from density-sensitive absorption lines seen in the high-resolution *Chandra*/HETG spectrum of the source in the high/soft state and derived the actual distance of the absorber as $\approx 4 \times 10^3$ km utilizing the density without any assumption of $\Delta R/R$. From the distance and density, we can estimate the size of ionized absorber as $\Delta R \approx 1$ km. This strongly indicates that the absorbers are composed of small clumps.

A possibility is that a fraction of the absorbing gas responsible for the dips is spread to the non-dip phases. MAXI J1305−704 is likely to be a high inclination system even compared with other dipping BHXBs and we may see many complex structures of the absorbing gas with a small scale height on the surface of the accretion disk. As described in Frank et al. (1987), the short orbital period of MAXI J1305−704 may maintain the clumpy absorbers and produce the similarity in the properties of the ionized absorbers seen in neutron star binaries. Also, like neutron star dippers, the disk size of MAXI J1305−704 ($\lesssim 10^6 M_4^{1/3}$ km), estimated from the binary size, is comparable with or maybe smaller than the Compton radius ($\sim 4 \times 10^5\ T_{\rm IC8}^{-1}\ M_4$ km, where $T_{\rm IC8}$ is the Compton temperature in units of 10^8 K) and would not be sufficiently large to power a thermal-driven disk wind (see Díaz Trigo & Boirin, 2013). However, there remains a possibility that we are seeing the launching site of the disk wind near the outer edge of the disk, which may be less homogeneous than in its outer parts and can be compact ($\Delta R/R < 1$). If this were the case, our *Suzaku* result would imply that such a disk wind exists in the low/hard state of a BHXB and that the accretion states do not always determine the presence of disk winds. Future studies using high quality and high-resolution spectra, like those obtained by *ASTRO-H* (Takahashi et al., 2012), should provide important clues to reveal the origin of these ionized absorbers in X-ray binaries (see Chapter 5).

Source name	photon index or State	distance (kpc)	orbital period (h)	$N_{\rm H}$ (10^{22} cm^{-2})	$\log \xi$	$L_{\rm X}$ (erg sec^{-1})	energy band of $L_{\rm X}$ (keV)	R (10^5 km)	$v_{\rm outflow}$ (km s^{-1})	$v_{\rm turb}$ (km s^{-1})	Reference
XB 1916−053	2.25 ± 0.03	9.3	0.8 h	4.2 ± 0.5	3.05 ± 0.04	4.4×10^{36}	0.6–10	9.3	-[l]	2300^{+2100}_{-1700}	Díaz Trigo et al. (2006)
4U 1254−690	2.09 ± 0.02	10	5.8 h	8.4 ± 0.3	4.3 ± 0.1	1.04×10^{37}	0.6–10	0.62	-[l]	2800 ± 1900	Díaz Trigo et al. (2006)
MXB 1659−298	1.96 ± 0.03	15	7.1 h	11.1 ± 0.6	3.8 ± 0.1	3.44×10^{37}	0.6–10	4.9	-[l]	700^{+1000}_{-350}	Díaz Trigo et al. (2006)
EXO 0748−676	1.57 ± 0.05	10	3.8 h	3.5 ± 0.2	2.45 ± 0.02	3.4×10^{36}	0.6–10	34	-[l]	13 ± 6	Díaz Trigo et al. (2006)
XB 1323−619	$1.90^{+0.06}_{-0.10}$	10	2.9 h	$3.6^{+1.0}_{-0.9}$	$3.90^{+0.08}_{-0.09}$	5.2×10^{36}	0.6–10	1.8	-[l]	1700 ± 1000	Boirin et al. (2005)
X 1624−490	2.25	$15^{+2.9}_{-2.6}$	21 h	20 ± 10	4.3 ± 0.4	4.9×10^{37}	1–10	1.2	607^{+354}_{-342}	280^{+180}_{-80}	Xiang et al. (2009)
				$1.3^{+0.3}_{-0.5}$	3.3 ± 0.2			190	-213^{+108}_{-158}	< 174	
GX 13+1	MCD dominant	7 ± 1	24 day[c]	10–100	4.2–4.5	1×10^{38}	full[i]	1–10	460 ± 70	490^{+110}_{-140}	Ueda et al. (2004)
IGR J17480−2446	1.26	5.5	21 h[d]	3[g]	3[g]	$(3.7 \pm 0.2) \times 10^{37}$	0.5–10	123	3100	4800 ± 900[m]	Miller et al. (2011)
				2[h]	4.3[h]			9	500	< 600[m]	
Cir X-1	$0.38^{+0.29}_{-0.19}$	6	16.6 day	80 ± 20	$1.6^{+0.4}_{-0.2}$	1.4×10^{36}	2–10	4.3	2300^{+840}_{-1400}	300 (fixed)	Schulz et al. (2008)
	2.62 ± 0.12			6 ± 1	$2.7^{+0.1}_{-0.2}$	9.9×10^{36}	2–10	33	570^{+670}_{-630}	300 (fixed)	
4U 1630−47	high/soft state	10	unknown	5–19	4.38–4.88	2.8×10^{38}	full[i]	0.1–1	(−120)–1740	500 (fixed)	Kubota et al. (2007)
H 1743−32[a]	high/soft state	8.5	unknown	≈ 5	5.7	6.8×10^{38}	0.5–10	0.01–1	670 ± 170[i]	1800 ± 400[l]	Miller et al. (2006c)
GRO J1655−40	high/soft state	3	2.6 day	30–100	3	1×10^{36}	9–∞	0.1–0.3	-[l]	< 130[h]	Ueda et al. (1998)
GRO J1655−40	high/soft state	3.2		5.2 ± 1.0	3.60 ± 0.04	8×10^{37}	0.5–200	40	540 ± 120	3500 ± 900	Díaz Trigo et al. (2007)
				1.5 ± 1.2	3.30 ± 0.04	4×10^{37}		130		5900 ± 1200	
GRO J1655−40	high/soft state	3.2		12–50	4.8–5.7	5×10^{37}	0.65–10	0.1–0.25	300–1600	300 (fixed)	Miller et al. (2008)
GRS 1915+105	"low/hard" state	12.5	33.5 ± 1.5 day[e]	≈ 1	≈ 3.8	4×10^{38}	2–10	≈ 10	≈ 1000	740[h] (fixed)	Kotani et al. (2000)
GRS 1915+105	"low/hard" state	12.5		≈ 3	$\lesssim 4.15$	6.4×10^{38}	full[i]	$\lesssim 20$[j]	700 ± 400[i]	578 ± 400[h]	Lee et al. (2002)
GRS 1915+105	high/soft state	12		≈ 10	4.2–4.3	(6.6–8.3) $\times 10^{38}$	0.01–100	2–6	90–560	70–200	Ueda et al. (2009)
GX 339−4	intermediate state[b]	5	1.76 day[f]	0.02	≈ 3	$\approx 1 \times 10^{37}$	0.5–10	20[k]	510[n]	410[n]	Miller et al. (2004)
MAXI J1305−704	high/soft state	6	9.74 ± 0.04 h	$5.1^{+3.8}_{-2.8}$	$2.86^{+0.52}_{-0.18}$	8.1×10^{36}	0.0136–13.6	22	< 4800	300 (fixed)	This work
MAXI J1305−704	high/soft state			$1.0^{+0.4}_{-0.3}$	1.2 ± 0.2			5.1×10^3	0 (fixed)	300 (fixed)	
MAXI J1305−704	low/hard state										
	(non-dip)			$0.61^{+0.09}_{-0.10}$	2.18 ± 0.04	1.3×10^{36}		140	< 2300	300 (fixed)	This work
MAXI J1305−704	(deep dip)			14.4 ± 0.6	1.90 ± 0.07			11	< 2700	300 (fixed)	
MAXI J1305−704	(shallow dip)			$6.6^{+0.5}_{-0.4}$	1.79 ± 0.07			32	< 5800	300 (fixed)	

Table 4.5: Properties of ionized absorbers in X-ray binaries.

[a] Observation 1 in Miller et al. (2006c).

[b] In the soft-to-hard transition.

[c] Corbet et al. (2010).

[d] Papitto et al. (2011).

[e] Greiner et al. (2001).

[f] Hynes et al. (2003).

[g] Estimated from the Fe XXV absorption line.

[h] Estimated from the Fe XXVI absorption line.

[i] Bolometric luminosity.

[j] $\Delta R/R \approx 0.1$.

[k] Calculated by assuming the thickness and number density of the absorber as 20 km and 8×10^{13} cm^{-3}, respectively.

[l] Not constrained.

[m] The line width when the Gaussian model is applied.

[n] The results of the Ne II line at 14.631 Å, from which the largest blue shift is obtained.

Notes. R is calculated from $L_{\rm X}/\xi N_{\rm H}$ by assuming $\Delta R = R$, unless otherwise stated. The positive values of $v_{\rm outflow}$ indicate blue shifts. The distances represent the assumed values that are used to estimate $L_{\rm X}$. 4U 1630−47 and the following sources are BHXBs. The results in the non-dip phases are shown for the top 6 sources (dippers).

5

Concluding Remarks

5.1 Summary

BHXBs are ideal objects to understand the fundamental physics in the vicinity of black holes, including gravitational effects, accretion and ejection processes, over wide rage of mass accretion rates. In this thesis, we studied the structure of the accretion flow and disk winds in the high/soft and low/hard states, using *Suzaku* and *Swift* X-ray data of H 1743−322 and MAXI J1305−704 obtained during their outbursts in 2012. We analyzed the light curves and performed detailed spectral modeling for the two sources. For H 1743−322, located in close proximity to the Galactic center, we found the observed X-ray spectra are significantly affected by dust scattering in the interstellar medium with $N_{\mathrm{H}} \approx 2 \times 10^{22}$ cm^{-2}. To accurately analyze the X-ray spectra, we appropriately corrected for this effect, which has been ignored in previous X-ray studies of this source.

All the time-averaged low/hard state spectra of the two sources were well described by a model consisting of the standard disk emission, its Comptonization, and the reflection on the disk. In all cases, the Compton-scattered component dominated the X-ray flux. The electron temperature of the Comptonized corona in H 1743−322 was successfully estimated to be ≈60 keV, while that in MAXI J1305−704 was not constrained. A weak low-frequency QPO was detected at 0.1–0.2 Hz in the power density spectra of H 1743−322. We found that the QPO frequency becomes lower as the X-ray luminosity and photon index decrease. A possible explanation of this behavior is that the low-frequency QPO is produced by the Lense-Thirring precession of hot inner flow, and that the inner edge of the disk, which determines the precession frequency, recedes as the mass accretion rate declines.

The inner disk radius in the low/hard state, estimated from the intrinsic disk flux including the Compton-scattered photons, was always larger than that in the high/soft state. This supports the disk truncation model, in which the standard disk does not extend to the ISCO in the low/hard state. We also estimated the cool disk component by investigating short-term spectral variability on the ∼1-sec timescale, independently of the time-averaged spectral modeling. We found that the spectral ratio between high- and low-intensity phases has a very similar shape to those of Cyg X-1 in the low/hard state, indicating the presence of stable disk emission at low energies.

We detected ionized absorption structures in MAXI J1305−704, both in the high/soft and low/hard states. The absorbers were found to have much smaller ionized parameters and column densities than those of typical disk winds seen in other BHXBs. The properties of the absorbing gas were rather similar to the deeply-dipping neutron star X-ray binaries. These results suggest that the absorbers have compact and clumpy structures like those responsible for the dips rather than an extended, homogeneous disk wind. The possibility that we were seeing the launching site of a disk wind is not ruled out, however. Thus, we do not reach any conclusion about whether the normal, extended disk winds are present in the low/hard state. Instead, we have revealed that there is another type of ionized absorber with different properties from those of the normal disk winds. Future observations with high-energy-resolution instruments, like the micro-calorimeter on *ASTRO-H*, may provide important clues for the origin of the absorbers (see below).

5.2 Prospects for Future Studies with *ASTRO-H*

The next Japanese satellite *ASTRO-H* (Takahashi et al., 2012, also see Figure 5.1), following *Suzaku*, has been developed in collaboration with NASA, ESA (European Space Agency), and some Western countries (Takahashi et al., 2012). It is scheduled to launch in the financial year of 2015. *ASTRO-H* has four scientific instruments. In particular, the X-ray micro-calorimeter, named the Soft X-ray Spectrometer (SXS), is powerful to investigate the detailed profiles of X-ray absorption and emission lines. It achieves an energy resolution of ≈7 eV below 10 keV. This unprecedented energy

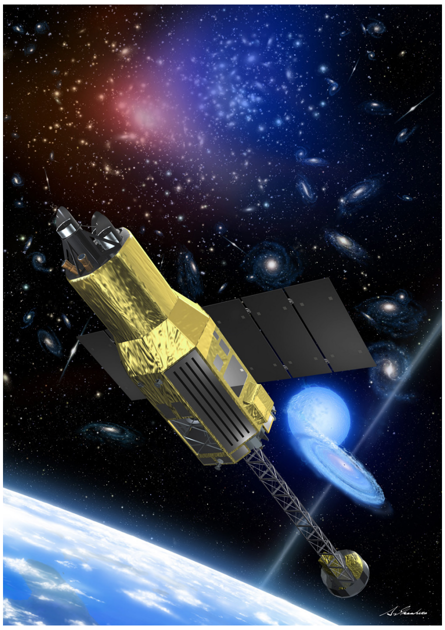

Figure 5.1: Image of *ASTRO-H*, taken from the *ASTRO-H* official webpage, http://astro-h.isas.jaxa.jp/ .

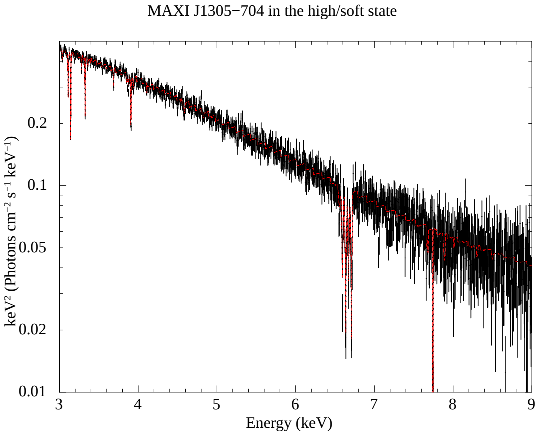

Figure 5.2: A simulated 40 ksec *ASTRO-H*/SXS spectrum of the ionized absorber in MAXI J1305−704 in the high/soft state, based on the *Swift*/XRT results (see Chapter 4). The best-fit *Swift*/XRT model is shown in red. The velocity of the absorber is assumed as 0 km sec^{-1}.

resolution, as well as good sensitivity at around 6 keV, will enable us to resolve the iron-K absorption lines from disk winds in BHXBs and to determine their physical properties (including velocity, density, ionization level) and geometry (see Miller et al., 2014b). It can also provide key information on the origin of the unusual ionized absorbers observed in MAXI J1305−704. Such absorbers may have small velocity that cannot be detected with the energy resolutions of X-ray CCDs. Figure 5.2 plots a simulated *ASTRO-H*/SXS spectrum of the ionized absorber observed in MAXI J1305−704, where the velocity is assumed as 0 km sec^{-1}. With a 40 ksec observation, the absorption lines are resolved and the velocity will be precisely measured with a 90% statistical error of less than ≈30 km sec^{-1}.

ASTRO-H carries hard X-ray and soft Gamma-ray instruments, called Hard X-ray Imager (HXI) and Soft Gamma-ray Detector (SGD), which achieve more than an order of magnitude higher sensitivity than the *Suzaku*/HXD above ∼10 keV. By combining SGD, HXI, SXS and the X-ray CCD camera "Soft X-ray Imager (SXI)", *ASTRO-H* is capable of observing BHXBs in a wide energy range (0.2–600 keV) with excellent sensitivity. High-quality broad-band spectra of BHXBs obtained with *ASTRO-H* will enable us to reveal the structure of the hot corona in the faint low/hard state and to study fast time variabilities of continuum spectra like QPOs and shots at the initial phase of outbursts. In this regard, all-sky X-ray monitoring with *MAXI* (which is expected to keep operating in the *ASTRO-H* era) would play a critical role to perform *ASTRO-H* observations of transient BHXBs at the appropriate time.

References

Anders, E., & Grevesse, N. 1989, Geochim. Cosmochim. Acta, 53, 197 24

Axelsson, M., Borgonovo, L., & Larsson, S. 2005, A&A, 438, 999 13, 14

Axelsson, M., Done, C., & Hjalmarsdotter, L. 2014, MNRAS, 438, 657 13, 62

Baba D., Nagata T., Iwata I., Kato, T. & Yamaoka, H. 2003, IAU Circ., 8112, 2 36

Balucinska-Church, M., & McCammon D. 1992, ApJ, 400, 699 45

Barthelmy, S. D., Barbier, L. M., Cummings, J. R., et al. 2005, Space Sci. Rev., 120, 143 30

Baumgartner, W. H., Tueller, J., Markwardt, C. B., Skinner, G. K., Barthelmy, S., Mushotzky, R. F., Evans, P. A., & Gehrels, N. 2013, ApJS, 207, 19 39

Beer, M. E., & Podsiadlowski, P. 2002, MNRAS, 331, 351

Begelman, M. C., McKee, C. F., & Shields, G. A. 1983, ApJ, 271, 70 15, 16, 97

Belloni, T., & Hasinger, G. 1990, A&A, 227, L33 13

Belloni, T., Psaltis, D., & van der Klis, M. 2002, ApJ, 572, 392 13

Belloni, T., Homan, J., Casella, P., van der Klis, M., Nespoli, E., Lewin, W. H. G., Miller, J. M., & Méndez, M. 2005, A&A, 440, 207 7

Benford, G. 1978, MNRAS, 183, 29 18

Blandford, R. D., & Königl, A. 1979, ApJ, 232, 34 18

Blandford, R. D., & Payne, D. G. 1982, MNRAS, 199, 883 18

Blum, J. L., Miller, J. M., Cackett, E., Yamaoka, K., Takahashi, H., Raymond, J., Reynolds, C. S., & Fabian, A. C. 2010, ApJ, 713, 1244 19, 36, 59, 61

Boirin, L., Méndez, M., Díaz Trigo, M., Parmar, A. N., & Kaastra, J. S. 2005, A&A, 436, 195 16, 94, 101

Bolton, C. T. 1972, Nature, 235, 271 1

Bradt, H. V., Rothschild, R. E., & Swank, J. H. 1993, A&AS, 97, 355 59

Breeveld, A. A., Landsman, W., Holland, S. T., Roming, P., Kuin, N. P. M., & Page, M. J. 2011, GAMMA RAY BURSTS 2010, AIP Conference Proceedings, Volume 1358, pp. 373-376 32

Burrows, D. N., Hill, J. E., Nousek, J. A., et al. 2005, Space Sci. Rev., 120, 165 30

Capitanio, F., Ubertini, P., Bazzano, A., et al. 2005, ApJ, 622, 503 36, 59

Capitanio, F., Belloni, T., Del Santo, M., & Ubertini, P. 2009, ApJ, 398, 1194 36, 46, 50, 58

Cardelli, J. A., Clayton, G. C., & Mathis, J. S. 1989, ApJ, 345, 245 56

Chakravorty, S., Lee, J. C., & Neilsen, J. 2013, MNRAS, 436, 560 22

Chaty, S., Dubus, G., & Raichoor, A. 2011, A&A, 529, 3 18

Chen, Y. P., 2010, Zhang, S., Torres, D. F., Wang, J. M., Li, J., Li, T. P., & Qu, J. L. 2010, A&A, 522, 99 36, 49, 50, 58

Chiang, C. Y., Done, C., Still, M., & Godet, O. 2010, MNRAS, 403, 1102 59, 61

Churazov, E., Gilfanov, M., & Revnivtsev, M. 2001, MNRAS, 321, 759 51

Cooke, B. A., Levine, A. M., Lang, F. L., Primini, F. A., Lewin, W. H. G. 1984, ApJ, 285, 258 36

Corbel, S., Fender, R. P., Tzioumis, A K., Nowak, M., McIntyre, V., Durouchoux, P., & Sood, R. 2000, A&A, 359, 251 18, 19

Corbel, S., Fender, R. P., Tzioumis, A K., Tomsick, J. A., Orosz, J. A., Miller, J. M., Wijnands, R., & Kaaret, P. 2002, Science, 298, 196 17

Corbel, S., & Fender, R. P. 2002, ApJ, 573, 35 18

Corbel, S., Kaaret, P., Fender, R. P., Tzioumis, A. K., Tomsick, J. A., & Orosz, J. A. 2005, ApJ, 632, 504 36

Corbel, S., Coriat, M., Brocksopp, C., Tzioumis, A. K., Fender, R. P., Tomsick, J. A., Buxton, M. M., & Bailyn, C. D. 2013, MNRAS, 428, 2500 18

Corbet, R. H. D., Pearlman, A. B., Buxton, M., & Levine, A. M. 2010, ApJ, 719, 979 101

Coriat, M., Corbel, S., Prat, L., et al. 2011, MNRAS, 414, 677 18, 56

Cui, W., Zhang, S. N., Chen, W., & Morgan, E. H. 1999, ApJ, 512, L43 62

Davis, S. W., Blaes, O. M., Hubeny, I., & Turner, N. J. 2005, ApJ, 621, 372 82

Dhawan, V., Mrabel, L. F., & Rodríguez, L. F. 2000, ApJ, 543, 373 17, 18, 19

Díaz Trigo, M., Parmar, A. N., Boirin, L., Méndez, M., & Kaastra, J. S. 2006, A&A, 445, 179 16, 94, 101

Díaz Trigo, M., Parmar, A. N., Miller, J., Kuulkers, E., & Caballero-García, M. D. 2007, A&A, 462, 657 98, 101

Díaz Trigo, M., Parmar, A. N., Boirin, L., Motch, C., Talavera, A., & Balman, S. 2009, A&A, 493, 145 68, 94

Díaz Trigo, M., & Boirin, L. 2013, Acta Polytechnica, 53, 659 98, 100

Díaz Trigo, M., Miller-Jones, J. C. A., Migliari, S., Broderick, J. W., & Tzioumis, T. 2013, Nature, 504, 260 17

Díaz Trigo, M., Migliari, S., Miller-Jones, J. C. A., & Guainazzi, M. 2014, A&A, 571, 76 19

Done, C., & Kubota, A. 2006, MNRAS, 371, 1216 12

Done, C., Gierliński, M., & Kubota, A. 2007, A&A Rev., 15, 1 6, 8, 13, 14, 57, 62, 81

Done, C., & Diaz Trigo, M. 2010, MNRAS, 407, 2287 12

Done, C. 2010, arXiv:1008.2287 59

Doxsey, R., Bradt, H., Fabbiano, G., et al. 1977, IAU Circ., 3113, 2 36

Draine, B. T. 2003, ApJ, 598, 1026 45

Ebisawa, K., Makino, F., & Mitsuda, K. 1993, ApJ, 403, 684 10

Ebisawa, K., Ogawa, M., Aoki, T., et al. 1994, ApJ, 46, 375 81

Esin, A. A., McClintock, J. E., Drake, J. J., Garcia, M. R., Haswell, C. A., Hynes, R. I., & Muno, M. P. 2001, ApJ, 555, 483 61

Fabian, A. C., Rees, M. J., Stella, L., & White, N. E. 1989, MNRAS, 238, 729 12

Fabian, A. C., Kunieda, H., Inoue, S., et al. 1994, PASJ, 46, L59 73

Fabian, A. C. 2012, ARA&A, 50, 455 23

Falcke, H., Körding, E., & Markoff, S. 2004, A&A, 414, 895 18

Fender, R. P.; Garrington, S. T., McKay, D. J., Muxlow, T. W. B., Pooley, G. G., Spencer, R. E., Stirling, A. M., & Waltman, E. B. 1999, MNRAS, 304, 865 18, 19

Fender, R. P. 2001, MNRAS, 31, 42 18, 19

Fender, R. P., Belloni, T. M., & Gallo, E. 2004, MNRAS, 355, 1105 8, 19, 20

Ferrigno, C., Bozzo, E., Del Santo, M., & Capitanio, F. 2012, A&A, 537, L7 58

Frank, J., King, A. R., & Lasota, J.-P. 1987, A&A, 178, 137 89, 93, 100

Frank, J., King, A., & Raine, D. 1992, Accretion Power in Astrophysics 2rd ed., (Cambridge University Press) 93

Fukazawa, Y., Mizuno, T., Watanabe, S. 2009, PASJ, 61, 17 43

Gandhi, P., Blain, A. W., Russell, D. M., et al. 2011, ApJ, 740, L13 18

Gallo, E., Fender, R. P., Pooley, G. G. 2003, MNRAS, 344, 60 18, 19

Gehrels, N., Chincarini, G., Giommi, P., et al. 2004, ApJ, 611, 1005 30, 31

Gierliński, M., Zdziarski, A. A., & Done, C., Johnson, W. N., Ebisawa, K., Ueda, Y., Haardt, F., & Phlips, B. F. 1997, MNRAS, 288, 958 73, 94

Gierliński, M., Zdziarski, A. A., Poutanen, J., Coppi, P. S., Ebisawa, K., & Johnson, W. N. 1999, MNRAS, 309, 496 12

Gierliński, M., & Done, C. 2003, MNRAS, 342, 1083 12

Gierliński, M., Done, C., & Page, K. 2008, MNRAS, 388, 753 90

Gierliński, M., Done, C., & Page, K. 2009, MNRAS, 392, 1106 90, 91

Gladstone, J., Done, C., & Gierliński, M. 2007, MNRAS, 378, 13 8

Greiner, J., Cuby, J. G., & McCaughrean, M. J. 2001, Nature, 414, 522 98, 101

Greiner, J., Rau, A., & Schady, P. 2012, ATel #4030 66, 87, 88

Han, X., & Hjellming, R. M. 1992, ApJ, 400, 304 19

Hjellming, R. M., & Rupen, M. P. 1995, Nature, 375, 464 17

Homan, J., Wijnands, R., van der Klis, M., Belloni, T., van Paradijs, J., Klein-Wolt, M., Fender, R., & Méndez, M. 2001, ApJS, 132, 377 14

Homan, J., Miller, J. M., Wijnands, R., Steeghs, D., Belloni, T., van der Klis, M., & Lewin, W. H. G. 2003, ATel #162 36

Homan, J., & Belloni, T. 2005, Ap&SS, 300, 107 8

Homan, J., Miller, J. M., Wijnands, R., van der Klis, M., Belloni, T., Steeghs, D., & Lewin, W. H. G. 2005, ApJ, 623, 383 36, 40

Hori, T., Ueda, Y., Shidatsu, M., et al. 2014, ApJ, 790, 20 12, 43, 45, 59

Hynes, R. I., Steeghs, D., Casares, J., Charles, P. A., & O'Brien, K. 2003, ApJ, 583, L95 101

Ingram, A., Done, C., & Fragile, P. C. 2009, MNRAS, 397, L101 62

Ingram, A., & Done, C. 2012, MNRAS, 419, 2369 14

Ishisaki, Y., Maeda, Y., Fujimoto, R., et al. 2007, PASJ, 59, 113 39

Juett, A. M., Psaltis, D., & Chakrabarty, D. 2001, ApJ, 560, L59 95

Kalberla, P. M. W., Burton, W. B., Hartmann, D., Arnal, E. M., Bajaja, E., Morras, R., & Pöppel, W. G. L. 2005, A&A, 440, 775 78

Kaluzienski, L. J., & Holt, S. S. 1977, IAU Circ. 3099 35, 36

Kato, S., Fukue, j., & Mineshige, S. 2008, Black-Hole Accretion Disks, Kyoto University Press 4, 9

Kawabata, K. S., Nagae, O., Chiyonobu, S., et al. 2008, Proc. SPIE, 7014, 4 55

Kawai, N., Matsuoka, M., Pan, H.-C., Stewart, G. C. 1989, PASJ, 41, 491 18

Kennea, J. A., Romano, P., Mangano, V., Beardmore, A. P., Evans, P. A., Curran, P. A., Krimm, H. A. & Yamaoka, K. 2011a, Proceedings of 4th International MAXI Workshop, The First Year of MAXI: Monitoring Variable X-ray Sources, arXiv:1101.6055 33

Kennea, J. A., Romano, P., Mangano, V., et al. 2011b, ApJ, 736, 22 33

Kennea, J. A., Altamirano, D., Evans, P. A., et al. 2012a, ATel #4034 66, 87

Kennea, J. A., Yang, Y. J., Altamirano, D., et al. 2012b, ATel #4044 66, 69

Kokubun, M., Makishima, K., Takahashi, T., et al. 2007, PASJ, 59, 53 25

Kolehmainen, M., Done, C., & Diaz Trigo, M. 2011, MNRAS, 416, 311 10, 81

Kolehmainen, M., Done, C., & Diaz Trigo, M. 2014, MNRAS, 437, 316 12

Kotani T., Kawai, N., Aoki, T., et al. 1994, PASJ, 46, L147 18

Kotani, T., Ebisawa, K., Dotani T., Inoue, H., Nagase, F., Tanaka, Y., & Ueda, Y. 2000, ApJ, 539, 413 14, 15, 61, 97, 101

Koyama, K., Tsunemi, H., Dotani, T., et al. 2007, PASJ, 59, 23 25

Krivonos, R., Revnivtsev, M., Churazov, E., Sazonov, S., Grebenev, S., & Sunyaev, R. 2007, A&A, 463, 957 39

Kubota, A., Tanaka, Y., Makishima, K., Ueda, Y., Dotani, T., Inoue, H., & Yamaoka, K. 1998, PASJ, 50, 667 49, 95

Kubota, A., & Done, C. 2004, MNRAS, 353, 980 12

Kubota, A., & Makishima, K. 2004, ApJ, 601, 428 10, 48

Kubota, A., Dotani, T., Cottam, J., et al. 2007, PASJ, 59, 185 14, 97, 98, 101

Kubota, K., Ueda, Y., Kawai, N., et al. 2010, PASJ, 62, 323 10, 18, 39

Kuulkers, E., Shaw, S. E., Paizis, A., et al. 2007, A&A, 466, 595

Kuulkers, E., Motta, S., & Belloni, T. M. 2012, ATel #4073 66, 69

Laor, A. 1991, ApJ, 376, 90 11, 12, 47, 74

Lee, J. C., Reynolds, C. S., Remillard, R., Schulz, N. S., Blackman, E. G., Fabian, A. C. 2002, ApJ, 567, 1102 22, 61, 101

Maccarone, T. J. 2003, A&A, 409, 697 8, 82, 91

Madej, O. K., Jonker, P. G., Fabian, A. C., Pinto, C., Verbunt, F., & de Plaa, J. 2010, MNRAS, 407, L11 96

Madej, O. K., & Jonker, P. G. 2011, MNRAS, 412, L11 96

Magdziarz, P., & Zdziarski, A. A. 1995, MNRAS, 273, 837 47, 73

Magorrian, J., Tremaine, S., Richstone, D., et al. 1998, AJ, 115, 2285 23

Makishima, K., Takahashi, H., Yamada, S., et al. 2008, PASJ, 60, 585 11, 43, 50, 51, 78, 94

Manmoto, T., Takeuchi, M., Mineshige, S., Matsumoto, R., & Negoro., H. 1996, ApJ, 1996, 464, L135 14

Marshall, F. E., Mushotzky, R. F., Petre, R., & Serlemitsos, P. J. 1993, ApJ, 419, 301 16

Matsuoka, M., Takano, S., Makishima, K. 1986, MNRAS, 222, 605 18

Matsuoka, M., Kawasaki, K., Ueno, S., et al. 2009, PASJ, 61, 999 27, 28, 30

Matt, G., Perola, G. C., & Piro, L. 1991, A&A, 247, 25 47, 74

McClintock, J. E., & Remillard, R. A. 2006, in Compact Stellar X-Ray Sources, ed. W. H. G., Lewin, & M. van der Klis (Cambridge: Cambridge Univ. Press), 157 8, 40, 59

McClintock, J. E., Shafee, R., Narayan, R., Remillard, R. A., Davis, S. W., & Li, L.-X. 2006, ApJ, 652, 518 10

McClintock, J. E., Remillard, R. A., Rupen, M. P., Torres, M. A. P., Steeghs, D., Levine, A. M., & Orosz, J. A. 2009, ApJ, 698, 1398 50, 58

Merloni, A., Heinz, S., & di Matteo, T. 2003, MNRAS, 345, 1057 18

Mihara, T., Matsuoka, M., & Mushotzky, R. F., Kunieda, H., Otani, C., Miyamoto, S., & Yamauchi, M. 1994, PASJ, 46, L137 73

Mihara, T., Nakajima, M., Sugizaki, M., et al. 2011, PASJ, 63, 623 28

Miller, J. M., Raymond, J., Fabian, A. C., et al. 2004, ApJ, 601, 465 101

Miller, J. M., Homan, J., Steeghs, D., Rupen, M., Hunstead, R. W., Wijnands, R., Charles, P. A., & Fabian, A. C. 2006a, ApJ, 653, 525 12, 14, 15, 16

Miller, J. M., Raymond, J., Fabian, A. C., Steeghs, D., Homan, J., Reynolds, C., van der Klis, M., & Wijnands, R. 2006b, Nature, 441, 953

Miller, J. M., Raymond, J., Homan, J., et al. 2006c, ApJ, 646, 394 36, 46, 61, 101

Miller, J. M., Raymond, J., Reynolds, C. S., Fabian, A. C., Kallman, T. R., & Homan, J. 2008, ApJ, 680, 1359 16, 97, 101

Miller, J. M., Maitra, D., Cackett, E. M., Bhattacharyya, S., & Strohmayer, T. E. 2011, ApJ, 731, L7 101

Miller, J. M., Raymond, J., Fabian, A. C., et al. 2012a, ApJ, 759, L6 61

Miller, J. M., Beardmore, A., Kennea, J., King, A. L., Fabian, A. C., Reynolds, C. S., & Raymond, J. 2012b, ATel #4070 66, 68, 81

Miller,J. M., Raymond, J., Kennea., J., et al. 2012c, ATel #4191 66, 81, 87

Miller, J. M., Raymond, J., Kallman, T. R., et al. 2014a, ApJ, 788, 53 98

Miller, J. M., Mineshige, S., Kubota, A., et al. 2014b, arXiv:1412.1173 106

Miller-Jones, J. C. A., Sivakoff, G. R., & Altamirano, D., et al. 2012, MNRAS, 421, 468 19

Mirabel, I. F., & Rodríguez, L. F. 1994, Nature, 371, 46 17

Mirabel, I. F., & Rodríguez, L. F. 1999, ARA&A, 37, 409 17

Mitsuda, K., Inoue, H., Koyama, K., et al. 1984, PASJ, 36, 741 9, 46, 73

Mitsuda, K., Bautz, M., Inoue, H., et al. 2007, PASJ, 59, 1 25, 26, 37, 66

Miyakawa, T., Yamaoka, K., Homan, J., Saito, K., Dotani, T., Yoshida, A., & Inoue, H. 2008, PASJ, 60, 637 59

Miyamoto, S., Kimura, K., Kitamoto, S., Dotani, T., & Ebisawa, K. 1991, ApJ, 383, 784 62

Miyamoto, S., Kitamoto, S., Hayashida, K., Egoshi, W. 1995, ApJ, 442, L13 6

Morihana, K., Nakahira. S., Serino, M., et al. 2013, PASJ, 65, L10 27, 33, 66, 67, 88

Morii, M., Tomida, H., Kimura, M., et al. 2013, ApJ, 779, 118 33

Motta, S., Muñoz-Darias, T., Casella, P., Belloni, T., & Homan, J. 2011, MNRAS, 418, 2292 62

Nagayama, T., et al. 2003, Proc. SPIE, 4841, 459 55, 86

Nakahira, S., Yamaoka, K., Sugizaki, M., et al. 2010, PASJ, 62, L27 27

Nakahira, S., Negoro, H., Shidatsu, M., Ueda, Y., Mihara, T., Sugizaki, M., Matsuoka, M., & Onodera, T. 2014, PASJ, 66, 84 27

Nandra, K., & Pounds, K. A. 1992, Nature, 359, 215 73

Negoro, H., Kitamoto, S., & Mineshige, S. 2001, ApJ, 554, 528 14

Negoro, H., Yamaoka K., Nakahira, S., et al. 2010a, ATel #2873 27

Negoro, H., Nakahira S., Ueda, Y., et al. 2011, ATel #3330 27

Negoro, H., Ozawa, H., Suwa, F., Asada, M., Serino, M., & the MAXI Team 2012, ASP Conf. Ser., 461, 797 66

Neilsen, J., & Lee, J. C. 2009, Nature, 458, 481 22, 61

Neilsen, J., Remillard, R. A., & Lee, J. C. 2011, ApJ, 737, 69 15

Ninkov, Z., Walker, G. A. H., & Yang, S. 1987, ApJ, 321, 425 2

Nowak, M. A. 1995, PASP, 107, 1207 6

Nowak, M. A. 2000, MNRAS, 318, 361 13

Oda, M., Gorenstein, P., Gursky, H. 1971, ApJ, 166,L1 1

Oppenheimer, J. R., & Snyder, H. 1939, Physical Review, 56, 455 1

Orosz, J. A., & Bailyn, C. D. 1997, ApJ, 477, 876 89

Orosz, J. A., McClintock, J. E., Aufdenberg, J. P., Remillard, R. A., Reid, M. J., Narayan, R., & Gou, L. 2011, ApJ, 742, 84 2

Paragi, Z., van der Horst, A. J., Belloni, T., et al. 2013, MNRAS, 432, 1319 19

Parmar, A. N., Kuulkers, E., Oosterbroek, T., et al. 2003, A&A, 411, L421 36

Papitto, A., D'Aì, A., Motta, S., Riggio, A., Burderi, L., di Salvo, T., Belloni, T., & Iaria, R. 2011, A&A, 526, L3 101

Paczyński, B. 1971, ARA&A, 9, 183 89

G. Ponti, G., Fender, R. P., Begelman, M. C., Dunn, R. J. H., Neilsen, J., & Coriat, M. 2012, MNRAS, 422, L11 14, 19, 21, 61

Pounds, K. A., Nandra, K., Fink, H. H., & Makino, F. 1994, MNRAS, 267, 193 73

Prat, L., Rodriguez, J., Cadolle Bel, M., et al. 2009, A&A, 494, L21 36

Predehl, P., & Schmitt, J. H. M. M. 1995, A&A, 293, 889 56, 88

Rahoui, F., Chaty, S., Rodriguez, J., Fuchs, Y., Mirabel, I. F., & Pooley, G. G. 2010, MNRAS, 715, 1191 91

Rahoui, F., Coriat, M., & Corbel, S., et al. 2012, MNRAS, 422, 2202 91

Reis, R. C., Miller, J. M., & Fabian, A. C. 2009, MNRAS, 395, L52 61

Reis, R. C., Fabian, A. C., & Miller, J. M. 2010, MNRAS, 402, 836 12

Remillard, R. A., Morgan, E. H., McClintock, J. E., Bailyn, C. D., & Orosz, J. A. 1999, ApJ, 522, 397 89

Remillard, R. A., & McClintock, J. E. 2006, ARA&A, 44, 49 3

Rieke, G. H., & Lebofsky, M. J. 1985, ApJ, 288, 618 88

Romano, P., Campana, S., Chincarini, G., et al. 2006, A&A, 456, 917 68

Roming, P. W. A., Kennedy, T. E., Mason, K. O., et al. 2005, Space Sci. Rev., 120, 95 30

Rupen, M. P., Mioduszewski, A. J., & Dhawan, V. 2003, ATel #142 36

Rushton, A., Miller-Jones, J. C. A., Campana, R., et al. 2012, MNRAS, 419, 3194 19

Russel, D. M., Markoff, S., Casella, P., et al. 2013, MNRAS, 429, 815 18

Rybicki, G. B., & Lightman, A. P. 1979, Radiative Processes in Astrophysics (New York: Wiley-Interscience), ch. 7 10

Sato, R., Serino, R., Nakahira, S., et al. 2012, ATel #4024 65, 66

Schulz, N. S., Kallman, T. E., Galloway, D. K., Brandt, W. N. 2008, ApJ, 672, 1091 97, 101

Schwarzschild, K. 1916, SB Preuss. Akad. Wiss., Berlin, pp. 424 1

Serlemitsos, P. J., Soong, Y., Chan, K., et al. 2007, PASJ, 59, 9 26

Shafee, R., McClintock, J. E., Narayan, R., Davis, S. W., Li, L.-X., & Remillard, R. A. 2006, ApJ, 636, L113 10

Shaposhnikov, N., & Titarchuk, L. 2007, ApJ, 663, 445 14

Shakura, N. I., & Sunyaev, R. A. 1973, A&A, 24, 337 8, 83

Shidatsu, M., Ueda, Y., Nakahira, S., et al. 2011a, PASJ, 63, 803 10, 27

Shidatsu, M., Ueda, Y., Tazaki, F., et al. 2011b, PASJ, 63, 785 11, 12, 18, 50, 78, 94

Shidatsu, M., Negoro, H., Nakahira, S., et al. 2012, ATel #4419 35, 37

Shidatsu, M., Ueda. Y., Nakahira, S., et al. 2013, ApJ, 779, 26 24, 58

Shidatsu, M., Ueda. Y., Yamada, S., et al. 2014, ApJ, 789, 100 24

Shimura, T., & Takahara, F. 1995, ApJ, 445, 780 59

Skrutskie, M. F., Cutri, R. M., Stiening, R., et al. 2006, AJ, 131, 1163 56, 87

Smale, A. P., Mukai, K., Williams, O. R., Jones, M. H., Corbet, R. H. D. 1992, ApJ, 400, 330 93

Smith, R. K., Edgar, R. J., & Shafer, R. A. 2002, ApJ, 581, 562 45

Sobczak, G. J., McClintock, J. E., Remillard, R. A., Levine, A. M., Morgan, E. H., Bailyn, C. D., & Orosz, J. A. 1999, ApJ, 517, L121 62

Sobczak, G. J., McClintock, J. E., Remillard, R. A., Cui, W., Levine, A. M., Morgan, E. H., Orosz, J. A., & Bailyn, C. D. 2000, ApJ, 531, 537 14

Steeghs D., Miller J. M., Kaplan D., & Rupen, M. 2003, ATel #146 36

Steiner, J. F., Narayan, R., McClintock, J. E., & Ebisawa, K. 2009, PASP, 121, 1279 81

Steiner, J. F., McClintock, J. E., Remillard, R. A., Gou, L., Yamada, S., & Narayan, R. 2010, ApJ, 718, L117 10

Steiner, J. F., McClintock, J. E., & Reid, M. J. 2012, ApJ, 745, L7 35, 36

Sturner, S. J., & Shrader, C. R. 2005, ApJ, 625, 923 58

Takahashi, T., Abe, K., Endo, M., et al. 2007, PASJ, 59, 35 25, 39, 68

Takahashi, H., Fukazawa, Y., Mizuno, T., et al. 2008, PASJ, 60, 69 11, 19, 50, 78, 94

Takahashi, T., Mitsuda, K., Kelley, R., et al. 2012, Proc. SPIE, 8443, 12 100, 104

Tananbaum, H., Gursky, H., Kellogg, E., Giacconi, R., & Jones, C. 1972, ApJ, 177, L5 19

Tamura., M., Kubota, A., Yamada, S., Done, C., Kolehmainen, M., Ueda, Y., & Torii, S. 2012, ApJ, 753, 65 12, 59, 62

Tanaka, Y., & Shibazaki, N. 1996, ARA&A, 34, 607 4, 5, 73

Titarchuk, L., & Fiorito, R. 2004, ApJ, 612, 988 14, 62

Titarchuk, L., & Shaposhnikov, N. 2005, ApJ, 626, 298 62

Tody, D. 1986, Proc. SPIE, 627, 733 56

Tomida, H., Tsunemi, H., Kimura, M., et al. 2011, PASJ, 63, 397 28

Tomsick, J., A., & Kalemci, E. 2003, ATel #198 36

Tomsick, J. A., Yamaoka, K., Corbel, S., Kaaret, P., Kalemci, E., & Migliari, S. 2009, ApJ, 707, L87 12

Ueda, Y., Ebisawa, K., & Done, C. 1994, PASJ, 46, 107 12

Ueda, Y., Inoue, H., Tanaka, Y., Ebisawa, K., Nagase, F., Kotani, T., & Gehrels, N. 1998, ApJ, 492, 782 14, 61, 101

Ueda, Y., Murakami, H., Yamaoka, K., Dotani, T., & Ebisawa, K. 2004, ApJ, 609, 325 14, 97, 101

Ueda, Y., Yamaoka, K., & Remillard, R. 2009, ApJ, 695, 888 101

Ueda, Y., Honda, K., Takahashi, H., et al. 2010, ApJ, 713, 257 19, 43, 45

van der Klis, M. 2004, arXiv:astro-ph/0410551 14

Vignarca, F., Migliari, S., Belloni, T., Psaltis, D., & van der Klis, M. 2003, A&A, 397, 729 62

Wainscoat, R. J., Cohen, M., Volk, K., Walker, H. J., & Schwartz, D. E. 1992, ApJS, 83, 111 56, 88

Watson, M. G., Stewart, G. C., Brinkmann, W., King, A. R. 1986, MNRAS, 222, 261 18

Webster, B. L., & Murdin, P. 1972, Nature, 235, 37 1

White, N. E., & Swank, J. H. 1982, ApJ, 253, L61 16

Woods, D. T., Klein, R. I., Castor, J. I., McKee, C. F., & Bell, J. B. 1996, ApJ, 461, 767 16, 97

Xiang, J., Lee, J. C., Nowak, M. A., Wilms, J., & Schulz, N. S. 2009, ApJ, 701, 984 101

Yamada, S., Uchiyama, H., Dotani, T., et al. 2012, PASJ, 64, 53 43

Yamada, S., Makishima, K., Torii, S., Torii, S., Noda, H., & Sakurai, S. 2013a, PASJ, 65, 80 11, 50, 51, 52, 58, 60, 61, 78, 94

Yamada, S., Negoro, H., Torii, S., et al. 2013b, ApJ, 767, 34 14

Yamaoka, K., Ueda, Y., Inoue, H., Nagase, F., Ebisawa, K., Kotani, T., Tanaka, Y., & Zhang, S. N. 2001, PASJ, 53, 179 98

Zdziarski, A. A., Johnson, W. N., & Magdziarz, P. 1996, MNRAS, 283, 193 46, 73

Zhou, J. N., Liu, Q. Z., Chen, Y. P., Li, J., Qu, J. L., Zhang, S., Gao, H. Q., & Zhang, Z. 2013, MNRAS, 431, 2285 58

Życki, P. T., Done, C., & Smith, D. A. 1999, MNRAS, 309, 561 46, 73

Acknowledgements

It is my great pleasure to express my most sincere gratitude and appreciation to my supervisor, Dr.Yoshihiro Ueda, for his guidance, support, advice, encouragement, and any other things he has provided for over six years. He often told that we observationalists must be fully responsible for the accuracy and reliability of the results and that we should check the data carefully and repeatedly not to leave any errors or unreliability. In my work, including this thesis, I have tried to follow this fundamental principle of scientific research. I am also grateful to Professor Chris Done in Durham University (whom I have regarded as another supervisor) for fruitful discussions with sharing her rich knowledge and insights on black hole astrophysics, as well as for what she did for me during my stays in Durham (including the amazing trip to Hadrian's Wall). I would like to thank Professor Shin Mineshige, my sub-supervisor, for instructive comments both in the theoretical and observational points of view.

I was supported by many experts of black hole X-ray binaries. In particular, Dr. Aya Kubota, Dr. Sin'ya Yamada, and Dr. Kazutaka Yamaoka gave me many helpful suggestions on the X-ray analysis and made valuable discussions of the results. I appreciate all the members of the *MAXI* mission, in which I have participated for five years. They provided unique opportunities to witness and to get involved with many exciting discoveries, including new galactic transients, tidal disruption events around supermassive black holes, gamma-ray bursts, large flares from stars. My special thanks go to Dr. Satoshi Nakahira for his great help concerning the *MAXI* data analysis and software development, and also to Professor Hitoshi Negoro and Professor Nobuyuki Kawai for helpful comments on the *Suzaku* results of MAXI J1305−704. I would like to continue working for the *MAXI* mission, and I hope that *MAXI* keeps making great contributions to the progress of X-ray astronomy. I am also grateful to Dr. Takahiro Nagayama for carrying out near-infrared observations, and to Dr. Yuki Moritani and the members of the *Kanata* team in Hiroshima University for optical observations. I hope to continue collaborating with all these people.

I would like to thank all the members, both current and past, of Dr. Ueda's group ("Uedaken"): Dr. Fumie Tazaki, Dr. Kazuo Hiroi, Dr. Naoki Isobe, Dr. Masaaki Hayashida, Dr. Satoshi Eguchi, Dr. Claudio Ricci, Dr. Kenta Matsuoka, Mr. Kohei Ichikawa, Mr. Ryosuke Sato, Mr. Taiki Kawamuro, Mr. Takafumi Hori, and Mr. Shota Mizuno for always kindly helping me and filling my postgraduate life with lots of fun. It was my great pleasure to study with them.

Last, but not least, I am very grateful to all the members of my family. I could not have finished this thesis without their continuous encouragement and support. I dedicate this thesis to my late father, who was looking forward to the day I complete my Ph.D. degree. He taught me the value of hard work. Fighting against his terminal cancer, he kept working very hard as a professional civil engineering consultant to propose the best plans for construction and maintenance of various structures in difficult site conditions. I will never forget his enthusiasm, devotion, and professionalism, which he had showed to me until the very last moment of his life.

This research has made use of the *MAXI* data provided by RIKEN, JAXA and the *MAXI* team. I appreciate the *Suzaku* operation team for arranging and carrying out the TOO observations. This work utilized the *Swift* public data archive, as well as data products from the Two Micron All Sky Survey, which is a joint project of the University of Massachusetts and the Infrared Processing and Analysis Center/California Institute of Technology, funded by the National Aeronautics and Space Administration and the National Science Foundation. I acknowledge financial support from a Grant-in-Aid for JSPS Fellows for Young Researchers.